REDUCED-ORDER MODEL FOR PREDICTION OF STAGED-COMBUSTOR NO_X EMISSIONS WITH DETAILED CHEMISTRY AND FINITE-RATE MIXING

A Dissertation
Presented to
The Academic Faculty

By

Edwin Y. Goh

In Partial Fulfillment
of the Requirements for the Degree of
Doctor of Philosophy in the
School of Aerospace Engineering

Georgia Institute of Technology

May 2020

REDUCED-ORDER MODEL FOR PREDICTION OF STAGED-COMBUSTOR NO_X EMISSIONS WITH DETAILED CHEMISTRY AND FINITE-RATE MIXING

Approved by:

Dr. Jerry Seitzman, Advisor
School of Aerospace Engineering
Georgia Institute of Technology

Dr. Timothy Lieuwen
School of Aerospace Engineering
Georgia Institute of Technology

Dr. Brian German
School of Aerospace Engineering
Georgia Institute of Technology

Dr. Tobin Isaac
School of Computational Science and Engineering
Georgia Institute of Technology

Dr. Joseph Oefelein
School of Aerospace Engineering
Georgia Institute of Technology

Date Approved: April 23, 2020

I will make your descendants as numerous as the stars in the sky and will give them all these lands, and through your offspring all nations on earth will be blessed.

Genesis 26:4

To Shan

ACKNOWLEDGEMENTS

This is arguably the hardest section of a thesis to write, partly due to my realization that it is by far the most widely perused section of most theses, and partly because there are literally too many people to acknowledge — from the countless baristas who kept me awake when I couldn't bring myself to make my own coffee to the custodians who tirelessly recycled my similarly innumerable coffee cups, not to mention the artists, musicians, novelists and authors whose creativity I can only dream of appreciating let alone acquiring, who satisfied my very human need to escape into an idyll world tucked away from the very real one in which we live. Then there are the people who helped me along the way, to whom the gratitude I owe simply cannot be put into nor repaid with words. Nonetheless, I shall try my best to pen these thoughts and feelings into bytes on your screen.

First of all, if there were only space for one person in this section, I would choose to recognize my advisor in a heartbeat. After journeying halfway around the globe in my quest to help democratize access to space and wandering through a few other undergraduate research projects, I finally stumbled into the combustion lab in my third year to work with Prof. Jerry Seitzman — and he is the reason I stuck around for 5 more years. Throughout my relatively short sojourn on Earth, I have met no other person who is as caring towards his students and as passionate about *educating* his students. For each time I struggled in life and berated myself for not being a better student, researcher, friend, son, or what have you—and believe me there have been far too many times, especially being separated from family—he would offer two times the encouragement. There is no doubt in my mind that you would not be reading this thesis if it weren't for Prof. Seitzman and the precious support that he offered. So thank you, Professor, for your guidance, your patience, and your sacrifice. I would not have been able embark on my journey toward the cosmos without you lighting the way, and I have been truly blessed to work with (by no less than ten thousand light years) the best advisor, mentor and teacher that any student could hope to have.

I would like to thank Prof. Tim Lieuwen for putting this project together and nurturing it to fruition. His intellectual curiosity and energy pushed me to grow both as a researcher and as a person. He has been and will always be my reminder to glorify God through my work and actions, and to be the hardest worker in the room. I would also like to offer a big “thank you” to my committee members Profs. Brian German, Tobin Isaac and Joseph Oefelein, who introduced me to multidisciplinary design optimization, high performance computing, and computational fluid dynamics, respectively. Their world-class guidance throughout this research, from the challenging questions during the thesis proposal to the insightful comments during the defense, have made this thesis clearer and more well-rounded. I strive to one day achieve the level of passion and mastery they possess in their respective disciplines.

Newton said, "If I have seen further it is by standing on the shoulders of Giants." I have been blessed to be surrounded by such Giants in the combustion lab. I am thankful to the ones who came before me in Prof. Seitzman’s group and helped nurture me from a young experimentalist into a serious developer. Dr. Brandon Sforzo was my first research mentor whose guidance piqued my interest in computational modeling. Dr. Sheng Wei will forever be my sifu in Cantera, and I am forever grateful for his patience with my horrible coding practices when I first started out as an undergraduate student. Dao Hoang, with whom I had the chance of reuniting at JPL, was at the time my sole conspirator in testing the FAA forced ignition rig, and was instrumental in teaching me the excitement of building a rig and eventually harvesting data from it. Dr. Nishant Jain was the one who called and texted me with advice, support and congratulations before and after quals, my proposal, *and* my defense. Our road trip to Turbo Expo in 2018 with Sheng is a fond memory that I will forever look back upon with a smile. Although he may, through no fault of his own, be unaware of it, Dr. Sampath Adusumilli was one of my greatest sources of intellectual and emotional support in the lab. He never failed to go the extra mile in helping me figure out a tough problem, be it in research or in coursework.

A huge thank you to my team mates on the DOE Low-NO_x team — Vedanth Nair, Dr. Matthew Sirignano, and Dr. Ben Emerson — for the great meetings and stimulating discussions about how we can achieve a functional high-temperature, low-NO_x combustor design. Thank you all for bearing with me despite speaking seemingly different languages of hardware vs. software, science vs. engineering, and for welcoming me onto the team. I owe Vedanth special gratitude for his assistance during my preparation for the qualifying exams. In addition, the combustion lab was a tremendous place to work thanks to the support and companionship provided by my fellow graduate students — Hanna Ek, Jeong-Won Kim, Kotaro Koike, Subodh Adhikari, Raghul Manosh and Henderson Johnson, to name a few. I also appreciate the recent additions to our little corner of the lab — Dr. Samuel Grauer, Asker Kazbekov and Leslie Hsiao — who brought with them fresh ideas, perspectives and insights. For instance, Sam will forever be the person who made me aware of the fact that one can copy a MATLAB figure, paste it into PowerPoint, and customize it as an object. Neat!

I have been blessed with the opportunity to work with, teach, and learn from three outstanding colleagues — James Li, Patrick Lei and Nam Young Kim — on the DOE Low-NO_x project. Their diligence and sheer intelligence have contributed a great deal to this thesis in ways that I could not have imagined had I been the sole contributor. I apologize for the times when we appeared stuck in a local minima without directions on where to take the project, and am forever grateful for the incredible patience they demonstrated in continuing to journey with Prof. Seitzman and me.

Having been at Georgia Tech for almost eight years, I came to experience deep, meaningful friendships that made me feel more at home in Atlanta than I ever felt back in my home country. Chun Qi Lim, Michelle Soo and Shea Chee Tan provided me with weekends to look forward to, and with enough laughter to last a lifetime. Jing Dao Chen introduced me to the world of machine learning and artificial intelligence, without whose influence I would not have pursued the intersection between engineering and AI, and for

that I am deeply grateful. I am thankful for the companionship that Anant Girdhar provided throughout my graduate career, especially during the time we were colleagues on the DOE Low-NO_x project. Painful though they may have been, our late-night struggles while taking Prof. Seitzman's combustion course will always be one of my best memories from Georgia Tech. Special thanks goes to Andy Kim, with whom I started my graduate career. Thank you, Andy, for the hours of great discussions, jam sessions, and the immense spiritual and emotional support you provided me as we prepared for the qualifying exams together.

As I continued to learn more about nature and science at Georgia Tech, so also have I questioned, explored and learned about the nature of my existence. I have come to know my part in God's story thanks to spiritual brothers and sisters including Gem Valencia, Patrick Lei, Andy Kim, Lee Thompson, Tracey West, Neale Hightower, Carol Hightower, Prof. Lakshmi Sankar, Jason Chen and Jasmine Shi. Our conversations and fellowship together have truly been a foretaste of heaven. I am also very grateful to my brothers and sisters at the Westminster Christian Fellowship, many of whom have become my second family in Atlanta. Their light helped keep me strong even in my darkest hours and their constant prayers are the reason I could encounter such a wonderful advisor, receive research assistantship *on the very day school started*, pass quals on my first attempt, and eventually complete this thesis with my sanity intact. They have taught me the power of faith and prayer, and the power of letting God be God.

After my family in Atlanta comes my real family to whom I literally owe my very existence. Pa and Mi, we don't normally say it at home, but thank you all for not abandoning me as a child for all the times I caused you grief. I know I would have! Thank you for teaching me what it means to love sacrificially and for providing me with the opportunity to pursue my dreams. Thank you for the unconditional love and support that you demonstrated through your actions, which speak louder (sometimes deafeningly so) than words. Thank you for pulling me through the toughest of times, even though it must have been twice as tough for you to not be here with me. I also owe my one and only sister

Rachel much gratitude for her companionship and emotional support as I fought to finish my thesis, and for forwarding funny posts that brighten my otherwise monotonous days.

I would be remiss (read: in grave danger) if I did not include my North Star. Shan, thank you for accepting me for who I am, and for continuing to love me even when I sometimes couldn't love myself. Thank you for encouraging me to work harder and to get out of my comfort zone for the sake of our future family. Thank you for praying for me constantly and for being the resting place in my heart to which I can return. Thank you for motivating me to want to want to (that's a second-order derivative) become a better human being, and most importantly for painstakingly drawing Figure 5.4!

Last but not least, I owe it all to Him who taught me that "the last will be first, and the first will be last." Thanks be to God who blessed me through joys and sufferings in ways only He can, not because I am deserving but because of His grace. May this thesis, the work behind it and the work that comes after it bring glory to His name.

TABLE OF CONTENTS

Acknowledgments v

List of Tables xiv

List of Figures xv

List of Symbols and Abbreviations xxi

Chapter 1: Introduction 1

1.1 Motivation 1

1.2 Literature Review 2

1.2.1 Oxides of Nitrogen: A Brief Introduction 2

1.2.2 NO_x Reduction Techniques 6

1.2.3 Staged Combustion: A Promising Architecture for Low-NO_x Combustors 9

1.2.4 Mixing and Entrainment 10

1.2.5 Jets In Cross Flow (JICF) 12

1.3 Research Questions 13

1.4 Thesis Organization 17

Chapter 2: Approach 19

2.1 Elements of Chemical Reactor Network (CRN) Modeling 19

2.2 Staged Combustor Reactor Network Model 23

2.2.1 Main Burner Stage 23

2.2.2 Secondary Stage 25

2.2.3 Chemical Mechanism 25

2.3 Design Optimization 26

Chapter 3: Theoretical Minimum Staged Combustor NO_x Levels 27

3.1 Ideal Secondary Stage Model 27

3.2 NO_x Reduction Potential of Staged Combustion 30

3.3 Parametric Studies 31

3.3.1 Fuel Split Sweep 32

3.3.2 Secondary Stage Residence Time Sweep 33

3.4 Minimum NO 35

3.4.1 Optimization Algorithm 35

3.4.2 Fundamental NO_x Limits 36

3.5 Global Residence Time Sensitivity 38

3.6 Sensitivity to Kinetic Mechanisms 40

3.7 Multi-Point Design with CO Constraint at Part Load (1650 K) 42

3.8 Summary of Minimum NO Results 46

3.9 Finite-Rate Mixing Effects 47

3.9.1 Secondary Stage: Worst-Case Model 48

3.9.2 Worst-Case NO_x Emissions 49

Chapter 4: Finite-Rate Entrainment Effects 51

4.1 Approach 51

4.1.1 Generic Flow Field 51

4.1.2 Physical Parameters 52

4.1.3 Secondary Stage Model 53

4.1.4 Model Parameters 56

4.1.5 Design Optimization 58

4.2 Finite Entrainment Effects: Pure Fuel Secondary Stage 61

4.3 Finite Entrainment Effects: Fuel-Air Secondary Stage 68

4.3.1 Varying ϕ_{sec} Under Constant r_τ 68

4.3.2 Varying ϕ_{sec} Under Constant Entrainment Rates 75

4.3.3 Connection with Experimental Findings 77

4.4 Minimum NO Configuration 81

4.5 Chapter Summary 83

Chapter 5: Finite-Rate Mixing Effects 86

5.1 Limitations in Current Finite-Rate Mixing Models 86

5.1.1 PaSR Background 86

5.1.2 CHEMKIN PaSR Validation and Limitations 87

5.2 Limited Mixing and Entrainment (LiME) Reactor 92

5.2.1 Conceptual Description 92

5.2.2 Model Implementation 95

5.2.3 Model Validation 99

5.3 Finite-Rate Mixing Effects with Infinitely Fast Entrainment 100

5.4 Finite Mixing and Entrainment Effects on NO_x 105

5.5 Chapter Summary 108

Chapter 6: Conclusion 110

6.1 Thesis Contributions 110

6.1.1 Fundamental Minimum NO_x Limits 110

6.1.2 Characterization of Finite-Rate Entrainment Effects 111

6.1.3 Limited Mixing and Entrainment (LiME) Reactor Model 113

6.2 Recommendations for Future Work 115

6.2.1 Further Design Space Exploration 115

6.2.2 LiME Reactor Performance Characterization and Optimization . . . 116

6.2.3 Reinforcement Learning Design Optimization Framework 117

Appendix A: Supplementary Figures 120

A.1 Chapter 4 120

Appendix B: Source Code 122

References 131

LIST OF TABLES

3.1 Constant parameters used to simulate gas turbine operating conditions. . . . 30

4.1 List of parameters required by the finite-entrainment staged combustor model. 59

4.2 Parameters held constant in this study. 60

4.3 Design parameters and the associated bounds used by the optimization algorithm to find minimum NO levels. 81

4.4 Optimum solution determined from the finite-rate entrainment model. . . . 82

5.1 Constraints and desirable properties of micromixing models taken from [92]. Note that not all constraints and properties are essential for the present use case where the system does not have an exit. 94

LIST OF FIGURES

1.1 Plot that illustrates the positive relationship between turbine inlet temperature and thermal efficiency. The temperature corresponding to 65% efficiency is 1700 °C (roughly 1975 K). Figure reproduced from [11]. 3

1.2 Variation in predicted minimum NO emissions from a lean premixed and EGR-type combustor with adiabatic flame temperature at 25 atm for a residence time of 25 ms, following [31]. 8

1.3 Examples of axial staged combustors by GE and Pratt & Whitney 10

1.5 Examples of naturally occurring and man-made JICF phenomena. 13

1.6 Time-averaged flow field of a typical (incompressible) JICF taken from Mahesh [52]. Contours of vertical velocity are shown, with blue indicating regions of high vertical velocity and red indicating regions of low velocity. . 14

2.1 Example CRN composed of Perfectly-Stirred Reactors (PSRs) and Plug-Flow Reactors (PFRs) developed using a prescribed combustor flow field. (Taken from Mavris [57]) 20

3.1 Simplified diagram of an axial fuel-staged combustor and the chemical reactors used to model it. 28

3.2 Block diagram of ideal staged combustor CRN model showing various combustor design parameters used in the optimization problem. 29

3.3 Temperature and NO time traces calculated using axial fuel-staged combustor model at 1975 K exit temperature. Solid lines represent cases where τ_{sec} = 5 ms while dotted lines represent cases where τ_{sec} = 2 ms. 31

3.4 Variation of NO and CO emissions with ϕ_{main} for $T_{exit} = 1975K$ and $\tau_{sec} = 0.5$ ms 33

3.5 Variation of NO and CO emissions with τ_{sec} for $T_{exit} = 1975K$ and $\phi_{main} = 0.42$. 34

3.6 Variation of NO emissions versus CO emissions at various τ_{sec} values for $T_{exit} = 1975K$ and $\phi_{main} = 0.43$. 35

3.7 Predicted minimum NO and corresponding CO levels at different firing temperatures for the AFS architecture (blue solid line), subject to 125% CO constraint, alongside predictions for a conventional LPM combustor (dashed line). 37

3.8 Configurations corresponding to minimum NO results for axial fuel-staged architecture. 38

3.9 Minimum NO achievable and corresponding main burner equivalence ratio for the 1975 K AFS combustor at multiple residence times. 39

3.10 Fundamental NO limits for the staged combustor architecture at various firing temperatures calculated using three different reaction mechanisms. A conventional LPM combustor fundamental limit is shown for comparison. 40

3.11 Predicted NO values for lean premixed 1-D laminar flames at various equivalence ratios using different reaction mechanisms. 42

3.12 Predicted NO in the secondary stage demonstrating differences in overall NO due to variations across mechanisms of the amount of prompt NO produced at early times. 43

3.13 Variation in NO and CO emissions across various firing temperatures for an ideal 20 ms staged combustor optimized for the 1975 K operating condition (ϕ_{main} = 0.37, τ_{sec} = 0.28 ms). 44

3.14 Variation in NO and CO emissions across various firing temperatures for a 20 ms AFS combustor optimized to minimize NO at full load and maintain 32 ppm CO at part load (ϕ_{main} = 0.449, τ_{sec} = 0.16 ms). The dashed lines show the variation in NO and CO across the same range of temperatures for a staged combustor optimized for minimum NO at 1760 K. 45

3.15 Block diagram depicting reactor network model used to study worst-case finite mixing rate effects on minimum NO_x. 48

3.16 Temperature evolution of the worst-case staged combustor model with a secondary residence time of 5 ms demonstrates the high temperature at which all the fuel injected in the secondary stage burns, thereby causing excessive NO_x emissions. 49

3.17 Time traces of local NO concentration for an LPM combustor (labeled "Baseline"), an ideal (at 1975 K) AFS combustor, and a worst-case stage combustor show that the worst-case staged combustor produces roughly 10x more NO than an ideal staged combustor. 50

4.1 Fuel jet emitting into coflowing vitiated products and the associated entrainment of both streams. Three regions are identified in the flow field — pure jet fluid, pure vitiated products, and an entrained region. 52

4.2 Reactor network used to model the secondary stage of a staged combustor under finite-entrainment of main and secondary streams. In this work, the entrained region is assumed to be a region where diffusive mixing is instantaneous. The model for the main burner is the same as the one described in Section 2.2.1 and used in Chapter 3. 56

4.3 Variation in main and secondary inlet mass flow rates with secondary equivalence ratio as governed by Equation 4.5. Results shown for $M_{total} = 100$, $\phi_{main} = 0.37$, $\phi_{global} = 0.64$, $f_s = 0.058$ (CH_4-air). 58

4.4 Corrected NO at 125% CO_{eq} constraint across different main burner entrainment time scales $\tau_{ent,main}$ and entrainment ratios $r_\tau \equiv \tau_{ent,main}/\tau_{ent,sec}$. 61

4.5 Variation of corrected NO (at 125% CO_{eq} constraint) with entrainment ratio r_τ varying from 0.6 to 8.0 across main burner entrainment time scales $\tau_{ent,main}$ = 1.0 ms, 2.0 ms and 5.0 ms. 63

4.6 Time evolution of entrained region temperature and system averaged NO for $\tau_{ent,main} = 5$ ms and $r_\tau = 0.6$, 1.0 and 1.2. System averaged NO accounts for unentrained reactants when calculating the corrected value. For r_τ = 0.6 and 1.0, the time evolution of the system is shown until system average CO reaches the 125% CO_{eq} constraint. 64

4.7 Time evolution of entrained region temperature and system averaged NO for $\tau_{ent,main} = 5$ ms and $r_\tau = 2.0$, 2.3, and 6.0. System averaged NO accounts for unentrained reactants when calculating the corrected value. The time evolution of the system is shown until system average CO reaches the 125% CO_{eq} constraint. 66

4.8 Distribution of secondary equivalence ratio used in the present study. 69

4.9 Corrected NO at 125% CO_{eq} constraint across entrainment ratio r_τ for various ϕ_{sec} and $\tau_{ent,main}$ combinations. 70

4.10 Corrected NO at 125% CO_{eq} constraint across different secondary equivalence ratios ϕ_{sec} for different main burner entrainment time scales $\tau_{ent,main}$ and entrainment ratios r_τ. 71

4.11 Maximum local temperature achieved in the entrained region across different secondary equivalence ratios ϕ_{sec} for different main burner entrainment time scales $\tau_{ent,main}$ and entrainment ratios r_τ. 72

4.12 Time traces of entrained region temperature, entrained region equivalence ratio and corrected system NO for various ϕ_{sec} at $\tau_{ent,main}$ = 5 ms and r_τ = 2.2 and 7.8. 73

4.13 Time traces of entrained region temperature, entrained region equivalence ratio and corrected system NO for various ϕ_{sec} at $\tau_{ent,main}$ = 5 ms and r_τ = 0.33. The horizontal time axis is plotted on a logarithmic scale to magnify pre-ignition features in the temperature and equivalence ratio plots. The ignition equivalence ratio of the entrained region, ϕ_{ign}, is indicated with round markers on top of the equivalence ratio subplot. 75

4.14 Variation of NO with $\phi_{sec,norm}$ for three constant values of entrainment rate ratios. The variation of r_τ with $\phi_{sec,norm}$ for the three entrainment rate ratios (as governed by Equation 4.8) are shown in blue. 76

4.15 Experimental results of normalized NO_x levels and liftoff height as a function of normalized jet equivalence ratio, as well as normalized NO_x levels as a function of liftoff height. Red markers indicate results obtained at $\phi_{main} = 0.50$ and blue markers indicate results obtained at $\phi_{main} = 0.45$. Crossflow conditions were held constant and $J \leq 20$ for all cases [80]. . . . 78

4.16 Variation in NO over ϕ_{main} and M_{sec}/M_{total} for $\phi_{global} = 0.635$, $\tau_{ent,main} =$ 5 ms and $\tau_{ent,sec} = 1$ ms. 83

5.1 Comparison between ensemble average temperatures (i.e., average temperatures across all particles in the reactor) for Correa's PaSR (top) and CHEMKIN's implementation. 89

5.2 Comparison between ensemble average mass fraction of NO for Correa's PaSR (top) and CHEMKIN's implementation (bottom). 90

5.3 NO and CO prediction time histories from the CHEMKIN PaSR model of an axial fuel-staged combustor for $\phi_{global} = 0.64$, $\phi_{main} = 0.37$ and $\tau_{mix} = 0.05ms$ for different NPAR-NREP combinations. Note that both variables are equally scaled by multiples of 3, 5 and 9 from the base case of NPAR = 1000 and NREP = 6. 91

5.4 Illustration of the time evolution of a batch of reactants within LiME (Limited Mixing and Entrainment) Reactor 92

5.5 Illustration of a LiME reactor with three non-reacting particles used to validate the IEM mixing model. 100

5.6 Enthalpy and mass time traces for the non-reacting three-particle LiME reactor illustrating that the mixing step conserves mass of each species although they are being transported across different particles. Total system enthalpy is also conserved to within 1 J, which is thought to be a numerical artifact. 101

5.7 Time traces of particle temperatures and mass fractions demonstrate relaxation to the mean achieved by the IEM model. 102

5.8 Comparison between four different micromixing times of the NO (blue) and CO (orange) histories obtained from the partially-stirred batch reactor model with infinitely fast macromixing. Dashed lines for NO and CO represent the two different particles being used in the reactor, while solid lines for NO and CO represent the mass-averaged values. The temperature histories of each case are overlaid in yellow. Although no scales are shown, the final temperature value at 20 ms for all cases is 1975 K; the emphasis is on the temperature overshoot under finite-rate mixing conditions. The yellow solid line represents the temperature of the secondary fuel particle while the yellow dashed line represents the main burner products particle. . 103

5.9 Variation in NO and CO at the 125% CO_{eq} constraint with τ_{mix}. Notice that all CO levels are around 32 ppm corrected, which corresponds to the 125% equilibrium CO level for a 1975 K methane-air flame. Time taken to reach the CO constraint is also shown. 104

5.10 Variation of NO with the mixing time scale τ_{mix} for four sets of entrainment time scale ratios, r_τ and $\tau_{ent,main}$ = 2.0 ms. 105

5.11 Variation of corrected NO (at 125% CO_{eq} constraint) with entrainment ratio r_τ for $\tau_{ent,main}$ = 2.0 ms under different mixing rates. The variation of NO with r_τ for the infinite mixing, finite-entrainment case from Chapter 4 is included as a reference. 107

5.12 Temperature histories of each particle in the LiME reactor (entrained region). The average temperature of the entrained region and the entire system (taking into account unentrained reactants) is plotted in black dashed and solid lines, respectively. 108

6.1 Variation in computational walltime with average number of particles in the LiME reactor. 116

A.1 Variation in system NO at the 125% CO_{eq} constraint with τ_{ign} based on the maximum change in temperature gradient. 120

A.2 Variation of ignition delay τ_{ign} with secondary equivalence ratio. 121

LIST OF SYMBOLS AND ABBREVIATIONS

Abbreviations

AFS	Axial fuel staged (combustor)
BACT	Best available control technology
CAD	Computer aided design
CFD	Computational fluid dynamics
CO	Carbon monoxide
CRN	Chemical reactor network
CSTR	Continuously-stirred tank reactor
DLN	Dry, Low-NOx
DNS	Direct numerical simulation
EGR	Exhaust gas recirculation
EMST	Euclidean minimum spanning tree
FADEC	Full authority digital engine control
GRI	Gas research institute
IEM	Interaction by exchange with the mean
JICF	Jet in crossflow

LES	Large eddy simulation
LiME	Limited mixing and entrainment (reactor)
LPM	Lean premixed
ODE	Ordinary differential equations
OEM	Original equipment manufacturer
PACE	Partnership for an Advanced Computing Environment
PaSR	Partially-stirred reactor
PDF	Probability density function
PFC	Particle flow controller
PFR	Plug-flow reactor
PPO2	Proximal Policy Optimization 2
PSR	Perfectly-stirred reactor
RANS	Reynolds averaged Navier-Stokes
RJICF	Reacting jet in crossflow
RQL	Rich-quench-lean
SCR	Selective catalytic reduction

Symbols

f_s	Stoichiometric fuel-air ratio by mass
J	Jet-to-crossflow momentum flux ratio
NO	Nitrogen oxide

NO_x	Oxides of nitrogen
P	Pressure
ϕ	Equivalence ratio
ϕ_{global}	Global equivalence ratio
ϕ_{ign}	Entrained region equivalence ratio at ignition
ϕ_{main}	Main burner equivalence ratio
ϕ_{sec}	Secondary injection equivalence ratio
$\phi_{sec,norm}$	Normalized secondary equivalence ratio
ppm	Parts per million
r_m	Ratio of secondary-to-main entrainment rate
r_τ	Ratio of main-to-secondary entrainment time scale
T_{ad}	Adiabatic flame temperature
T_{air}	Air preheat temperature
T_{fuel}	Fuel preheat temperature
$\tau_{ent,main}$	Main burner entrainment time scale
$\tau_{ent,sec}$	Secondary burner entrainment time scale
τ_{global}	Global residence time
τ_{main}	Main burner residence time
τ_{mix}	Molecular mixing time scale
$\tau_{res,sec}$	Secondary burner residence time
τ_{sec}	Secondary burner residence time

SUMMARY

The ground power industry is targeting combined cycle plant efficiencies of 65% and above, which can be achieved primarily through higher combustor firing temperatures. Because conventional combustors fail to meet NO_x regulations at such temperatures, there is a pressing need for high-temperature, low-emissions combustors. In this regard, the staged combustion architecture is one such concept that shows promise due to its enhanced emissions performance and operational flexibility. The prohibitive cost of building prototypes relegates full-scale testing to the final stages of the product design cycle, while accurate models with turbulence and detailed chemistry cannot be used to efficiently explore the design space. Therefore, an efficient computational model is necessary to study a broad range of architectures.

Despite extensive research on staged combustion and the related jet-in-crossflow (JICF) problem, there is little published research regarding the minimum NO_x levels achievable by staged combustion architectures. The first contribution of this thesis presents a set of fundamental minimum NO_x levels that are obtained by wrapping a constrained optimization routine around a reduced-order staged combustor model. For a firing temperature of 1975 K which corresponds to 65% efficiency, the minimum NO levels (corrected to 15% excess oxygen) are determined to be roughly 1 ppm. The corresponding configuration is one with the most fuel-lean main burner that can autoignite the secondary stage, and the shortest secondary stage residence time that allows sufficient CO oxidation. Sensitivities of these minimum NO_x levels to operational, geometric and computational parameters are identified and discussed. The minimum NO_x levels were found to be insensitive to combustor firing temperature and overall residence time. Furthermore, a fixed combustor design was found to achieve low NO_x entitlement levels across a range of firing temperatures while maintaining low part-load emissions.

Recognizing that a turbulent flow field affects NO_x chemistry primarily through mixing,

the second contribution presents finite-rate entrainment effects on NO_x. The studies were conducted using a generic CRN model that consists of two pure fluid streams and a homogeneous entrained region in which reactants from the two streams are well-mixed. Characteristic entrainment time scales were introduced to compare entrainment characteristics based on the fundamental physical time scales, which decoupled and allowed independent specification of inlet flow rates and entrainment rates. The results are in agreement with the literature — finite-rate entrainment does indeed have a significant influence on NO_x, with some cases producing NO_x levels more than $300\times$ above theoretical limits. These trends were found to be governed by temperature overshoots in the entrained region due to burning equivalence ratios closer to stoichiometric, as well as the high dwell time at those temperatures. Further, it was found these temperature overshoots and residence time at high temperatures are heavily influenced by the autoignition delay time, τ_{ign}. This is again in agreement with previous experimental work [1, 2] that found an inverse relationship between the lift-off height and NO_x emissions in reacting jets in crossflow.

The effect of fuel-air staging under finite-rate entrainment scenarios was explored as a method by which the potentially debilitating effects of finite-rate entrainment could be mitigated. For cases where the secondary stream entrains faster than the main burner stream (which is the typical scenario in practical devices), NO was in general found to decrease monotonically with the secondary equivalence ratio ϕ_{sec} across all entrainment rates. It was found that a $\phi_{sec} < 2$ was sufficient to maintain NO_x levels below 10 ppm across all entrainment rates explored. The primary mechanism through which ϕ_{sec} affects NO_x was determined to be the ignition delay, τ_{ign}. As more air is introduced through the secondary stage, the entrained region starts at lower initial temperatures, thus increasing τ_{ign}. This increase in τ_{ign} again influences the temperature overshoots and residence time spent at high temperatures such that NO_x emissions are reduced. Thus the main takeaway from this study is that air injection in the secondary stage, as well as other methods of delaying secondary stage autoignition, are of crucial importance when designing staged combustors.

The finite-entrainment work culminated in a constrained optimization study for a prescribed main and secondary entrainment rate, in which the minimum NO level was found to be $\sim$3 ppm. These results are promising for the staged combustion architecture because it shows that even under finite-rate entrainment limitations, the design space still allows for NO_x levels that are lower than even the theoretical NO_x limits for the LPM architecture.

The consensus is that better JICF mixing leads to lower NO_x emissions, but little work has been done to characterize the effects of large-scale entrainment and small-scale mixing on NO_x in isolation. The third contribution of this thesis presents the development of a reduced-order Lagrangian model — the Limited Mixing and Entrainment (LiME) reactor — that is designed to accurate represent the evolution of a batch of reactants in a combustor under finite-rate mixing *and* entrainment. The LiME reactor is essentially a non-uniform collection of small, homogeneous reacting particles whose interaction based on a set of rules emulates small-scale mixing. It is a performance-oriented model, and is capable of leveraging parallel computing architectures to integrate the network of particles simultaneously. Molecular mixing is simulated based on the Interaction by Exchange with the Mean (IEM) model through interacting Lagrangian particles. Preliminary validation studies were performed to verify that the implemented IEM model enforces the conservation equations and converges each particle's thermodynamic state to the mean system state according to the prescribed mixing time scale τ_{mix}. Studies performed under the assumption of infinitely fast entrainment showed little influence of the mixing time scale τ_{mix} on NO_x levels. However, a study performed to characterize the combined effects of finite-rate mixing and entrainment demonstrated that mixing can be a significant determining factor under finite-rate entrainment scenarios. This is especially true when the secondary stream entrains much faster than the main burner stream, where the slowest mixing case increased NO_x by more than 2x compared to the infinite mixing case. However, slower small-scale mixing was found to be *beneficial* in entrainment-limited scenarios where overshoot temperatures were high and high-temperature dwell times are long. Therefore, a key takeaway

from this study is the importance of capturing the *combined* effect of finite-rate large-scale entrainment and small-scale mixing in staged combustor NO_x prediction.

CHAPTER 1
INTRODUCTION

1.1 Motivation

Between now and 2040, the burgeoning global population and a growing global economy will lead to a projected rise in energy use of 30%. This is equivalent to adding another China *and* India to today's global demand [3]. Despite the rapid growth of and heavy investment into renewables and energy storage, natural gas continues to play an essential role in the electricity generation mix for the foreseeable future [4]. In addition to playing a base load role where renewables are unavailable, natural gas-fired turbines also take on peaking duties where the generated power is tuned to meet local peak electricity usage [5].

In terms of natural gas-fired plants, the current workhorse is the gas-turbine based combined cycle plant, providing around 20% of all electric energy worldwide [6]. For a typical gas-turbine engine (Brayton) cycle with a cycle efficiency of around 40%,[1] the main source of inefficiency is the remaining thermal energy from the combustor exhaust that cannot be converted into mechanical energy by the turbine. A combined cycle plant provides drastically improved cycle efficiencies by using the otherwise wasted heat from the gas turbine to generate steam and drive a steam (Rankine) cycle.

Thermodynamic cycle analysis shows that while combined cycle efficiency is a function of both the gas turbine efficiency η_{gt} and steam turbine efficiency η_{st}, i.e. $\eta_{cc} = \frac{\text{Power out}}{\text{Heat energy in}} = \eta_{gt} + \eta_{st} - \eta_{gt}\eta_{st}$ [6], the efficiency is primarily dependent on the turbine inlet temperature (TIT) — the temperature of the combustor exhaust provided there is no cooling or dilution between the combustor exit and the turbine [7]. As such, the main driver behind improved power generation efficiencies from combined cycle plants has been the

[1] η_{gt} = Turbine power output/Heat input rate

steady increase in firing temperatures throughout the past three decades [8]. This positive relationship between turbine inlet temperature and thermal efficiency is shown in Figure 1.1. Today, the best combined cycle plants have efficiencies of roughly 63%, which is a great improvement compared to the 47% levels when the technology was just being adopted in 1985. These impressive efficiency values are enabled in part by lean premixed (LPM) combustors that produce low NO_x emissions even without post-combustion scrubbing. The long-standing industry-wide goal of 65% efficiency and above can be attained by further pushing turbine inlet temperatures to 1975 K and beyond [9]. The foregoing statement has been referred to as a "brute-force" approach to improve cycle efficiencies with two major hurdles [10]:

1. Materials limitations — superalloys currently in use require too much cooling at elevated temperatures
2. Excessive NO_x emissions limits — at these elevated temperatures, the thermal pathway for NO_x becomes active and results in such excessive NO_x emissions that even the theoretical minimum NO_x levels for LPM combustors fails to meet today's NO_x requirements, which can be as low as 2 ppm in developed countries [8]. This will be discussed in the next section.

Advances in materials technology and developments in high-temperature materials such as *ceramic matrix composites* show great promise in helping overcome the first hurdle. This work, on the other hand, focuses on the second hurdle — NO_x. It is therefore appropriate at this point in the discussion to provide a background on NO_x and offer some justification for the second hurdle to higher turbine inlet temperatures.

1.2 Literature Review

1.2.1 Oxides of Nitrogen: A Brief Introduction

In the mid 1940s, the effects of photochemical air pollution were first encountered in the Los Angeles area [12]. It was not until the 1950s when the culprit behind the Los Angeles

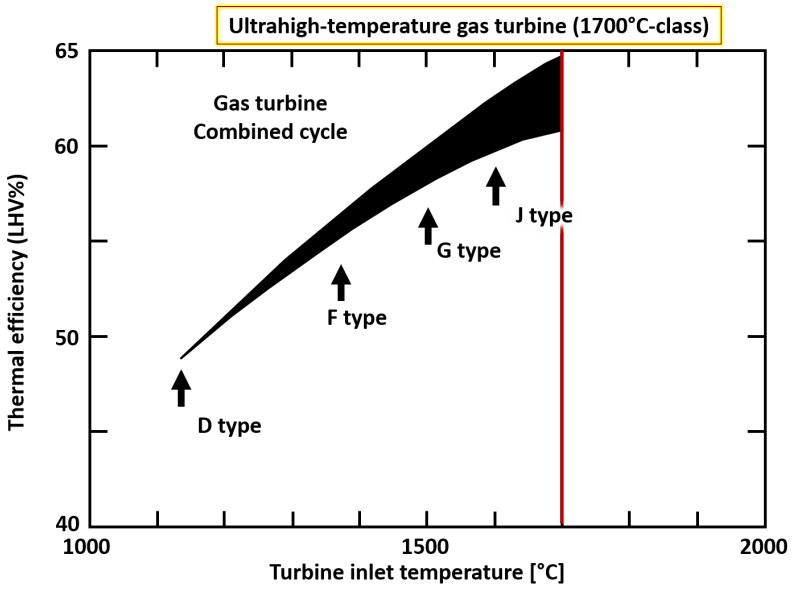

Figure 1.1: Plot that illustrates the positive relationship between turbine inlet temperature and thermal efficiency. The temperature corresponding to 65% efficiency is 1700 °C (roughly 1975 K). Figure reproduced from [11].

photochemical smog was determined to be unburned hydrocarbons and nitrogen oxides emitted from automobiles [13]. Emissions legislation on state and federal levels, such as the Clean Air Act, were initiated in the mid-1950s and subsequently amended over the years with more stringent requirements and more specific areas of emphasis [14]. Today, NO_x emissions are almost entirely attributable to the production of energy, and energy-related NO_x emissions are still increasing on a global scale due to the higher rate of increase in emissions from developing countries compared to the volumetric decrease seen in certain developed countries [15].

Nitrogen oxide (NO, IUPAC: nitrogen monoxide), nitrogen dioxide (NO_2), and nitrous oxide (N_2O) are the primary oxides of nitrogen in the atmosphere [16]. The first two species are collectively referred to as NO_x, and are primary pollutants that are emitted into the atmosphere typically as products of high-temperature combustion. In addition to NO_2 being produced through combustion processes, it is also formed in the atmosphere photochemically from NO [12].

NO_2 is a toxic gas and can contribute to the production of particulate matter (nitrate

aerosols) and ozone, both of which contribute to air pollution — the source of around 3,000,000 deaths around the world each year [17]. Furthermore, NO_x also contributes to acid rain, while N_2O is a greenhouse gas which contributes to global warming and climate change [16].

Reaction Mechanisms

A brief summary is now presented regarding the chemistry behind nitrogen oxides, with substantial references from Bowman [16], Glassman [12], and Turns [18].

The main sources of NO in hydrocarbon fuel combustion processes are [19]:

1. Oxidation of atmospheric nitrogen (N_2) via the *thermal NO (Zeldovich) mechanism*
2. "Early" production of NO via the *prompt/Fenimore mechanism*
3. The N_2O-intermediate mechanism which is most important in fuel-lean, low-temperature conditions
4. The NNH mechanism, which is most important in fuel-rich flames [20]

Post-flame NO_x

NO formation from atmospheric nitrogen in the high-temperature post-flame zone is generally attributed to the thermal NO pathway. The elementary chain reactions that constitute the kinetic route of thermal NO formation were first proposed by Zeldovich to be the following:

$$\mathrm{O} + \mathrm{N_2} \rightleftharpoons \mathrm{NO} + \mathrm{N} \tag{1.1}$$

$$\mathrm{N} + \mathrm{O_2} \rightleftharpoons \mathrm{NO} + \mathrm{O} \tag{1.2}$$

Today, this mechanism is frequently extended with the reaction

$$\mathrm{N} + \mathrm{OH} \rightleftharpoons \mathrm{NO} + \mathrm{H} \tag{1.3}$$

to form the *extended* Zeldovich mechanism. [18]

The rate-limiting step for the Zeldovich mechanism is the breakdown of atmospheric nitrogen in Reaction 1.1. This is because a significant amount of energy is required to break the triple bond found in N_2, and because the supply of N required by Reaction 1.2 is dependent on Reaction 1.1. Thus, the production of NO by the Zeldovich mechanism can only progress as fast as N_2 can be broken down into NO and N. Due to the relatively large activation energy of Reaction 1.1, this reaction has a strong temperature dependence, and a generally accepted rule of thumb in the industry is to consider the Zeldovich mechanism at temperatures above 1800 K [18].[2]

An approximate formula that shows the relationship between *thermal* NO, temperature, oxygen concentration and residence time can be derived from [16] using reaction rate constants presented by Hanson and Salimian in [21]. This relation, given in Equation 1.4, provides key insights into the NO_x-abatement methods available for thermal-NO_x-limited systems and will thus be called upon in later sections.

$$[NO] \propto [O][N_2]e^{-38{,}379/T}\tau_{res} \tag{1.4}$$

Flame/Prompt NO_x

A fascinating narrative of historical research in "flame" NO_x, differing interpretations of "prompt" NO_x, and the various proposed reactions to explain in-flame NO_x formation can be found in Glassman [12]. While initially defined by Fenimore in 1970 to be the non-zero NO_x value at a burner surface,[3] prompt NO is today mainly attributed with the elementary reaction

$$\mathrm{HCN + O \rightleftharpoons NCO + H} \tag{1.5}$$

[2]Recall that thermal NO_x is a key motivator of this work, as the temperatures required to meet cycle efficiency targets are well above 1800 K.

[3]The measured axial profile of NO_x along the burner centerline that was extrapolated back to the burner surface [22]

whose products NCO and H subsequently react and lead to the formation of NO through atomic nitrogen N. The sources of the non-zero NO_x value at the burner surface can be attributed to:

1. nonequilibrium O and OH concentrations in the reaction zone and burned gas which accelerate Reaction 1.1 and in turn the thermal NO mechanism;[4]
2. a series of reactions initiated by the reactions of N_2 with hydrocarbon radicals present in and near the reaction zone culminating in Reaction 1.5 (Fenimore mechanism); and
3. the reaction of O atoms with N_2 to form N_2O which in turn reacts with other O atoms to form NO.

In a relatively recent discovery in the field of NO_x chemistry, researchers at Emory University showed that the NCN + H reaction is a major pathway to prompt NO [24]. The (very) detailed Konnov mechanism [25] implements this pathway as part of its NO_x submechanism.

1.2.2 NO_x Reduction Techniques

Steam Dilution

At one time, most gas turbine combustors typically operated in a non-premixed flame mode where fuel and air were injected separately because of their reliability, operational flexibility, and simplicity [26]. Up until the late 1980s, water or steam injection into the combustion zone was the "best available control technology" (BACT) for achieving NO_x levels on the order of 25 ppm [27]. Steam injection reduces (thermal) NO_x formation by reducing [O] through the reaction $H_2O + O \longrightarrow 2\,OH$. In addition, the reduction in temperature (i.e., the cooling effect) due to steam injection also serves to inhibit Reaction 1.1 which is highly temperature-dependent.

[4] Miller and Bowman [23] report that this is not a very important source of prompt NO in flames

Selective Catalytic Reduction (SCR)

For cases where *in-situ* control of NO_x is inadequate, cleanup of the exhaust gas using post-combustion control techniques such as selective catalytic reduction (SCR) is used. In addition to decreasing plant efficiency (which leads to increased fuel usage and carbon emissions) and increasing fine particulates from ammonia leakage (or "slip"), SCR also incurs additional maintenance costs and causes a solid waste problem [16]. Moreover, the range of operating conditions for which SCR is effective is limited [28] and its use requires the incorporation of additional control systems which further increase costs [27].

Lean Premixed Technology and Exhaust Gas Recirculation

The effort to meet increasingly stringent NO_x emissions standards culminated in the development of lean-premixed (LPM) gas turbine combustor technology [29]. Combustors implementing LPM technology, often referred to as Dry Low NO_x (DLN) combustors, are widely employed in combined cycle plants. In the LPM approach, heat release occurs at lean conditions[5] to lower flame temperatures, thereby curtailing thermal NO_x production through the Zeldovich mechanism. Furthermore, operating at a lean condition greatly reduces the concentration of hydrocarbon radicals that can contribute to the production of prompt NO [28]. This approach also employs significant premixing of fuel and air before combustion occurs in order to eliminate local hot spots where temperatures are high and thermal NO production is elevated. For example, Leonard and Stegmaier's [30] experimental results for GE's LM6000 DLN combustor demonstrated an exponential dependence of NO_x emissions on flame temperature. Furthermore, NO_x production was found to be independent of residence time at flame temperatures below 1900 K, demonstrating that NO_x emissions below this temperature were essentially limited by the NO_x produced in the flame

[5] In combustion, a common measure of the ratio of fuel to air in a combustion process is the equivalence ratio, $\phi \equiv (f/f_{stoich}$. ϕ is the ratio between the fuel-to-air ratio of a given mixture f and the *stoichiometric* fuel-to-air mixture f_{stoich}. When fuel and air react at stoichiometric proportions, $\phi = 1$. Fuel-lean conditions are conditions where $f < f_{stoich}$, i.e. when the amount of fuel in the mixture is less than that required for a stoichiometric reaction. Therefore, $\phi < 1$ under lean conditions. Similarly, $\phi > 1$ for (fuel-)*rich* conditions.

zone instead of post-flame thermal NO_x.

A sample calculation of the dependence of the NO_x emissions upon temperature for the LPM architecture is shown by the solid line in Figure 1.2 [31], calculated using a chemical reactor network (CRN) consisting of a premixed flame and a constant-pressure batch reactor (the definitions of which will be described in later sections). This calculation provides the theoretical minimum, referred to as "entitlement NO_x", that can be achieved using this approach because it assumes perfect mixing between fuel and air before the reaction zone/flame. It should be noted that Figure 1.2 gives the minimum NO achievable by an LPM combustor *of a given geometry*, mainly one with a global residence time τ_{global} (analogous to the length of the combustor) of 25 ms. This is a consequence of the assumption of perfect premixing, and is *not* the resulting solution of an optimization problem. On the other hand, determination of the *absolute* minimum NO for the LPM architecture would, in addition to requiring the same perfect premixing assumption, be an optimization problem where τ_{global} is a design parameter.

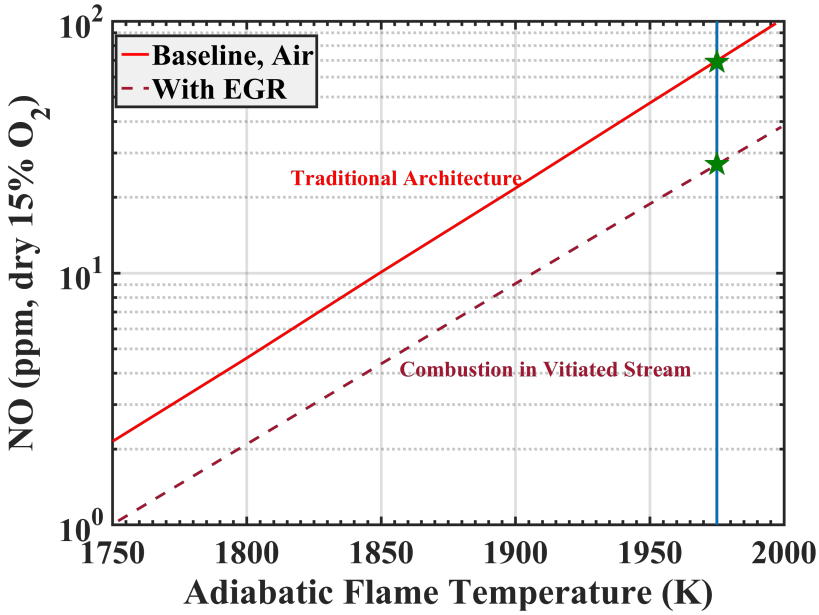

Figure 1.2: Variation in predicted minimum NO emissions from a lean premixed and EGR-type combustor with adiabatic flame temperature at 25 atm for a residence time of 25 ms, following [31].

The dashed line shown in Figure 1.2 shows predicted NO emissions against flame tem-

perature for a modified form of the LPM architecture, with exhaust gas recirculation (EGR). The EGR architecture recirculates products of combustion into the main reaction zone such that they are mixed with fresh reactants. Compared with a typical LPM combustor at the same temperature, EGR enables lower NO_x emissions due to the reduced amount of excess O_2 in the reactants which in turn reduces the O radical concentration. Together with secondary kinetic effects triggered by the increased levels of H_2O and CO_2, this change in the O radical concentration retards the rate-limiting step of thermal NO_x formation: N_2 + O $\longrightarrow$ NO + N, thus lowering overall NO_x.

Now, recall that in order to achieve 65% combined cycle efficiency, turbine inlet temperatures would need to be pushed to 1975 K and beyond. In Figure 1.2, we see that the predicted NO emissions for the EGR architecture increase exponentially with firing temperature and consequently exhibit poor temperature scaling characteristics, particularly at these desired temperatures close to 2000 K. This exponential variation of NO with firing temperature suggests that the main source of NO from LPM and EGR architectures is thermal NO (the approximate rate of production of which is given in Equation 1.4), and that it is the main culprit behind the second hurdle mentioned in Section 1.1.

1.2.3 Staged Combustion: A Promising Architecture for Low-NO_x Combustors

Staged combustion, specifically axial or longitudinal staging, is a variant on the LPM concept that enables NO abatement through the reduction of all but one parameter ($[N_2]$) in Eq. 1.4. A simplified schematic of GE's Axial Fuel-Staged combustor is shown in Figure 1.3a. Combustors with this architecture inject secondary reactants at potentially multiple locations downstream of a primary, low-temperature LPM-type combustor. This allows for:

- control over residence times τ_{res} at which [NO] is governed by Eq. 1.4 (i.e. at which T is high);
- tailoring of the radical pool to minimize [O] at high temperatures;

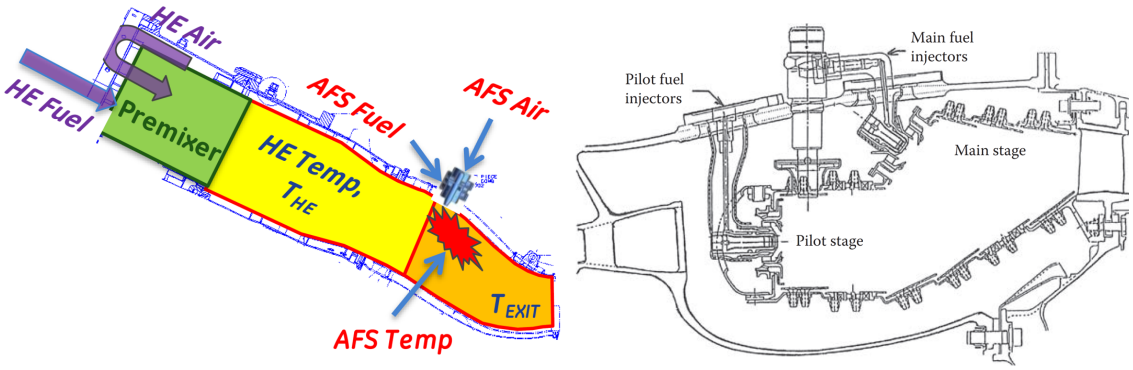

(a) GE's prototype AFS combustor, taken from [32]

(b) Pratt & Whitney axially-staged combustor [27, p. 397]

Figure 1.3: Examples of axial staged combustors by GE and Pratt & Whitney

Even as early as the 1970s, the potential for emissions reduction of staged combustion concepts were already being studied as part of NASA's Experimental Clean Combustor Program in the context of aircraft [33]. However, this technology never took off because the required control technology for the staged injectors did not yet exist [34]. With the advent of Full Authority Digital Engine Control (FADEC), increased regulatory pressures on NO_x emissions, and the continuing march toward ever higher cycle efficiencies, staged combustors are now seeing widespread research, development, and adoption. Indeed, the staged combustion architecture has been implemented commercially and patented by OEMs [32, 35, 36]. This architecture shows promise in the high combined cycle efficiency regime (i.e. high-temperatures) due to its enhanced emissions performance[6] and operational flexibility [37].

1.2.4 Mixing and Entrainment

It is widely recognized that the mixing between main burner fluid and secondary reactants is a key parameter that "makes or breaks" the staged combustor technology. Indeed, based on their experimental and numerical work in reacting jets in crossflow, Ahrens *et al.* state in [38] that mixing "is of crucial importance for low NO_x emissions" and is "favorable

[6]Certain combustor design requirements need to be met in order for improved performance, as will be shown in later sections.

in terms of NO_x reductions". The significance of mixing is evident in a 2018 patent by Siemens Energy Inc. [39] that describes the invention of a dual outlet nozzle with a circumferential layer of air shielding the secondary fuel. The inventors claim that this nozzle design enhances circumferential mixing of the secondary reactants so as to lower the peak temperature in the secondary stage, which results in reduced NO_x emissions.

This work adopts a perspective on mixing based on [40], which is the notion that at high Reynolds numbers, interactions between two streams of fluid (e.g., the transverse jet and axial crossflow in a JICF system) begin with the "large-scale intertwining of the two fluid streams" that transport packets of one fluid into the vicinity of the other. These coherent structures then break down into smaller structures, eventually resulting in fine structures at the Kolmogorov scale λ_o. At the Kolmogorov scale, molecular diffusion takes over from turbulent transport and brings the volume to a homogeneous, "well-mixed" state whereby reactions can occur. This distinction between large-scale entrainment and fine-scale mixing is a fundamental paradigm that leads to the development of the models described in Chapters 4 and 5.

For instance, consider a shear layer formed by the parallel flow of two fluids at different velocities such as that shown in Figure 1.4. The interface between the two fluids is unstable and is said to exhibit the Kelvin-Helmholtz (KH) instability. In this photograph by Broadwell and Breidenthal [40], the upper stream (dark) carries reactant A and the lower stream (light) carries reactant B, both of which participate in an irreversible reaction and form product C immediately upon mixing. Large scale coherent structures in the form of KH vortices transport reactant A from the upper stream into the vicinity of reactant B on the other side of the shear layer before any significant molecular mixing occurs at the Batchelor scale.

This is an example of an entrainment-limited flow, where by the acid-base reaction is faster than the rate at which the reactants are transported by the coherent structures. As we will see in later sections, the relationships between the mixing, entrainment, NO_x and

ignition time scales play an essential part in governing staged combustor NO_x emissions.

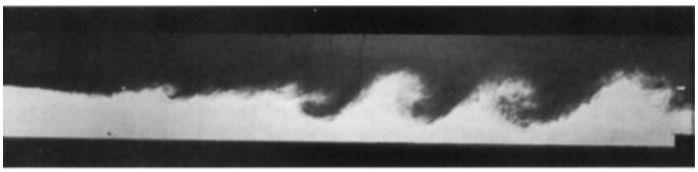

Figure 1.4: Water layer photograph of a turbulent shear layer. Before molecular mixing due to diffusion can take place, coherent structures transport the alkaline solution from the upper stream into the vicinity of the acidic solution in the lower stream and vice versa. Taken from Broadwell and Breidenthal [40].

1.2.5 Jets In Cross Flow (JICF)

The jet in cross flow (JICF) problem is intimately related with the staged combustion architecture given that transverse jets are the straightforward method by which secondary reactants are introduced into the combustor. In fact, many of the patented axial staged combustor designs utilize some form of JICF that injects secondary reactants into a crossflow of vitiated main burner products. As such, research on staged combustion often revolves around the interaction between JICF fluid dynamics and combustion processes. An example of a natural jet in crossflow phenomenon is a volcano erupting into strong winds, shown in Figure 1.5a. On the other hand, an example of man-made JICF is the emission of smoke and steam from cooling towers and smoke stacks into the atmosphere, as shown in Figure 1.5b.

Figure 1.6 shows the time-averaged flow field of an incompressible JICF and its formidable complexity. Extensive computational and experimental work has been performed to characterize the jet's trajectory [41, 42], structure [43–46], hydrodynamic stability [47–49], mixing properties [43, 45, 50, 51], etc.

Compared to the vast body of literature on non-reacting JICF, relatively little work has been performed to study *reacting* jets in crossflow especially in the context of staged combustors. These reacting flow studies mainly focus on how chemical reactions affect the JICF flow field and vice versa, specifically with regards to flame stabilization, the NO_x

(a) Volcano plume interacting with the wind — a naturally-occurring JICF.

(b) Emissions from cooling towers and smoke stacks into the atmosphere — a man-made JICF.

Figure 1.5: Examples of naturally occurring and man-made JICF phenomena.

abatement potential of staged combustors, and NO_x formation in premixed jets [37, 38, 50, 53–56]. Because very few reacting JICF studies are performed with staged combustors in mind, very few elevated-pressure results applicable to real, high-pressure combustion environments are available.

With regards to mixing, important findings by Sirignano *et al.* [2] and Sullivan *et al.* [42]) indicate that the secondary flame's lift-off height impacts emissions by influencing the extent to which the main and secondary streams mix before ignition.

1.3 Research Questions

Despite extensive research in staged combustors and the JICF problem, there is little published research in the way of the design of staged combustors from an emissions perspective. The expensive computational methods used in a majority of the foregoing work (e.g.: large-eddy simulation (LES) and direct numerical simulation (DNS)) preclude the incorporation of the detailed hydrocarbon oxidation mechanisms and NO_x formation pathways required for accurate NO_x prediction. Moreover, these computational models were only used

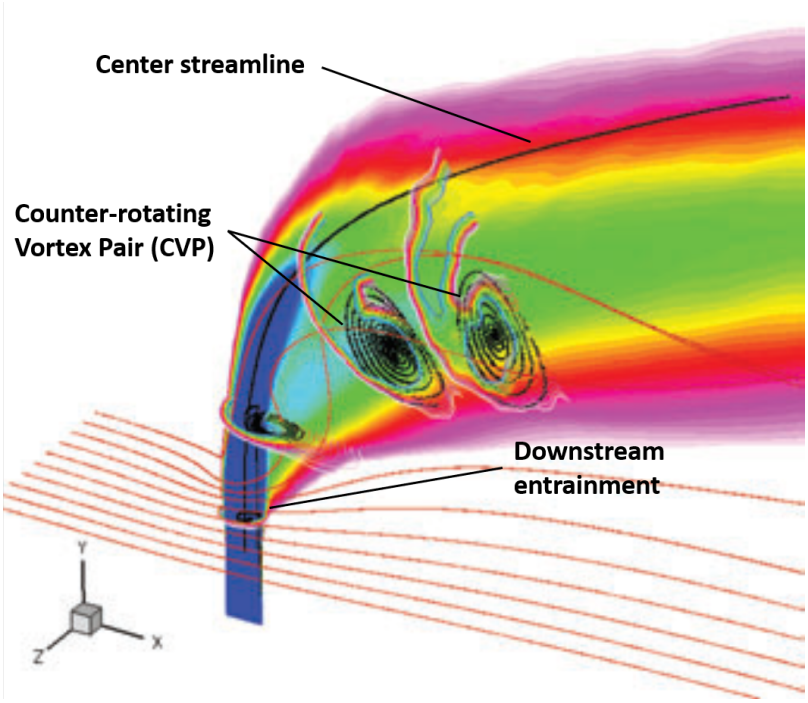

Figure 1.6: Time-averaged flow field of a typical (incompressible) JICF taken from Mahesh [52]. Contours of vertical velocity are shown, with blue indicating regions of high vertical velocity and red indicating regions of low velocity.

in conjunction with experimental methods and measurements in a "post-dictive" manner for deeper explorations into various aspects of the JICF problem. The same can be said about the reduced-order models that have been used [37, 53, 56] to substantiate experimental and high-fidelity CFD studies — they were used to study specific sub-problems, tailored to match the results and flow field from a particular test rig of simple geometry.

Consequently, there is a lack of published work that examines and quantifies the minimum NO_x achievable by the staged combustion architecture. In other words, Figure 1.2 presents the theoretical minimum for an LPM combustor of 25 ms residence time as mentioned before, but the question of ***how much staging can lower theoretical limits*** remains unanswered.

An understanding of these fundamental limits is important for both OEMs and academic researchers to focus and allocate resources towards staged combustor R&D efforts. This is analogous to how the efficiency of various ideal thermodynamic cycles (e.g., the

Brayton cycle) can help engineers determine whether or not an engine design is efficient, and how much more effort should be put into further optimizing the design. These minimum NO_x levels will also provide regulators with guidance regarding emissions standards. For example, if slightly higher NO levels are required to allow OEMs to design higher temperature systems that do not require SCRs, then avoiding the reduced efficiencies associated with SCR could bring about a greater net decrease in CO_2 emissions. Furthermore, identification of the combustor configuration that enables minimum NO_x will inform various design choices that influence the chemical kinetics and fluid mechanics within the combustor. The first research question of this work is hence defined.

Research Question 1

For a given firing temperature and residence time, what are the minimum theoretical NO_x limits for the staged combustion architecture? How much lower is this fundamental limit than that of current architectures?

Research Subquestion 1

What is the configuration that enables a staged combustor to achieve these theoretical minimums? What are the underlying physical processes enabling this configuration to achieve these values?

With advanced manufacturing and control technologies, the concept of staged combustion can be further extended to more complex geometries in contrast to those found in the literature. For example, *continuous/multi-point axial injection of fuel, air, and other reactants* along the length of the combustor vastly expands the design space (i.e. provides more "knobs" which an engineer can turn to meet certain objectives) and further pushes the boundaries of NO reduction through Equation 1.4. Because of the cost associated with building and simulating such complex systems, herein lies a novel, unexplored frontier of which conventional methods prevent efficient exploration. That being said, a new method-

ology is in order to efficiently study the concept of a continuous axial staged combustor from an emissions and operability perspective — one that can explore the emissions performance of conceptual designs without being tied down by the need for specific geometries or flow fields.

The possibility of such a method has been established in [57] albeit for NO_x emissions in aircraft engine design. In this approach, a *chemical reactor network*[7] (CRN) is developed to match a prescribed flow field and used to perform the detailed chemical calculations required for NO_x prediction. While chemical reactor network models are typically used to study combustion phenomena and predict yield in a chemical process, the novelty in [57] lies in the fact that CRN models are used in a hybrid fashion to overcome the computational cost limitations preventing CFD calculations of reacting flows from being used in design space exploration. This opens up a multitude of multidisciplinary design optimization methods such as large parametric variations and the creation of generalizable emissions models. With this in mind, we arrive at two further research questions.

Research Question 2

Can a chemical reactor network (CRN) model of an axial multi-staged combustor be developed which allows for efficient parameter space exploration, sensitivity studies, and design optimization? Can such a model achieve this enabling performance while still providing reasonable fidelity and prediction accuracy for the chemical time scales governing NO_x production?

Research Subquestion 2

What is an appropriate and computationally efficient way to capture the impact of real-world effects such as turbulent mixing and entrainment on NO_x chemistry? What is chemical reactor network's topology in the absence of a prescribed flow field?

[7] The CRN approach will be further described in Chapter 2.1.

Research Question 3

How do the minimum NO_x emissions enabled by staged combustors depend on the real-world effects of finite-rate mixing and entrainment? How does the optimal staged combustor configuration change as a result of these effects?

In addition to the novel reduced-order model developed for use in the conceptual design of staged combustors, this thesis aims to arm the combustion and power generation communities with knowledge about the impact of mixing and entrainment on staged combustor NO_x emissions, which will hopefully result in a more efficient and focused design process. In addition, the optimization studies presented herein will provide engineers with an example on tractable methods by which to parameterize the otherwise formidable staged combustor design space.

1.4 Thesis Organization

The remaining portions of this thesis are organized as follows. Chapter 2 introduces the cornerstone upon which this thesis is built — chemical reactor network (CRN) modeling. It provides a background on the fundamental equations behind the chemical reactors used in this study, and introduces the software toolkit used to numerically solve these fundamental equations — Cantera. Descriptions of a generic CRN staged combustor model are given, with special emphasis placed on the main burner model that will remain unchanged throughout this thesis.

Chapter 3 presents answers to the first research question of fundamental minimum NO_x levels enabled by the staged combustor architecture. First, the key assumptions for this work are presented. Using a chemical reactor network model based on these assumptions, the potential for NO_x reduction in a staged combustor is illustrated through preliminary parameter sweeps. Then, the minimum NO_x results obtained by wrapping a commercial optimization toolkit around the aforementioned CRN model are presented. The sensitivities

of these minimum NO_x levels to operational, geometric, and computational parameters are discussed.

Chapter 4 describes the effects of finite-rate entrainment of the main and secondary streams on NO_x emissions from a staged combustor. Once entrained, the main and secondary streams are assumed to be instantly mixed at a molecularly level. In this chapter, the main burner model remains the same, but a different model for the secondary stage is adopted to relax the infinite mixing assumption and allow for entrainment rates to be specified independently of the inlet flow rates. Entrainment time scales are introduced as a method of specifying entrainment characteristics, and the effect of varying entrainment time scales on NO_x emissions is characterized. NO_x emissions results from a parameter study across the secondary equivalence ratio are also presented. Finally, minimum NO_x results from an optimization problem under entrainment constraints are shown in Chapter 4.

Chapter 5 presents a further relaxation of the infinite-rate molecular mixing assumption. That is, a novel model that incorporates *both* the effects of finite-rate convective entrainment and finite-rate diffusive (molecular) mixing is presented. Chapter 5 first discusses the motivation behind this model, before delving into the details behind its implementation. The implementation considerations for computational efficiency of this model as well as potential for parallelization is discussed. Finally, preliminary results obtained using this model illustrate the combined effects of finite-rate entrainment and mixing on NO_x emissions in a staged combustor.

Chapter 6 summarizes the key findings of this thesis, discusses the contributions of this work, and provides recommendations for exciting future work based on the reduced-order models described herein.

CHAPTER 2

APPROACH

2.1 Elements of Chemical Reactor Network (CRN) Modeling

In many cases, the inclusion of detailed chemical kinetics in conventional CFD methods is too computationally expensive to be practical, thereby requiring reduced-order approaches to simplify complex problems into tractable ones. Consequently, CRN models are widely employed to model combustion processes, with some example uses being to investigate chemical kinetic rates, predict combustor emissions, and analyze combustor performance [19, 57–64]. These are situations where the problems being studied are highly dependent on chemical processes and thus require the calculation of detailed, finite-rate chemical kinetics.

The present work dealing with staged combustor NO_x emissions is one such instance where two chemical time scales need to be modeled with utmost accuracy in order to capture the correct trends. Unsurprisingly, the first chemical time scale is related to the rate at which NO_x is produced — τ_{NO_x}. Because CRN simulations make use of detailed chemical mechanisms, one would expect NO_x production rates to be more accurate than that of reduced chemical mechanisms, which exclude unused reactions in order to reduce run times in reacting CFD simulations. Secondly, the results from [2] and [42] indicate that the ignition time scale, τ_{ign} is a significant factor that influences emissions in staged combustors that employ JICF. It has been shown that CRN simulations are good indicators of the dominant combustion regime in the secondary stage of staged combustors under various operating conditions [65], which includes autoignition, flame propagation and flame propagation assisted by autoignition. This is in part due to the use of detailed finite-rate chemical mechanisms, which accurately represent radical formation rates that play a key

role in autoignition.

In the CRN approach, the flow field being considered is simplified into several zones which are approximated by one or several zero/one-dimensional chemical reactors — mathematical representations of corresponding laboratory reactors that are frequently used to study chemical kinetics [66]. Although this simplification immensely reduces the computational cost associated with solving a coupled flow and chemical model, it introduces unknown model parameters to describe flow rates between the various zones. Indeed, Fogler [67, p. 871] describes this approach as requiring "a certain amount of art", and Yousefian [68] emphasizes that CRN construction is based on an engineer's skill and experience in partitioning the flow field. An example of a CRN developed from a combustion flow field is shown in Figure 2.1. In this case, chemical reactors are situated in a flow field obtained a non-reacting CFD simulation for the given geometry.

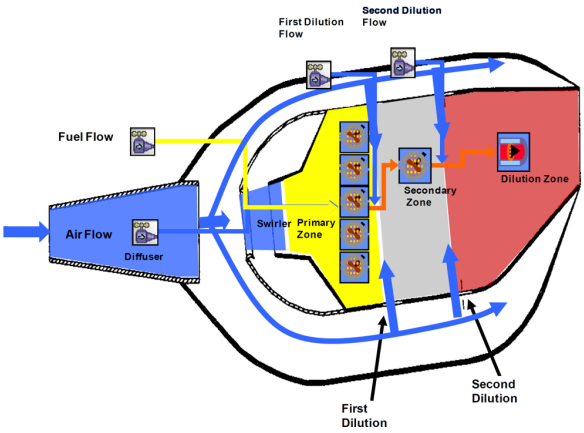

Figure 2.1: Example CRN composed of Perfectly-Stirred Reactors (PSRs) and Plug-Flow Reactors (PFRs) developed using a prescribed combustor flow field. (Taken from Mavris [57])

The primary reactor to be used in this work is based on a *constant-pressure batch reactor*. Traditionally, a batch reactor, as its name implies, models the reactions taking place within a batch of homogeneous reactants inside a reactor without any inflow or outflow. Because it is a closed system, the batch reactor is characterized by a fixed amount of mass.

Therefore, the conservation of mass is

$$\frac{dm_k}{dt} = \dot{\omega}_k \, W_k \, V \tag{2.1}$$

where m_k is the mass of the kth species (kg), $\dot{\omega}_k$ is the molar production rate (or chemical source term) due to chemical reactions (mol m^{-3} s^{-1}), W_k is the molecular weight of the kth species (kg mol^{-1}), and V is the volume of the reactor (m^3). A more convenient form of the conservation of mass uses the mass fraction of each species, $Y_k = m_k/m_{total}$, which is a dimensionless number. Dividing Eq. 2.1 by m_{total} thus yields

$$\frac{dY_k}{dt} = \frac{\dot{\omega}_k \, W_k}{\rho} \tag{2.2}$$

where $\rho = m_{total}/V$ is the density of the system.

The energy conservation equation is used to calculate the temperature of the batch reactor at each time step. For a constant pressure system, it is written in terms of the system enthalpy, $H \equiv U + PV$.

$$H = \sum_{k=1}^{N_{sp}} m_k h_k \tag{2.3}$$

$$\begin{aligned} \frac{dH}{dt} &= \sum_{k=1}^{N_{sp}} h_k \frac{dm_k}{dt} + \sum_{k=1}^{N_{sp}} m_k \frac{dh_k}{dt} = 0 \\ &= m_{total} \sum_{k=1}^{N_{sp}} h_k \frac{dY_k}{dt} + m_{total} \sum_{k=1}^{N_{sp}} Y_k \frac{dh_k}{dt} = 0 \end{aligned} \tag{2.4}$$

$$\cancel{m_{total}} \sum_{k=1}^{N_{sp}} h_k \frac{dY_k}{dt} = -\cancel{m_{total}} \sum_{k=1}^{N_{sp}} Y_k \frac{dh_k}{dt} \tag{2.5}$$

where h_k is the enthalpy per unit mass of the k-th species. Substituting dY_k/dt with the species conservation equation in Eq. 2.2 and assuming that $h_k = h_k(T, P)$, Eq. 2.5 can be

expressed as

$$\sum_{k=1}^{N_{sp}} h_k \frac{\dot{\omega}_k W_k}{\rho} = -\sum_{k=1}^{N_{sp}} Y_k \left(\frac{\partial h_k}{\partial T}\Big|_P \frac{\partial T}{\partial t} + \frac{\partial h_k}{\partial P}\Big|_T \cancelto{0}{\frac{\partial P}{\partial t}} \right) \tag{2.6}$$

$$= -\sum_{k=1}^{N_{sp}} Y_k \left(c_{p,k} \frac{\partial T}{\partial t} \right) \tag{2.7}$$

where $c_{p,k}$ is the constant-pressure specific heat of the k-th species per unit mass. Rearranging to solve for temperature, we obtain

$$\frac{\partial T}{\partial t} = -\frac{1}{\rho c_p} \sum_{k=1}^{N_{sp}} h_k \dot{\omega}_k W_k \tag{2.8}$$

where c_p is the mass-averaged constant-pressure specific heat of the batch reactor. For a state vector

$$\phi = \{T, Y_1, Y_2, ...Y_{N_{sp}-1}\}^T, \tag{2.9}$$

a system of ODEs governing the evolution of the thermochemical state of the batch reactor is

$$f = \frac{\partial \phi}{\partial t} = \left\{ \frac{\partial T}{\partial t}, \frac{\partial Y_1}{\partial t}, \frac{\partial Y_2}{\partial t}, ..., \frac{\partial Y_{N_{sp}-1}}{\partial t} \right\}^T \tag{2.10}$$

The transient simulation of a batch reactor is performed by numerically integrating Equation. 2.10, using data regarding the possible reactions for a given set of chemical species and their corresponding reaction rates to calculate $\dot{\omega}_k$. Here, the simulation is performed with the open-source Cantera software package [69], which in turn uses the CVODE solver from the Sundials library [70] to integrate the system of (stiff) ODEs.

It is important to note that while the batch reactor is normally defined to be a closed system, Cantera's implementation of the generic constant pressure reactor allows for inlets and outlets to be added to the reactor. In addition to enabling these reactors to function as

perfectly-stirred reactors (PSRs) with a prescribed residence time, these inlets and outlets allow for reactants to be added (or products to be removed) at any given time. The mass flow rates, heat loss rates, and volume change can also be varied as functions of time as well.Although a batch reactor with inlets/outlets is known as a *semibatch reactor* in the chemical reaction engineering community [71], it will be referred to as a batch reactor or constant pressure reactor in this thesis to maintain consistency with the Cantera implementation.

2.2 Staged Combustor Reactor Network Model

The reduced-order chemical reactor network (CRN) approach described in Section 2.1 is used to predict NO_x in this thesis. At the highest level, a staged combustor CRN model is partitioned into two sections — a main burner stage and a secondary stage. This section details the implementation of the main burner stage in Cantera and describes a generic version of the secondary stage.

2.2.1 Main Burner Stage

The nominal main burner in the staged combustor represents a state-of-the-art lean premixed combustor — a configuration typical of staged combustors currently in operation [32]. This combustor is in turn modeled as a one-dimensional premixed laminar flame followed by a constant pressure batch reactor. NO_x chemistry in premixed flames has been found to be dominated by temperature effects and is therefore relatively insensitive to turbulence effects [26]. While in-flame NO_x formation rates increase with turbulence level, this effect is negated by the decrease in flame length (i.e., residence time) as turbulence increases [72]. In addition to this justification for the use of a laminar (instead of a turbulent) flame regime at the main burner head end, the laminar flame model increases fidelity in the simulation of NO_x chemistry within a flame, which is affected by the diffusion of reactants and products into the reaction zone.

A one-dimensional laminar flame reactor, including the one implemented in Cantera, solves the conservation equations for mass, momentum, species, and energy on a given domain to obtain a steady-state solution along a single spatial coordinate, x. In particular, Cantera discretizes the flow equations in a finite-difference scheme and uses a hybrid Newton/time-stepping algorithm to solve the resulting nonlinear algebraic equations for a steady-state solution. Adaptive grid refinement is performed to resolve flame profiles, while adaptive grid coarsening can remove unnecessary grid points to improve performance. The spatial coordinates on which the flame is located are cast into temporal coordinates for the purposes of calculating residence times.

The flame solver specifies the flame location through an estimate of the temperature profile. Consequently, flames of different conditions (equivalence ratio, preheat temperature, etc.) are situated at roughly the same region in the spatial domain. The temporal locations of flames of different equivalence ratios, however, differ due to the difference in flame speeds, leading to situations whereby lean flames have unreasonably long ignition times while near-stoichiometric flames ignite almost instantaneously. A definition of the point in the spatial domain that represents the initial time τ_0 should therefore maintain consistency across various equivalence ratios and enable the accurate representation of flame physics on a temporal basis. The point of peak formaldehyde (CH_2O) concentration is a good indicator of the beginning of the preheat zone in methane-air flames of different equivalence ratios, which allows the entire flame to be captured in the time domain. As such, defining τ_0 to be the point of peak CH_2O ensures that all cases with burning solutions ignite before the end of the main burner, i.e., within the total residence time of the main stage (τ_{main}).

Because the domain used in the laminar flame calculation may be too small and may thus end at a residence time less than τ_{main}, a constant pressure batch reactor is used to allow the main burner to achieve the required main stage residence time. In this case, the batch reactor is initialized with the state of the flame at the end of the domain τ_{end} before

being allowed to react for the difference in residence times, i.e. $\tau_{main} - \tau_{end}$. Another situation where the batch reactor is used following a laminar flame is when the grid points in the laminar flame solution are too coarse to obtain the desired τ_{main} even though $\tau_{end} > \tau_{main}$. The batch reactor is thus initialized with the laminar flame solution at the residence time smaller than but closest to τ_{main} and allowed to react for $\tau_{main} - \tau_{closest}$.

2.2.2 Secondary Stage

In all the reactor network models described in this thesis, the fundamental building block of the secondary stage is the generic constant-pressure batch reactor. In the ideal case discussed in Chapter 3, the secondary stage is a true batch reactor with specified initial conditions. In the limited entrainment model of Chapter 4, the secondary stage consists of *multiple* parallel reactors with inflows and/or outflows, one reactor for the main stage fluid and another to represent an entrained region. Finally, the finite-rate mixing model of Chapter 5 uses a large network of parallel reactors that are allowed to interact based on prescribed micromixing rules.

2.2.3 Chemical Mechanism

The default chemical reaction mechanism used to provide chemical kinetic, thermodynamic, and transport data in the simulations is GRI-Mech 3.0 [73]. This mechanism has been optimized for natural gas combustion modeling, and includes detailed chemistry on NO formation and reburn, for instance. Because of its relatively small size (53 species and 325 elementary reactions) and its inclusion with many major combustion modeling software packages such as CHEMKIN and Cantera, this mechanism has found widespread adoption in the combustion community, particularly in industry. Indeed, Yousefian *et al.* [68] found that nearly 45% of the literature they studied in their review of CRN modeling employed the GRI-Mech 3.0. In Section 3.6, other chemical mechanisms (Konnov 0.6 [25] and UCSD [74]) are examined to investigate their impact the on prediction of minimum

NO_x levels.

2.3 Design Optimization

With one of the major objectives of this work being to determine the minimum NO_x achievable by staged combustors, a constrained minimization problem can be formulated as follows:

$$\begin{aligned} &\underset{x}{\text{minimize}} \quad f(x) \\ &\text{subject to} \quad g_i(x) \leq b_i,\ i = 1, \ldots, m. \end{aligned} \tag{2.11}$$

where $f(x)$ is the CRN simulation used to obtain NO_x emissions, x is the vector of design variables, and g_i represents the i-th constraint.

It is important to discuss the constraint function $g(x)$. Section 3.3 illustrates an inverse relationship between NO and CO emissions, which necessitates the discussion of minimum NO for a given constraint on CO. This allowable level of CO manifests as a constraint $g(x)$ in the NO optimization problem posed above, and directly affects the minimum NO_x levels identified by the optimization algorithm.

In this thesis, the default constraint on CO is for CO emissions to not exceed 125% of the equilibrium CO levels, CO_{eq}, based on the overall combustor equivalence ratio. In Chapters 4 and 5, this constraint is used as a consistent basis from which NO levels are reported. The premise behind allowing 25% more CO at the combustor exit is to anticipate further CO burnout beyond the combustor (e.g., in the engine turbine or nozzle).

CHAPTER 3

THEORETICAL MINIMUM STAGED COMBUSTOR NO_X LEVELS

As stated in Chapter 1, axially fuel-staged (AFS) combustors have been implemented commercially and patented by OEMS, and studies have analyzed their performance from both emissions and operability standpoints. However, there is a lack of published work that quantifies the minimum NO_x entitlement for staged combustors and characterizes its sensitivity. As such, this chapter answers the first research question of this thesis — for a given firing temperature, what are the minimum theoretical NO_x limits for the staged combustion architecture — and in doing so accomplishes Thesis Objective 1.

We first look at the key assumptions required to identify theoretical minimum NO_x values and proceed to discuss the secondary stage CRN model used to predict emissions under these key assumptions. The necessity of a constraint on CO in order to reasonably define a minimum is shown through the inverse relationship between NO and CO. Minimum NO values obtained using this model, as well as their sensitivities to geometric and operational parameters are then presented. An upper bound is placed on the NO values by modeling the worst-case scenario where all the secondary fluid reacts stoichiometrically with all the main burner products.

3.1 Ideal Secondary Stage Model

Two key assumptions that are required for a staged combustor to achieve the absolutely lowest NO_x levels are that:

1. The main burner stage itself has to be producing the minimum levels of NO_x. This is achieved by assuming that the main burner is an ideal version of the state-of-the-art lean premixed combustor in which fuel and air are completely premixed before any

reactions occur.

2. In the secondary stage, products from the main burner and fresh reactants from the secondary inlet are completely mixed before any reactions occur.

The secondary stage of an ideal staged combustor model that assumes infinite mixing between secondary reactants and main burner products can be separated into two parts:

1. A non-reacting mixer between the products of the first stage and the reactants injected at the second stage.

2. A constant-pressure batch reactor in which the mixture is allowed to react but does not experience further entrainment of vitiated products from the main burner and secondary (injected) reactants.

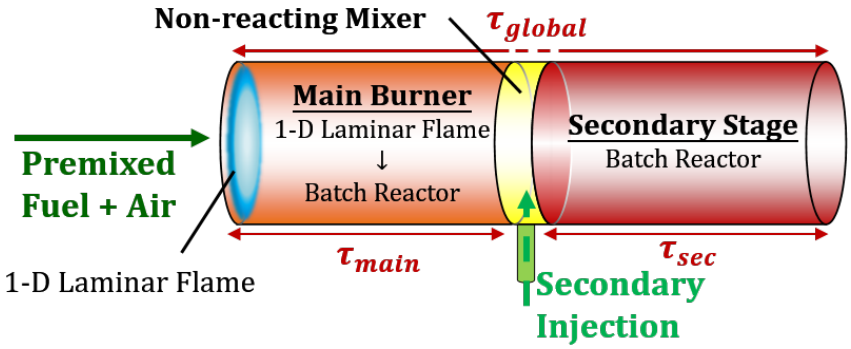

Figure 3.1: Simplified diagram of an axial fuel-staged combustor and the chemical reactors used to model it.

By perfectly mixing the main burner products and the secondary reactants, NO_x emissions can be minimized because there are no regions in the reaction zone where combustion occurs at near-stoichiometric equivalence ratios (i.e., at high temperatures). This is a similar approach to the LPM technology used to minimize NO_x in the main burner, with the only difference being that one of the "reactants" is now a stream of vitiated products of lean combustion instead of air. Indeed, the premixed combustion approach is stated by Sattelmayer [75] to ensure spatial homogeneity in the temperature distribution within the

reaction zone, thus reducing local high-temperature regions where NO_x production rates are high. As such, while one may question the practicality of such an idealized model, it is in fact important to isolate chemical kinetic effects from aerodynamic effects when studying the minimum NO_x entitled by chemistry alone for a given combustion regime. In other words, this approach is justified because the objective of this chapter is to predict *theoretical minimum NO_x levels* rather than to model a given embodiment of the staged combustion approach.

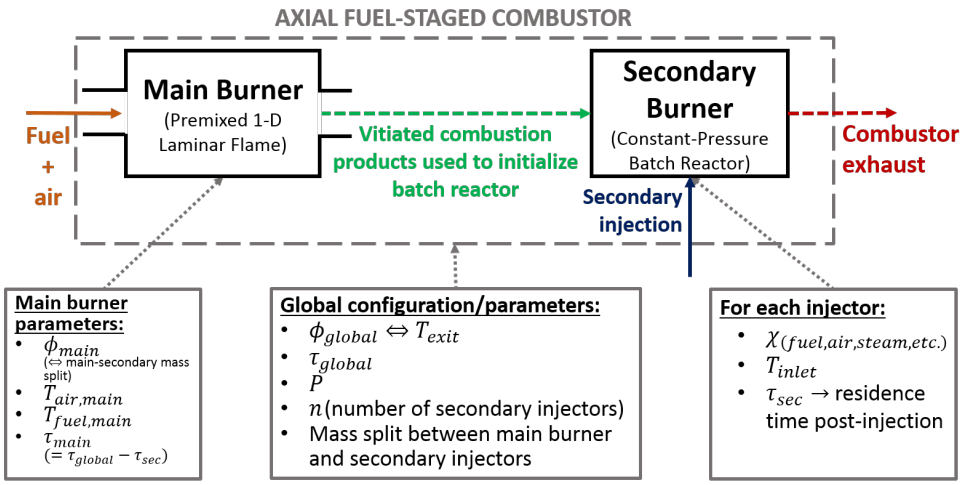

Figure 3.2: Block diagram of ideal staged combustor CRN model showing various combustor design parameters used in the optimization problem.

Figure 3.2 shows the list of design parameters that can be varied at the main burner stage and each secondary stage using the model described in Section 3.1. In the current chapter, for a given ϕ_{global} and τ_{global}, the parameters are chosen such that the only design variables are τ_{sec} and ϕ_{main}. That is, the vector x in Equation 2.11 is a vector of size 2.

Only AFS combustors with two stages are simulated herein, i.e., the only reactant being injected in the sole secondary stage is pure fuel. Nominal gas turbine operating conditions are used in the model, thereby fixing the values of the various combustor design parameters (see Figure 3.2 for parameter list). Unless stated otherwise, the values of these parameters are shown in Table 3.1.

Table 3.1: Constant parameters used to simulate gas turbine operating conditions.

Parameter		**Value**
Number of secondary reactors, n		1
Fuel		CH_4 (Natural Gas)
Pressure, P	(atm)	25
Fuel temperature, T_{fuel}	(K)	300
Air preheat temperature, T_{air}	(K)	650
Nominal global residence time, τ_{global}	(ms)	20

3.2 NO_x Reduction Potential of Staged Combustion

To emphasize the primary reason for the potential for NO_x reduction in AFS combustors, Figures 3.3a and 3.3b show comparisons between a typical LPM combustor and four different staging configurations, all with the same final temperature of 1975 K. The four configurations include two main burner equivalence ratios ϕ_{main} (0.5 and 0.6) and two secondary reactor residence times τ_{sec} (5 ms and 2 ms).

The results shown in Figure 3.3 demonstrate that the axial fuel-staged architecture can achieve varying levels of NO reduction depending on the choice of ϕ_{main} and τ_{sec}. Specifically, these results indicate, as might be expected, that a staged combustor with a leaner main burner (i.e., lower ϕ_{main}) and later injection of secondary fuel (i..e, lower τ_{sec} is beneficial to the reduction of NO.

As a reminder, this lowering of NO_x emissions is obtained under the assumption that any additional fuel rerouted from the main burner to the secondary stage for a fixed ϕ_{global} is mixed with vitiated products from the first stage before any new reactions can occur. As can be seen in Figure 3.3b, the thermal NO formation rates (i.e., dNO/dt) remain essentially constant across each configuration, so long as the equivalence ratio (and temperatures) of the post-combustion zones are the same. The small dip in temperature and NO at the injection point is due to an increase in the mass of the system resulting from the addition of (relatively cold) fuel at the secondary injector.

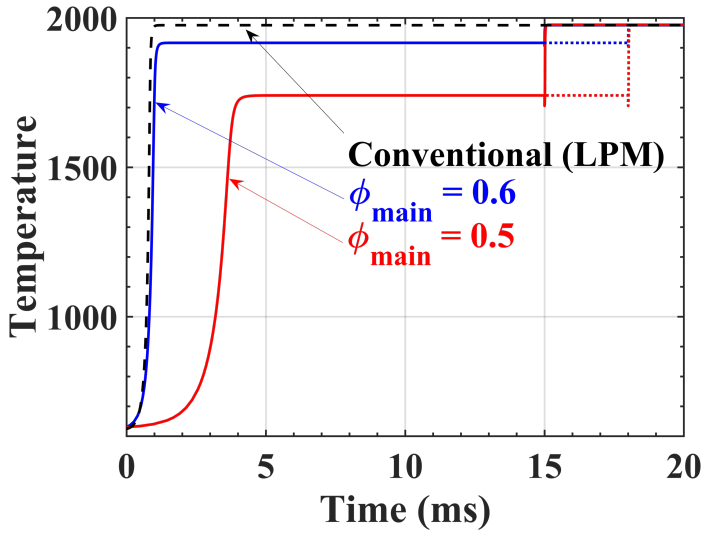

(a) Temperature time trace

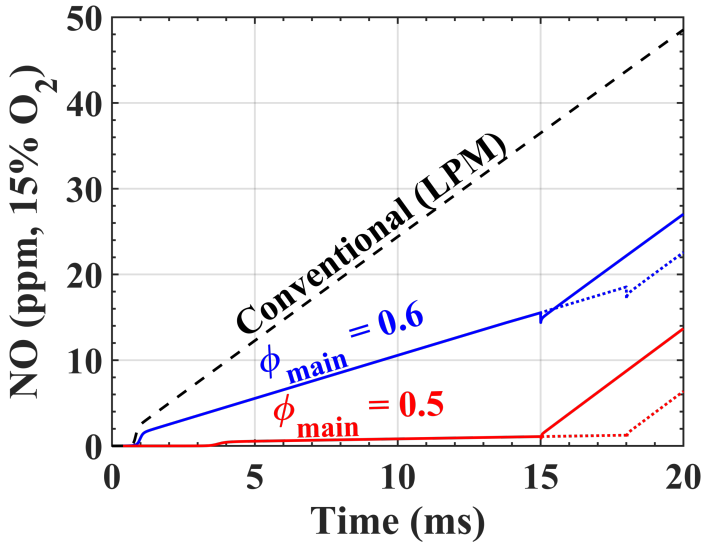

(b) NO Time Trace

Figure 3.3: Temperature and NO time traces calculated using axial fuel-staged combustor model at 1975 K exit temperature. Solid lines represent cases where τ_{sec} = 5 ms while dotted lines represent cases where τ_{sec} = 2 ms.

3.3 Parametric Studies

This section describes parameter sweeps across the two design variables ϕ_{main} and τ_{sec} that are performed to determine the minimum achievable NO for the axial fuel-staged combustion architecture and the corresponding configuration.

Results are only shown for NO because NO has been found to be the largest constituent

in the predicted NO_x values. For reference, N_2O/NO ratios are approximately 0.5 and 0.07 for configurations where NO levels are 1 ppm and 10 ppm, respectively, while NO_2 levels are negligible ($NO_2 < 0.01$ ppm) for all conditions tested. Emissions results are corrected to reference conditions (15% O_2, 0% H_2O, i.e. dry) as per regulatory emissions standards according to the following equation (shown for NO)[1]:

$$\chi_{NO,\ dry} = \frac{\chi_{NO}}{1 - \chi_{H_2O}} \tag{3.1}$$

$$\chi_{NO,\ dry,\ 15\%O_2} = \chi_{NO,dry}\left(\frac{\chi_{O_2,air} - \chi_{O_2,15\%}}{\chi_{O_2,air} - \chi_{O_2,dry}}\right) \tag{3.2}$$

where $\chi_{O_2,air} = 20.9\%$.

3.3.1 Fuel Split Sweep

Figure 3.4 shows the dependence of NO and CO emissions as the fuel split is varied. NO production is reduced when more fuel is diverted from the main burner to the secondary stage. This reduction in NO production rate is due to the reduction in the main burner temperature, as stated in Equation 1.4 and evidenced in Figure 3.3a. For a fixed T_{exit} (again set to the baseline value of 1975 K) and τ_{sec}, the main burner equivalence ratio was varied from 0.4 (close to the lean flammability limit) to 0.65 (the limiting LPM case where all fuel is injected at the main burner).

Thus, a very lean main burner is indeed a desirable configuration for the NO minimization at high temperatures. An NO improvement is achieved across the entire range of main burner equivalence ratios, although lower ϕ_{main} values produce diminished returns. Furthermore, the CO emissions remain at equilibrium levels across the fuel-split range for the studied τ_{sec}, indicating that CO relaxation at 1975 K is completed in less than 1 ms. It should be noted, however, that this analysis does not take into account stability (static

[1]The purpose of this correction is twofold — to enable a baseline condition at which to compare different sets of experimental data, and also to indicate that less NO_x production is expected from combustors which burn less fuel [27].

and dynamic) issues that can arise when operating highly lean combustors and which could thus limit the achievable main burner equivalence ratio.

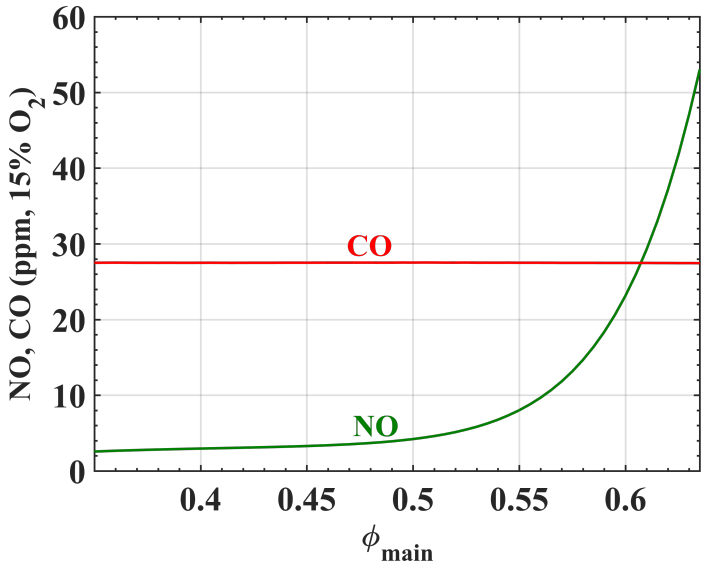

Figure 3.4: Variation of NO and CO emissions with ϕ_{main} for $T_{exit} = 1975K$ and $\tau_{sec} = 0.5$ ms .

3.3.2 Secondary Stage Residence Time Sweep

In addition to a dependence on ϕ_{main}, Figure 3.3b also reveals that NO production in an axial staged combustor is dependent on the residence time of the secondary stage, τ_{sec}. For a fixed global residence time, varying τ_{sec} implies earlier or later injection of the secondary fuel. Figures 3.5 and 3.6 shows the results of a parameter sweep on this post-injection residence time τ_{sec} at a fixed ϕ_{main} of 0.42, which enables identification of the minimum NO configuration for a given firing temperature. As expected, the results in Figure 3.5 indicate reduced NO emissions for shorter post-injection residence time. Down to $\tau_{sec} \approx 100\ \mu s$, NO emissions decrease linearly with residence time; below 100 μs, the NO produced in the secondary stage is so low that thermal NO is no longer the dominant contributor. In contrast to the NO behavior, the CO levels at the combustor exit remain constant until τ_{sec} is less than roughly 0.2 ms, below which CO emissions rapidly rise. While complete mixing of fuel with the hot main burner products enables rapid combustion, at a short enough

residence time, the secondary reactor does not achieve complete CO oxidation.

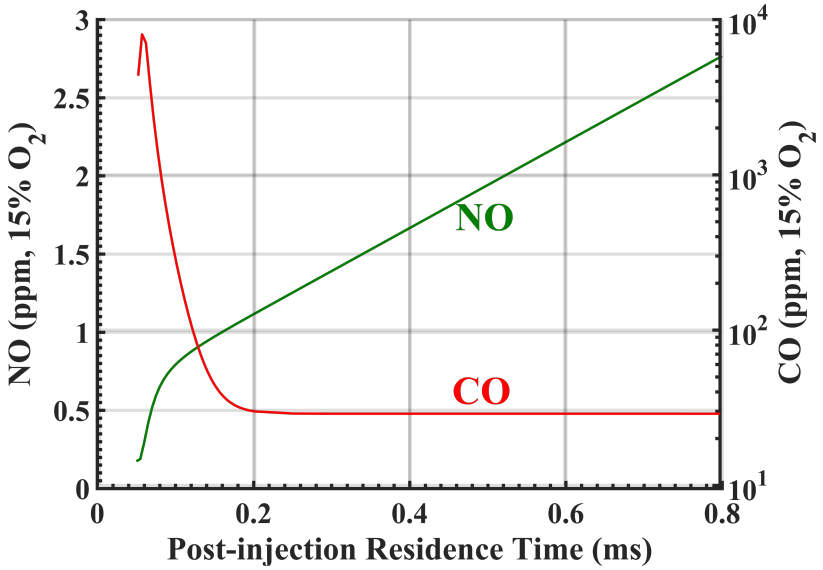

Figure 3.5: Variation of NO and CO emissions with τ_{sec} for $T_{exit} = 1975K$ and $\phi_{main} = 0.42$.

Figure 3.5 shows the familiar trade-off between NO and CO emissions performance, which is more clearly presented in Figure 3.6 where NO emissions are plotted against CO emissions for a range of secondary stage residence times. A single objective NO minimization problem is invalid without suitable constraints on CO and also the combustor exit temperature because certain configurations will give trivial, non-igniting results with low NO *and* low CO. Thus, one must enforce some constraint that ensures satisfactory combustion performance in order to find a minimum NO configuration. One constraint that will be explored is to require that the CO emissions are no more than 125% of the equilibrium CO levels, CO_{eq}, based on the overall combustor equivalence ratio ϕ_{global} (and equivalently the associated adiabatic combustor exit temperature). The other constraint is for the combustor exit temperature to be within 2% of the adiabatic flame temperature, thus ensuring that only non-trivial solutions are obtained. The equilibrium CO level (corrected) and 125% CO_{eq} constraint are indicated in Figure 3.6 with vertical dashed lines.

Of course, the more CO one is willing to allow at the combustor exit, the lower the achievable NO emissions. Therefore, should this problem be framed as a multi-objective

optimization to minimize both NO and CO, the bend in Figure 3.6 before CO starts to increase can be interpreted as a Pareto frontier where no combination of ϕ_{main} and τ_{sec} "dominates" or is necessarily "better" than the other. That is, NO cannot be reduced without increasing CO and vice versa. In this case, the preceding NO minimization problem with a CO constraint is simply the *epsilon constraint method* where the Pareto Frontier is mapped out by changing the CO constraint (i.e. shifting the dashed red line in Figure 3.6 left and right).

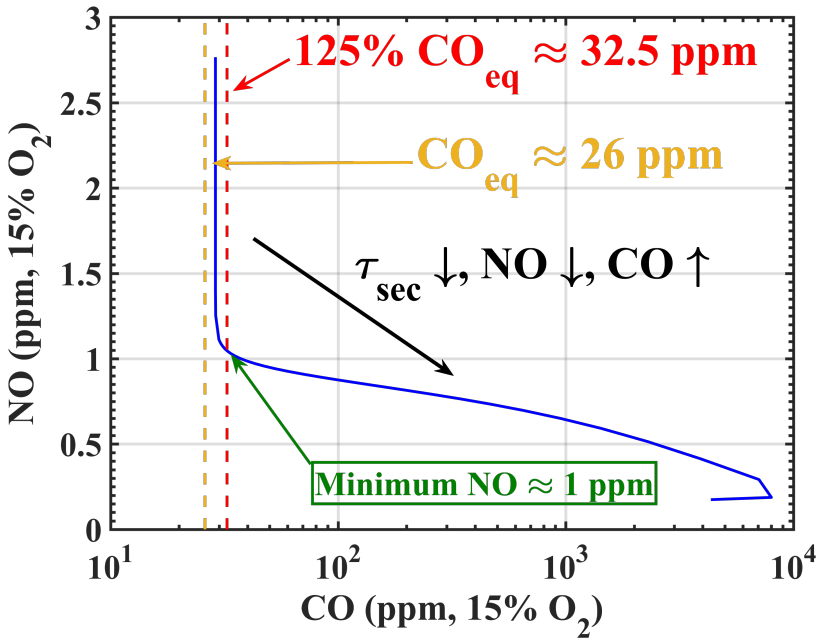

Figure 3.6: Variation of NO emissions versus CO emissions at various τ_{sec} values for $T_{exit} = 1975K$ and $\phi_{main} = 0.43$.

3.4 Minimum NO

3.4.1 Optimization Algorithm

As noted in Chapter 2, the minimum theoretical NO_x is a strong function of the constraint function $g_i(x)$, in particular with regards to CO emissions, as they interact strongly in terms of residence time and temperature. A set of different constraints on allowable CO can arise in lieu of part load operability, and the resulting design changes are discussed in Section

3.7. From Equation 2.11, we can express the optimization problem for each ϕ_{global} as:

$$\min_{\phi_{main},\tau_{sec}} \quad \text{NO}(x) \tag{3.3}$$

$$\text{s.t.} \quad \text{CO}(x) \leq 1.25 \times \text{CO}_{eq}(\phi_{global}) \tag{3.4}$$

$$\frac{|T - T_{ad}(\phi_{global})|}{T_{ad}(\phi_{global})} \leq 0.01 \tag{3.5}$$

where $x = \{\phi_{global}, \phi_{main}, \tau_{global}, \tau_{sec}, T_{fuel}, T_{air}, P\}$, with ϕ_{global} specified and constant parameters given in Table 3.1. Due to the non-linear nature of the objective function NO(x), discrete design variables such as the number of injectors and the main burner equivalence ratio ϕ_{main} [2] and the relatively quick run time of the CRN model, a genetic algorithm (GA) is used to solve this minimization problem. Specifically, the Darwin algorithm included ModelCenter calls the staged combustor CRN simulation as its objective function to minimize NO_x subject to CO and combustor exit temperature constraints.

3.4.2 Fundamental NO_x Limits

Using the Darwin Algorithm in ModelCenter with the 125% CO constraint, a set of fundamental NO_x limits are predicted across a range of firing temperatures for τ_{global} = 20 ms. Optimization is performed independently for each temperature, so each result represents a single-point optimized configuration of ϕ_{main} and τ_{sec}. The resulting NO_x entitlement curve is shown in Figure 3.7 alongside curves for the theoretical minimum NO_x entitled by an ideal LPM combustor with residence time of 10 ms. Figure 3.7 shows that the minimum achievable NO_x for an axial fuel-staged combustor is less than 1 ppm for firing temperatures below 1975 K, and on the order of 1 ppm at temperatures of 1975 K - 2000 K. The significance of this result should be emphasized; it demonstrates that *there is no fundamental reason that prevents very low NO emissions from being achieved for elevated flame*

[2] Because laminar flame calculations are expensive, flame libraries are first generated for a finite range of ϕ_{main} which are then used to initialize the batch reactor in the main burner simulation.

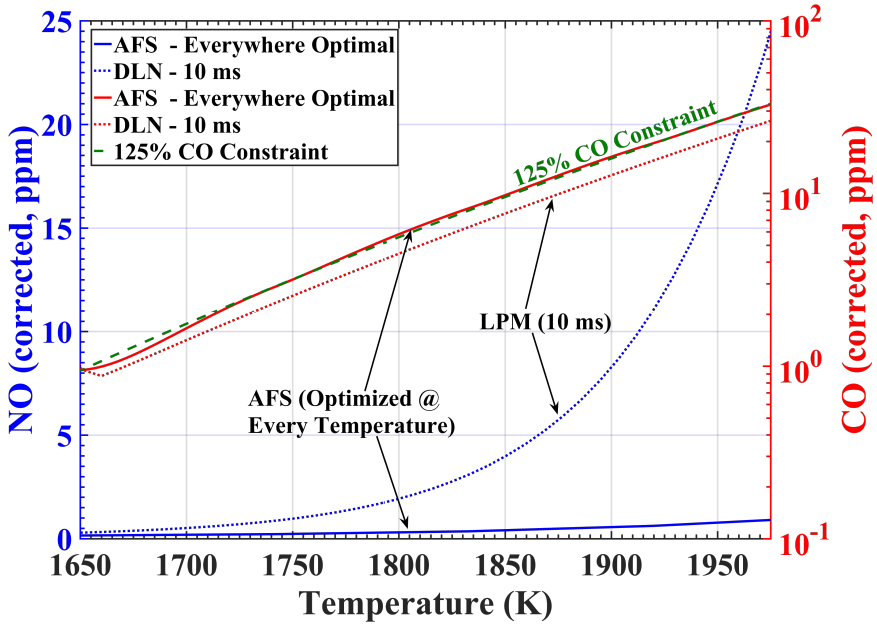

Figure 3.7: Predicted minimum NO and corresponding CO levels at different firing temperatures for the AFS architecture (blue solid line), subject to 125% CO constraint, alongside predictions for a conventional LPM combustor (dashed line).

temperature devices. Indeed, given that the most stringent NO emissions today are on the order of 3 ppm @ 15%O_2, this result indicates that the staging approach has significant potential to enable both increased efficiencies and reduced NO emissions.

Figure 3.8 shows the corresponding configurations for the minimum NO results shown in Figure 3.7. As discussed in Section 3.3, the optimum main burner equivalence ratio is one that minimizes NO production in the main burner yet maintains operability. The optimum ϕ_{main} results in Figure 3.8 show that the optimal main burner in a staged combustor would be operated as lean as possible without sacrificing stability and secondary stage functionality. The optimal secondary stage, on the other hand, is one with the minimum amount of residence time required for sufficient CO oxidation. This is shown in Figure 3.8, where the optimum τ_{sec} increases with decreasing firing temperature because CO oxidation is slower at lower temperatures and thus requires more residence time.

A trade-off between main burner NO, secondary stage NO, and secondary stage operability can be seen in Figure 3.8. At high temperatures, the lower τ_{sec} and higher ϕ_{main}

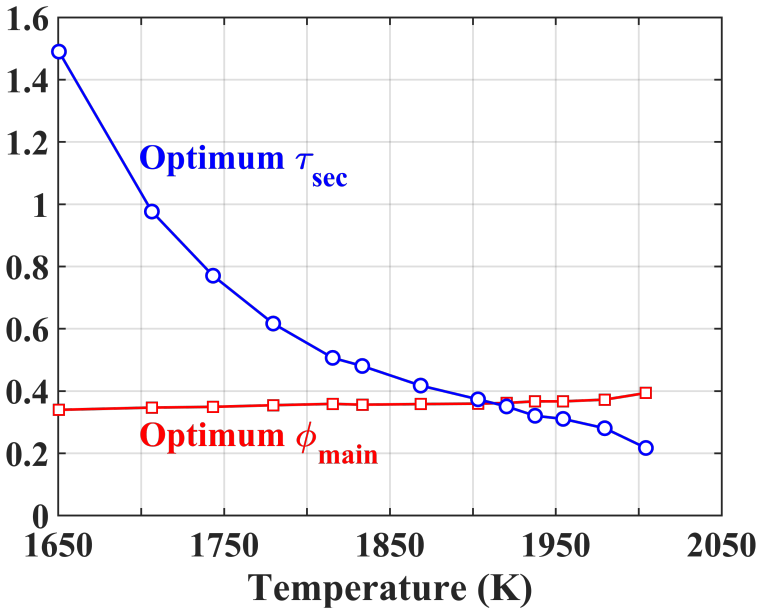

Figure 3.8: Configurations corresponding to minimum NO results for axial fuel-staged architecture.

values curtail the more dominant NO levels produced in the secondary stage (at the expense of slightly more NO from the main burner), whereas the lower ϕ_{main} and higher τ_{sec} values minimize the higher main burner NO levels and enable secondary stage autoignition at low temperatures.

3.5 Global Residence Time Sensitivity

The results presented in the previous section were for a single global residence time. The sensitivity to τ_{global} of the NO_x entitlement for staged combustion was examined by performing optimization studies for five global residence times, ranging from 5 to 25 ms. The shortest residence time studied here is comparable to minimum values obtainable in current engines. All the cases are for the target 1975 K firing temperature. As seen in Figure 3.9, the minimum obtainable NO for the AFS paradigm is essentially independent of the overall combustor residence time at the high operating temperatures required for 65% efficiency. While a conventional LPM combustor needs to be shortened to reduce NO at high firing temperatures, the AFS combustor can meet the 125% CO constraint while main-

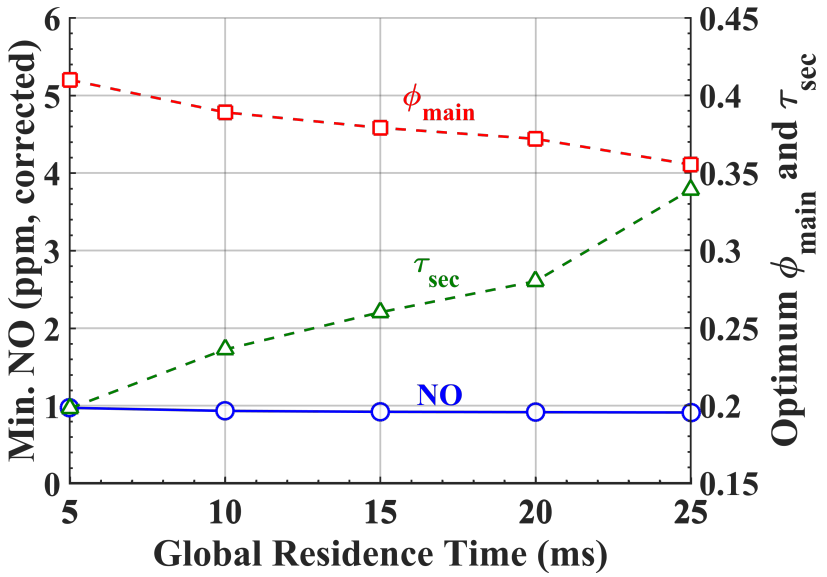

Figure 3.9: Minimum NO achievable and corresponding main burner equivalence ratio for the 1975 K AFS combustor at multiple residence times.

taining roughly the same low NO emissions without requiring residence times that may be unobtainable in practical devices. As the global residence time of the staged combustor decreases, the optimum configuration for a shorter staged combustor changes slightly, favoring a higher ϕ_{main} and lower τ_{sec} for rapid CO oxidation.

The above calculations demonstrate theoretical minimums for a single axial stage. A natural follow-on question is the extent to which further emissions improvements are achievable with multiple stages or even continuously distributed fuel injection. In the ideal case with infinitely fast mixing, configurations with multiple injection locations were tested but showed marginal benefit compared to the single injection configuration. For example, we repeated this process for two discrete axial injection points, whereby the optimum configuration resulted in an injection system where i) most of the fuel is injected in the second injector (i.e. the third stage), and ii) the second injector is placed very close to the end of the combustor, similar to the single injector configuration. The lack of improvement for multiple injection locations is likely limited to the case of fast mixing, as will be discussed in Section 3.9.

3.6 Sensitivity to Kinetic Mechanisms

A further question that must be addressed is the sensitivity of the results presented so far (both the trends and quantitative NO limits) to the reaction mechanism used, as recent studies have reported uncertainties surrounding the elementary NO reaction rates used in several widely-used reaction mechanisms [76]. This section presents calculations for several reaction mechanisms and shows that these key outcomes do not change. As a means of understanding the uncertainties in the current results based on the chosen GRI-Mech 3.0 mechanism, the same optimization routine used to obtain the minimum NO values presented in Section 4.3 was used to predict the fundamental NO limits for the AFS architecture for two other mechanisms: Konnov 0.6 [25] and UCSD [74]. Note that for each mechanism, the minimum NO results can be associated with slightly different staging configurations; the key trends in how the optimum configuration changes with operating conditions remain the same.

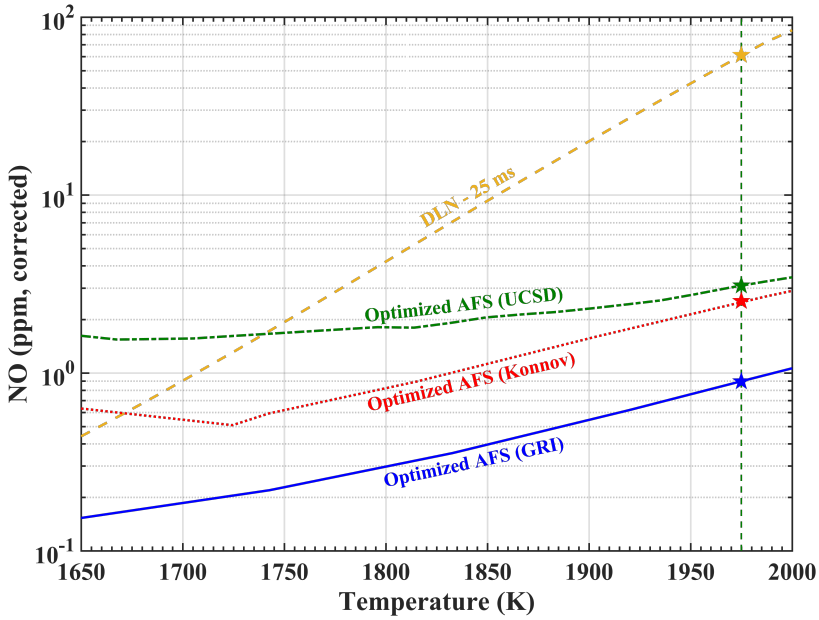

Figure 3.10: Fundamental NO limits for the staged combustor architecture at various firing temperatures calculated using three different reaction mechanisms. A conventional LPM combustor fundamental limit is shown for comparison.

As seen in Figure 3.10, the choice of reaction mechanism does influence the predicted

minimum NO levels in relative terms. The differences in absolute values, however, are small. All the optimized NO results are on the order of 1 ppm at 1975 K, regardless of the reaction mechanism. This is well below the value ($\sim$60 ppm) for the LPM configuration obtained using the GRI mechanism. It is also interesting to note that the GRI and Konnov mechanisms show more similar trends with firing temperature, though the Konnov prediction is roughly 2.5 times higher than that for the GRI mechanism. The minimum NO predicted by the UCSD mechanism is slightly higher than the Konnov result at 1975 K and shows a reduced sensitivity to firing temperature.

Figure 3.11 shows predicted NO values from the lean premixed laminar flame model used to simulate the main burner at three equivalence ratios (from 0.42-0.45), with predictions from the same three chemical mechanisms. These results correlate well with the trend shown in Figure 3.10; the UCSD mechanism predicts the highest NO emissions from the main burner, while the GRI-Mech 3.0 mechanism produces the lowest. Therefore, a significant portion of the differences observed in the minimum NO levels of Figure 3.10 are due to the differences in the predicted main burner NO emissions. As the baseline LPM NO limits shown in Figure 3.10 were predicted using the GRI mechanism, they should be considered a lower bound because the other mechanisms would produce a higher LPM NO level.

To isolate mechanism effects associated with the secondary stage (fuel injection), cases were also studied using a common data set for the main burner based on the GRI 3.0 simulations, but with different mechanisms to model the post-injection reactions. These results are presented in Figure 3.12, where the injection occurs at t = 20 ms. Analysis of the detailed results indicates that the prompt and N_2O pathways in the heat release zone of the secondary stage are the largest contributors to the differences in the predicted NO values. This is consistent with differences seen in the initial rise in NO that occurs during fuel consumption and primary heat release. By comparison, the slower rate of NO increase at later times, primarily associated here with thermal NO_x, is similar for all three mechanisms.

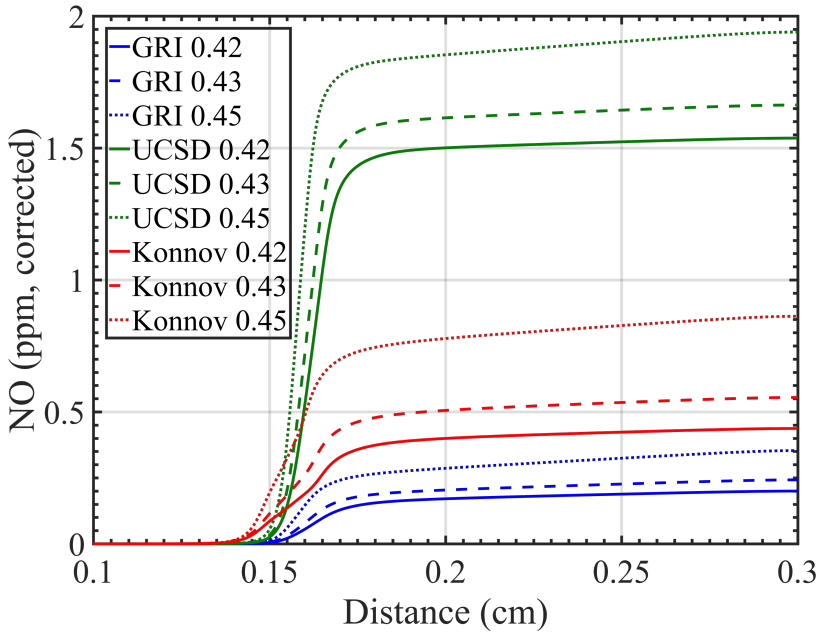

Figure 3.11: Predicted NO values for lean premixed 1-D laminar flames at various equivalence ratios using different reaction mechanisms.

The Konnov mechanism predicts the highest post-injection NO production (for the same pre-injection conditions) for two reasons: 1) it has the most rapid autoignition of the injected fuel, and thereby has the longest post-combustion residence time (which increases the thermal NO_x contribution) and 2) it has the greatest prompt NO production during the initial heat release after injection. The UCSD mechanism produced the highest overall minimum NO levels in the earlier case (Figure 3.10) primarily because it predicts the highest main burner NO.

In summary, the choice of mechanism does influence the ideal minimum NO levels for staged combustion, but the differences in absolute levels are small compared to the corresponding ideal minimum levels obtainable with a traditional LPM architecture, especially at high firing temperatures.

3.7 Multi-Point Design with CO Constraint at Part Load (1650 K)

While the foregoing results present the fundamental minimum NO levels achievable by staged combustors at various conditions such as operating temperatures and residence

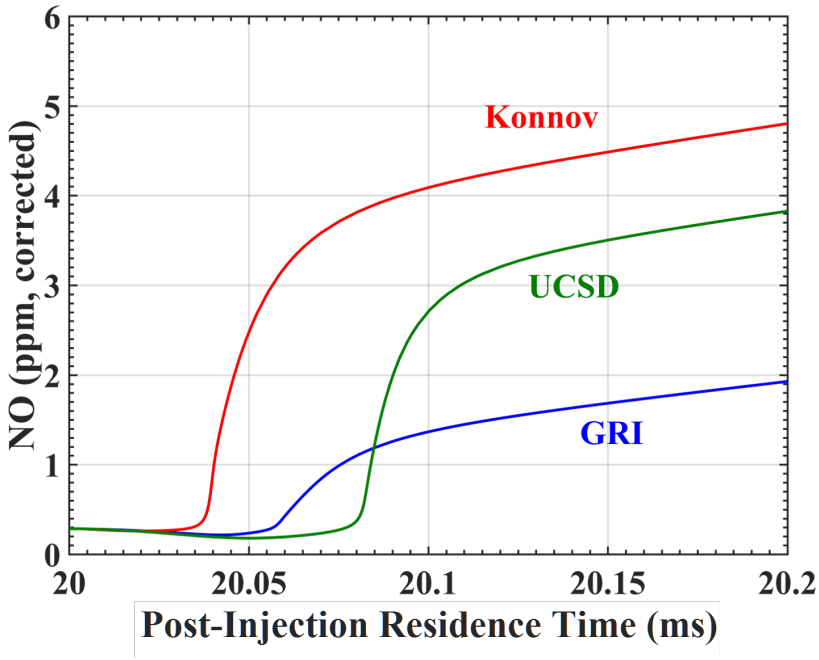

Figure 3.12: Predicted NO in the secondary stage demonstrating differences in overall NO due to variations across mechanisms of the amount of prompt NO produced at early times.

times, the optimal configurations were determined for single-point operating conditions. For instance, if one were to operate the optimal 1975 K combustor with the 125% CO constraint (i.e., maximum allowable CO of 31.8 ppm) at part-load by reducing the secondary fuel, the CO emissions could become excessive due to the lack of residence time for sufficient oxidation as illustrated in Figure 3.13.

This section explores the minimum achievable NO emissions for systems that must meet multi-point design constraints. We first explore a two-point staged combustor design by applying the same maximum CO determined by the 125% CO constraint at full load (1975 K) at a chosen part load condition (1650 K). An optimization study is performed with the objective being to minimize NO at full load, subject to the new CO constraint. In contrast to the single-point design, the optimal staged combustor design under this constraint has a higher ϕ_{main} of 0.449 and a shorter τ_{sec} of 0.158 ms. This design increases NO by 0.1 ppm at 1975 K and decreases CO emissions at 1650 K to 31 ppm compared to the 600 ppm levels seen in Figure 3.13.

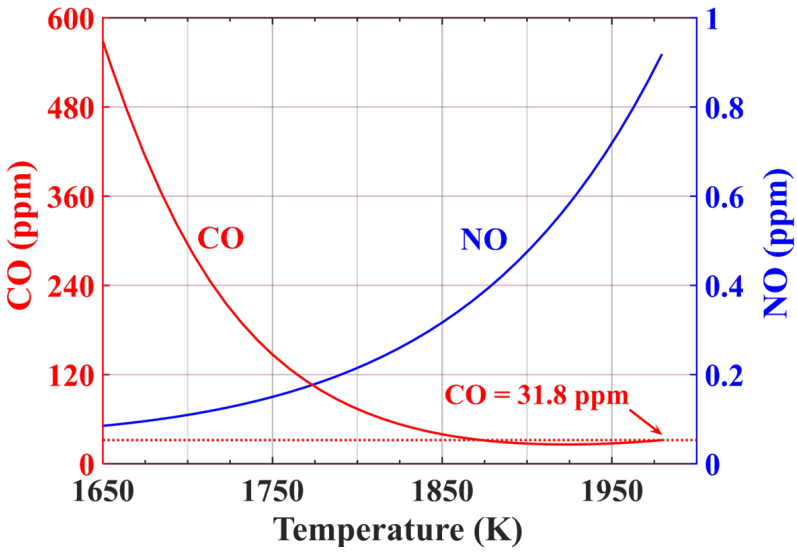

Figure 3.13: Variation in NO and CO emissions across various firing temperatures for an ideal 20 ms staged combustor optimized for the 1975 K operating condition (ϕ_{main} = 0.37, τ_{sec} = 0.28 ms).

In this configuration, the staged combustor routes almost all the fuel through the main burner at part load; ϕ_{global} = 0.45 gives an exit temperature of 1650 K, so a ϕ_{main} of 0.449 indicates that only 0.01% of the fuel is injected into the secondary burner to provide a temperature increase of only 2 K. While this solution does in fact give the minimum NO emissions under the two-point CO constraint, the improvement is insignificant compared to operation of the main burner at ϕ_{global}. Consequently, we can take the optimum ϕ_{main} to be 0.45 in which case the staged combustor would operate in LPM mode at part load (i.e., with the second stage disabled), producing only 0.8 ppm of CO at 1650 K, rather than 31 ppm.

As such, an optimized staged combustor based on the two-point CO constraint would run the main burner at the global equivalence ratio for part load and minimize the residence time of the secondary burner such that there is sufficient time for autoignition and CO oxidation at full load.

The solid lines in Figure 3.14 shows the variation in NO and CO as this newly optimized staged combustor is lowered from full load to part load. Although CO levels are

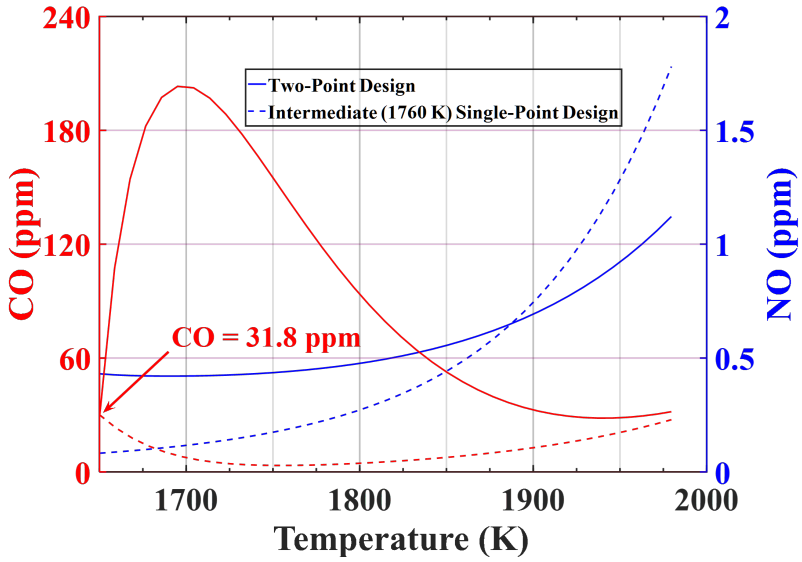

Figure 3.14: Variation in NO and CO emissions across various firing temperatures for a 20 ms AFS combustor optimized to minimize NO at full load and maintain 32 ppm CO at part load (ϕ_{main} = 0.449, τ_{sec} = 0.16 ms). The dashed lines show the variation in NO and CO across the same range of temperatures for a staged combustor optimized for minimum NO at 1760 K.

indeed below 32 ppm at both target operating points, CO levels increase to ∼200 ppm at intermediate operating temperatures between 1700 K and 1975 K because the lower temperatures in the secondary burner result in slower CO oxidation rates. In other words, while a design with a high ϕ_{main} (equal to the part load ϕ_{global}) and a very short τ_{sec} (only just long enough to enable CO oxidation to the full load 125% CO constraint) does indeed minimize NO at full load under the two-point CO constraint, the short τ_{sec} combined with the slower CO oxidation results in excessive CO emissions at intermediate temperatures.

Thus, we also consider the minimum achievable NO emissions at full load for a design that must meet CO constraints across a wide range of part load conditions. Although one could perform an optimization study to address this, a faster approach can be taken by noting in 3.8 that as the design temperature decreases, the optimum τ_{sec} increases to account for the slower CO oxidation. A single-point staged combustor design optimized for an intermediate temperature (e.g., between the full and minimum load conditions considered here, 1650 and 1975 K) can be identified with a τ_{sec} sufficiently long for acceptable

CO oxidation at all operating conditions. This design would then enable CO levels at or below the full load 125% limit for all intermediate temperatures at the expense of slightly increased full load NO emissions.

Interpolation of the results from Figures 3.7 and 3.8 shows that an AFS combustor designed for the 1760 K operating temperature (ϕ_{main}=0.35,τ_{sec}=0.69 ms) produces 32 ppm of CO at part load and less than 2 ppm of NO at 1975 K. Plotted as dashed lines in Figure 3.14, the results from this approach show that for an approximately 1 ppm penalty in NO at full load, NO emissions at intermediate temperatures can be kept in the 1 ppm range while CO levels are maintained below 32 ppm at all operating conditions. Therefore, these results demonstrate that the staged combustor architecture can achieve essentially the same fundamental minimum NO limits of an optimized single-operating point condition under multi-operating point design constraints.

3.8 Summary of Minimum NO Results

Simulation results based on a chemical reactor network were presented that explore the fundamental NO_x limits achievable by an axially fuel-staged combustor architecture. A combustor operating at 25 atm was simulated in order to represent a nominal ground power gas turbine, with a maximum CO emissions constraint of 125% of equilibrium for the corresponding full-load condition. Under ideal conditions, NO emissions near 1 ppm are theoretically achievable with staged combustors for a wide range of global residence times (5-25 ms) and firing temperatures (1650-2000 K). This range includes firing temperatures required for combined cycle efficiencies exceeding 65%. Based on a total residence time of 20 ms and a firing temperature of 1975 K, this represents a potential NO_x reduction of nearly 50 times compared to the ideal performance of conventional low-NO_x architectures. While three widely used chemical kinetic mechanisms for modeling natural gas combustion predict slightly different NO levels, the differences in the predictions at high firing temperatures are small compared to the large reduction in minimum theoretical emissions

for AFS combustors.

The single-point design configuration that minimizes NO at full-load varies with the firing temperature and global residence time, but in general the optimal architecture is one with the minimum main burner equivalence ratio that enables rapid secondary stage autoignition and the minimum secondary zone residence time required to meet the CO burnout constraint. Similar NO levels were also shown to be achievable by the staged combustion architecture for multi-point designs with emissions constraints extending from part-load to full-load operation, with the main burner equivalence ratio and secondary stage residence time chosen based on optimal results from an appropriate intermediate load condition. The optimization results presented here were for a single (secondary) injection location; more complex schemes, such as multiple discrete locations provided little benefit under the infinite mixing assumption. For finite-rate mixing between the staged injection fluid and the main burner products, however, the optimum injection scheme could potentially involve multiple discrete or continuous injection configurations.

3.9 Finite-Rate Mixing Effects

The above results constitute theoretical minima that are achievable with a single injection point. An important question is the sensitivity of these results to mixing rates, which is the key challenge associated with reducing this concept to practice. As discussed in Section 3.1, the model used to obtain the results thus far has assumed infinitely fast mixing and entrainment of vitiated main burner products and secondary reactants before reaction in the secondary stage. Furthermore, the products of reaction in the current secondary reactor never mix back with upstream reactants; they simply evolve forward in time. However, it is clear (e.g., see Ahrens *et al*. [53]) that mixing limitations can reduce the benefits of axial fuel-staging in terms of NO emissions. This is due to the formation of localized pockets in which reactants meet in near-stoichiometric proportions, forming hot-spots with temperatures that promote thermal NO production. As such, this section aims to provide

an estimate of the upper bound for the NO_x emissions of AFS combustors.

3.9.1 Secondary Stage: Worst-Case Model

As one may surmise from the foregoing results that demonstrate time and again the benefit of low temperatures on NO_x emissions, the inverse situation where combustion occurs *everywhere* at the highest temperatures should drastically elevate NO_x emissions from a system whose NO production is dominated by the thermal-NO pathway. A staged combustor for which reaction zone temperature is the highest is thus modeled as one where:

1. There is only partial mixing between with the incoming secondary reactants; *and*
2. The portion of the main burner products that mixes with the incoming secondary reactants is such that the resulting reaction between these two streams occurs at stoichiometric conditions, thus producing near-maximum reaction zone temperatures.

Such a model is shown in Figure 3.15 where the main burner products enter a gas splitter instead of a non-reacting mixer. This splitter then passes the stoichiometric amount of main burner products into the secondary reactor where locally stoichiometric reaction occurs while the remaining main burner products simply continue reacting (while most of the heat release reactions will be complete by this point, i.e. temperature is constant, NO_x production will persist as per the discussion in Section 1). At the end of the combustor, τ_{end}, the two streams are mixed in a non-reacting mixer to obtain the final mass-averaged mixture of the stoichiometric products and remaining main burner products.

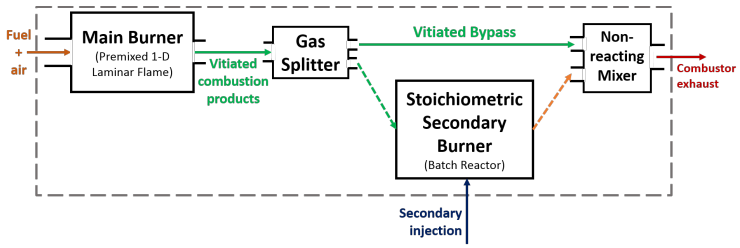

Figure 3.15: Block diagram depicting reactor network model used to study worst-case finite mixing rate effects on minimum NO_x.

3.9.2 Worst-Case NO_x Emissions

To better illustrate the worst-case reactor model, Figure 3.16 compares the time evolution of temperature between this model, the conventional LPM model, and the ideal staged combustor model with a τ_{sec} of 5 ms. The stoichiometric reactor burns at a higher temperature and thus produces more NO compared to the ideal secondary reactor. This worst-case model essentially simulates a localized stoichiometric region that persists throughout the combustor.

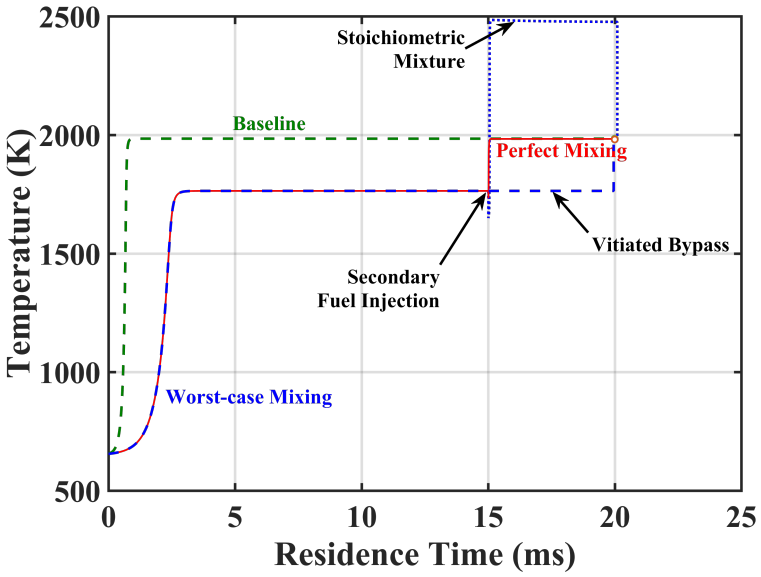

Figure 3.16: Temperature evolution of the worst-case staged combustor model with a secondary residence time of 5 ms demonstrates the high temperature at which all the fuel injected in the secondary stage burns, thereby causing excessive NO_x emissions.

Figure 3.17 shows a comparison of the NO emissions between the ideal and worst-case models using the optimized configuration found in the preceding sections. These results show that the worst-case scenario in a 1975K-optimized AFS combustor increases NO emissions by around 11 ppm. Even with this increase in NO production due to the high-temperature secondary reaction zone, the worst-case result still represents a NO benefit compared to the baseline architecture because of the short τ_{sec}. The predicted CO emissions levels, however, are around 300 ppm. This is because the CO formed in the stoichiometric reaction zone cannot oxidize further to form CO_2. As noted in the earlier section, in the

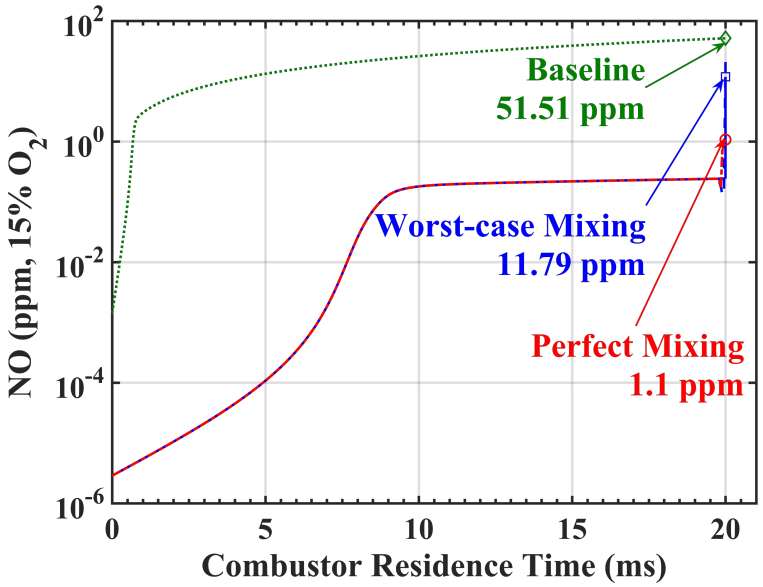

Figure 3.17: Time traces of local NO concentration for an LPM combustor (labeled "Baseline"), an ideal (at 1975 K) AFS combustor, and a worst-case stage combustor show that the worst-case staged combustor produces roughly 10x more NO than an ideal staged combustor.

infinitely fast mixing limit, a single axial-stage yields essentially optimum NO_x emissions results; essentially no benefit is achieved from multiple or continuously distributed fuel injection from a kinetics standpoint.

With finite-rate mixing, important interactions between mixing and NO_x chemistry arise that necessitate design changes in the staged combustor's geometric and operational parameters — both of which serve to define the overall chemical trajectory within the combustor. The negative impact of finite-rate mixing demonstrated in the foregoing results motivates the relaxation of the ideal mixing assumptions used in this chapter. As such, the next chapter discusses the effect of finite-rate large-scale entrainment on NO_x.

CHAPTER 4
FINITE-RATE ENTRAINMENT EFFECTS

In Chapter 3, optimization studies were performed using the a staged combustor CRN model to identify minimum NO_x levels enabled by the staged combustion architecture. To that end, the model assumed that the main burner vitiated products and secondary fuel mixed infinitely fast prior to chemical reactions. The relaxation of this assumption is the key focus of this chapter. A similar approach to Chapter 3 is taken, except the reactor model network is modified to account for finite rates of entrainment of the main, premixed stage and secondary stage fluids. This section provides a physical basis for the model, as well as the details of its implementation.

4.1 Approach

4.1.1 Generic Flow Field

As a generic example of the flow field features that exist between a staged combustor's main and secondary streams, consider the flow of a secondary jet into coflowing main burner products, as illustrated in Figure 4.1. In such a flow, large-scale coherent structures of high vorticity convectively transport main burner products and jet fluid into an *entrained region*. As the large-scale structures break down into smaller structures due to dissipation, eventually molecular diffusion dominates and brings the entrained fluid into a molecularly mixed state where reactions can occur. Thus Figure 4.1 shows a possible separation of the generic flow field into three regions: two with pure fluid (main or secondary) and the third being the entrained region containing both fluids, where small scale turbulence and molecular diffusion act to mix the fluids. It is important to note that the entrained region can in general contain pure fluid packets in addition to molecularly mixed packets, i.e., the

entrainment region is not necessarily well-mixed.

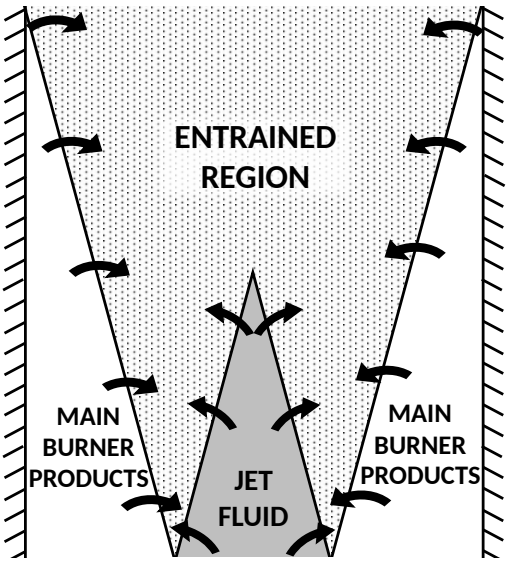

Figure 4.1: Fuel jet emitting into coflowing vitiated products and the associated entrainment of both streams. Three regions are identified in the flow field — pure jet fluid, pure vitiated products, and an entrained region.

Existing literature has shown that emissions in typical staged combustion systems are limited by large-scale entrainment rather than small-scale mixing [38], thus the present model seeks to incorporate the effects of finite-rate entrainment by large-scale structures while retaining the assumption that small-scale mixing is much faster than all other time-scales. The model used in this chapter is designed as a generic framework that allows one to simulate reaction kinetics based on physical time scales that are directly related to physical parameters.

4.1.2 Physical Parameters

The equivalence ratio at which a combustor is operated, ϕ_{global}, is given in Equation 4.1 as the (operational) fuel-to-air ratio divided by the stoichiometric fuel-to-air ratio, f_s.

$$\phi_{global} = \frac{\dot{m}_{fuel,total}/\dot{m}_{air,total}}{f_s} \tag{4.1}$$

For a staged combustor, ϕ_{global} can be expressed in terms of the fuel and air flow rates at the main and secondary stages — $\dot{m}_{fuel,main}$, $\dot{m}_{air,main}$, $\dot{m}_{fuel,sec}$, $\dot{m}_{air,sec}$. These four inlet flow rates are parameters that can either be specified directly or through variables such as ϕ_{global}, ϕ_{main}, ϕ_{sec}, and total mass flow rate.

It is important to distinguish between these flow rates and the mass entrainment rates, i.e., the rates at which the two fluid streams are transported into the entrained region. In general, entrainment rates are dependent on the inlet flow rate of each stream, as well as other parameters. For example, entrainment rates in typical jet-in-crossflow (JICF) configurations used in several staged-combustion devices also depend on additional parameters such as Reynolds number and momentum flux ratio. Due to finite entrainment rates, the pure fluid regions in Figure 4.1 exist for a finite distance before disappearing. The extent to which a pure fluid region persists in the flow field is a key physical parameter that will be taken in this work to indicate entrainment characteristics.

This distinction between inlet and entrainment rates means that the entire fluid in the entrained region can be characterized by an equivalence ratio, $\phi_{entrain}$, which is different than ϕ_{global}, though it approaches ϕ_{global} as all the pure fluid is entrained. Thus, a proper model of a staged combustor must include parameters that properly capture the inlet flow rates and entrainment rates for both main and secondary stages, or alternately ϕ_{global}, ϕ_{main}, ϕ_{sec} and $\phi_{entrain}$. Furthermore, we wish to study the effects of entrainment rate in isolation while keeping all other parameters (on which entrainment rate may be dependent) fixed, especially those parameters that directly impact NO production.

4.1.3 Secondary Stage Model

For the secondary reaction zone with finite-rate entrainment, we adopt a simple model of the flow field that enables fluid mechanics and chemical kinetics to be treated separately by casting the spatial distribution of a steady-state/time-averaged flow field into a temporal distribution. This is a Lagrangian representation of an Eulerian flow field, where we follow

a control volume as it evolves downstream. As described in Section 4.1.1, the flow field in the secondary stage is partitioned into regions of pure and entrained fluid. Here, the open system shown in Figure 4.1 is modeled as a control volume, hence the inlet mass flow rates for the pure main and pure secondary streams are represented as *masses* of reactants instead of mass flow rates. The ratios of these masses are matched to the ratio of inlet flow rates such that ϕ_{global} is maintained, whereas the total amount of reactants (representative of the total mass flow rate) is a free parameter. The total mass defines the extensive size of the system while the mass ratio governs the kinetic effects being studied.

Figure 4.2 presents a chemical reactor network implemented in Cantera to simulate the secondary stage model described above. The network contains an element for each partition in the flow field — a pure main burner stream, a pure secondary stream, and the entrained region. In the network, incoming streams of pure fluid are modeled as either non-reacting reservoirs or constant-pressure batch reactors, both being adiabatic. The main burner stream is modeled as a batch reactor in order to capture NO_x production within the main fluid in the secondary stage before it is entrained, while the low-temperature secondary stream is stored in a non-reacting reservoir. The inlet flow rates of main and secondary streams are represented as M_{main} and M_{sec}.

The entrained region is modeled as an adiabatic, homogeneous constant-pressure batch reactor with multiple inlets (this model is also equivalent to a perfectly-stirred reactor with multiple inlets and no outlet). This allows for control over the finite entrainment ratios while simulating an infinite mixing rate. These inlets, implemented using Cantera mass flow controllers, are connected to the main burner and secondary streams with prescribed mass flow rates $\dot{m}_{ent,main}$ and $\dot{m}_{ent,sec}$. As noted previously, the inlet flow rates and mass entrainment rates would likely be coupled in a practical system. However by allowing for independent specification of the M_i and $\dot{m}_{ent,i}$, this model of the secondary stage enables decoupling of entrainment rate effects from the division of fuel and air between the stages.

In general, the entrainment rates $\dot{m}_{ent,main}(t)$ and $\dot{m}_{ent,sec}(t)$ could vary with time (or

downstream distance). At later times when pure stream i has disappeared, $\dot{m}_{ent,i} = 0$. In this study, the main and secondary entrainment rates are held constant until the respective stream disappears, i.e., until all that fluid has been entrained. While the most direct approach to control entrainment rate is to specify $\dot{m}_{ent,i}$, we instead prescribe entrainment rates through *entrainment time scales* $\tau_{ent,i}$, defined as the total time required for a reservoir of amount M_i to be convected into the entrained region. In physical terms, $\tau_{ent,i}$ represents the spatial distance along which a pure fluid stream i exists in the time-averaged flow field, or equivalently the distance along the flow field where some pure fluid i remains unentrained.

Mathematically, it is defined such that

$$\int_{t=0}^{\tau_{ent,i}} \dot{m}_{ent,i}(t)\, dt = M_i \tag{4.2}$$

In the present case of constant $\dot{m}_{ent,i}$ (e.g., by taking it to be the average entrainment rate in a time-averaged flow field),

$$\dot{m}_{ent,i} \int_{t=0}^{\tau_{ent,i}} dt = M_i \tag{4.3}$$

$$\tau_{ent,i} = \frac{M_i}{\dot{m}_{ent,i}} \tag{4.4}$$

A key motivation behind the use of entrainment time scales is to compare cases that have similar entrainment characteristics although the overall inlet flow rates are different. When modeling a JICF setup for instance, this allows $\tau_{ent,main}$ and $\tau_{ent,sec}$ to be independently specified so that ϕ_{main} and ϕ_{sec} can be varied without affecting the jet's penetration distance into the crossflow. The use of $\tau_{ent,main}$ and $\tau_{ent,sec}$ is illustrated in Fig. 4.2 through the different points in time at which the streams stop entraining into the entrained region.

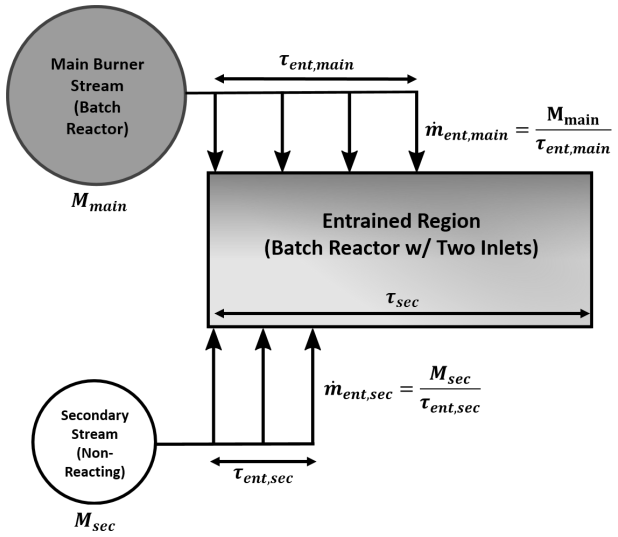

Figure 4.2: Reactor network used to model the secondary stage of a staged combustor under finite-entrainment of main and secondary streams. In this work, the entrained region is assumed to be a region where diffusive mixing is instantaneous. The model for the main burner is the same as the one described in Section 2.2.1 and used in Chapter 3.

4.1.4 Model Parameters

As noted above, the four mass parameters: $M_{fuel,main}$, $M_{air,main}$, $M_{fuel,sec}$ and $M_{air,sec}$ can be more conveniently, and perhaps more meaningfully, specified using the main burner, secondary and overall combustor equivalence ratios, ϕ_{main}, ϕ_{sec}, and ϕ_{global}. Since there are four unknowns, the specification of these three equivalence ratios along with one other variable serves to fully constrain the problem. If the fourth variable is chosen to be M_{total}, one can determine $M_{main} = M_{fuel,main} + M_{air,main}$ and $M_{sec} = M_{fuel,sec} + M_{air,sec}$ according

to the following equations:

$$M_{fuel,main} = M_{total}\left[\frac{\phi_{main} f_s}{\phi_{global} f_s + 1}\frac{\phi_{global} - \phi_{sec}}{\phi_{main} - \phi_{sec}}\right] \tag{4.5a}$$

$$M_{air,main} = M_{total}\left[\frac{1}{\phi_{global} f_s + 1}\frac{\phi_{global} - \phi_{sec}}{\phi_{main} - \phi_{sec}}\right] \tag{4.5b}$$

$$M_{fuel,sec} = M_{total}\left[\frac{\phi_{sec} f_s}{\phi_{sec} f_s + 1}\right]\left[1 - \frac{\left(\phi_{main} f_s + 1\right)\left(\phi_{global} - \phi_{sec}\right)}{\left(\phi_{global} f_s + 1\right)\left(\phi_{main} - \phi_{sec}\right)}\right] \tag{4.5c}$$

$$M_{air,sec} = M_{total}\left[\frac{1}{\phi_{sec} f_s + 1}\right]\left[1 - \frac{\left(\phi_{main} f_s + 1\right)\left(\phi_{global} - \phi_{sec}\right)}{\left(\phi_{global} f_s + 1\right)\left(\phi_{main} - \phi_{sec}\right)}\right] \tag{4.5d}$$

where in order to ensure all mass flow rates are non-negative.

$$\phi_{sec} \geq \frac{\phi_{global} f_s}{\phi_{global} f_s + 1}\left(\phi_{main} f_s + 1\right) \tag{4.6}$$

The variation in M_{main} and M_{sec} across normalized secondary equivalence ratio is shown in Figure 4.3 for a methane-air system with specified main and global equivalence ratios.

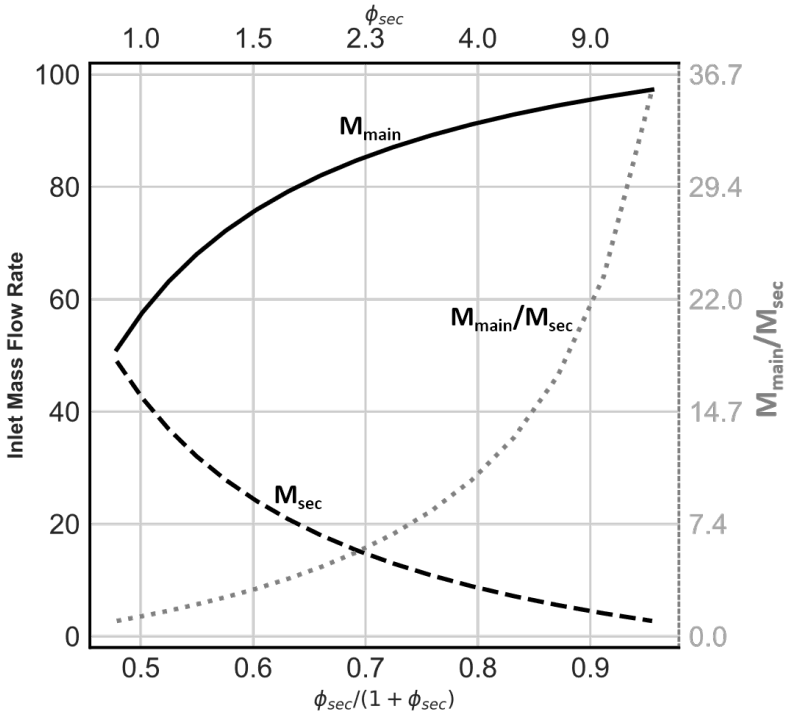

Figure 4.3: Variation in main and secondary inlet mass flow rates with secondary equivalence ratio as governed by Equation 4.5. Results shown for $M_{total} = 100$, $\phi_{main} = 0.37$, $\phi_{global} = 0.64$, $f_s = 0.058$ (CH_4-air).

In addition to the three equivalence ratios and the (arbitrary) total mass, the staged combustor model requires parameters related to the combustor geometry: the main burner residence time τ_{main} (from the flame to the start of the secondary stage) and the secondary stage residence time τ_{sec} (from the start of the secondary stage to the end of the combustor). The full list of model parameters is given in Table 4.1. In addition, the results presented here utilize the GRI-3.0 mechanism to model the methane and NO chemical kinetics.

4.1.5 Design Optimization

This reactor network model can be used to perform both parametric studies and optimization studies, e.g., for preliminary combustor design. This chapter presents an optimization study conducted by wrapping the Dakota framework [77] around the staged combustor model. The objective is to minimize NO emissions for a firing temperature of 1975 K and

Table 4.1: List of parameters required by the finite-entrainment staged combustor model.

Parameter	Description
T_{fuel}	Fuel preheat temperature
T_{air}	Air preheat temperature
P	Pressure
τ_{main}	Main burner residence time
τ_{sec}	Secondary burner residence time
ϕ_{global}	Global equivalence ratio
ϕ_{main}	Main burner equivalence ratio
ϕ_{sec}	Secondary inlet equivalence ratio
M_{total}	Total inlet (main + secondary) flow rate
$\tau_{ent,main}$	Main burner entrainment time scale
$\tau_{ent,sec}$	Secondary burner entrainment time scale

a given set of entrainment time scales, subject to constraints on M_{sec}/M_{total} and CO_{eq}.

We use an asynchronous parallel pattern search solver implemented in the HOPSPACK framework [78] which is bundled into Dakota. Leveraging HOPSPACK's parallel MPI implementation and Dakota's *multilevel parallelism* paradigm, optimization steps involving this otherwise serial model can be performed in an embarrassingly parallel fashion, thus allowing for large parameter spaces to be searched using high-performance computing clusters. The current work employed Georgia Techs PACE cluster [79].

Parametric studies were performed by varying the main burner and secondary stage entrainment time scales, $\tau_{ent,main}$ and $\tau_{ent,sec}$. The ratio of these two parameters, r_τ, is defined in Equation 4.7 and will be an important parameter in the analyses to follow.

$$r_\tau \equiv \frac{\tau_{ent,main}}{\tau_{ent,sec}} \tag{4.7}$$

It is helpful to keep in mind the inverse relationship between the entrainment *time scales* and the entrainment *rates*, as both will be called upon interchangeably in this work; longer entrainment time scales correspond to *lower* entrainment rates and vice versa. Furthermore, substituting Equation 4.4 into Equation 4.7 gives the following expression that relates the

ratio of entrainment time scales to the ratio of entrainment *rates*,

$$r_\tau = \frac{\tau_{ent,main}}{\tau_{ent,sec}} = \frac{M_{main}/\dot{m}_{ent,main}}{M_{sec}/\dot{m}_{ent,sec}} = \frac{M_{main}}{M_{sec}} \frac{\dot{m}_{ent,sec}}{\dot{m}_{ent,main}} \tag{4.8}$$

The parameters shown in Table 4.2 are held constant throughout the current simulations to simulate a relevant engine condition, with one exception. In most of the results, the main burner is operated at the optimum equivalence ratio identified in a previous work — 0.372. This value for ϕ_{main} was identified to be the leanest fuel-air mixture within the flammability limit of a methane-air system that enabled autoignition of the secondary stage. For the optimization study, the main burner equivalence ratio is a free parameter, allowed to vary in order to achieve the minimum NO emissions.

Table 4.2: Parameters held constant in this study.

Parameter	**Value**
T_{final} (K)	1975
ϕ_{global}	0.635
ϕ_{main}	0.372
P (atm)	25
T_{fuel} (K)	300
T_{air} (K)	650

Similar to Section 3.3, emissions values are corrected to 15% O_2 on a volumetric dry basis. Unless stated otherwise, these corrected NO values are reported from the point in a staged combustor when final CO burnout reaches 125% of equilibrium CO. As opposed to reporting NO at a fixed point in time, this approach provides a consistent basis on which to compare different entrainment regimes. [1] The premise behind allowing 25% more CO at the combustor exit is to anticipate further CO burnout beyond the combustor (e.g., in the

[1] For instance, recall from the definition of entrainment time scales in Section 4.1.3 that a larger $\tau_{ent,main}$ means that vitiated main burner products stay pure for longer before being completely entrained. This necessitates longer residence times to allow for CO burnout, which leads to higher NO levels than that of combustors with faster entrainment.

engine turbine or nozzle).

Thus it is important to remember that the total residence time in the combustor ($\tau_{res,main}+\tau_{res,sec}$) is *not* fixed in this chapter, as longer entrainment time scales can require longer residence times to allow for CO burnout and vice versa. For an exit temperature of 1975 K (ϕ_{global} = 0.635), 125% of equilibrium CO (corrected) is roughly 33 ppm. In other words, the following solutions all have the same CO level of 33 ppm.

4.2 Finite Entrainment Effects: Pure Fuel Secondary Stage

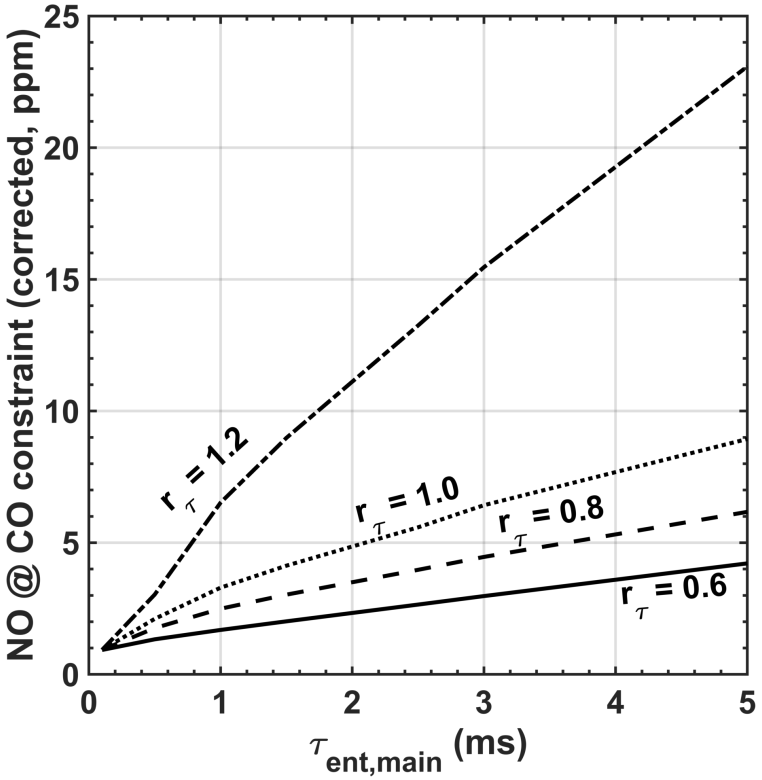

Figure 4.4: Corrected NO at 125% CO_{eq} constraint across different main burner entrainment time scales $\tau_{ent,main}$ and entrainment ratios $r_\tau \equiv \tau_{ent,main}/\tau_{ent,sec}$.

Figure 4.4 shows NO values from the staged combustor model for various entrainment rates of main and secondary fluids. At low $\tau_{ent,main}$, near 0.1 ms, NO emissions approach the minimum levels identified in Section 3.4. This shows that entrainment time scales on the order of 0.1 ms can be considered "infinitely fast". As demonstrated in the previous

chapter, fast entrainment of both streams allows for quicker CO burnout, leading to shorter overall residence times and thus less time for NO production. Indeed, the optimum secondary stage residence time identified in Section 3.4 was around 0.2 ms, which is on the same order of magnitude as the "fast" limit identified in this finite entrainment scenario.

For a given ratio of main-to-secondary entrainment time scales r_τ, $\tau_{ent,sec}$ increases with $\tau_{ent,main}$, thus increasing the total residence time of the secondary stage. Consequently, NO increases monotonically with $\tau_{ent,main}$ as a result of the linear dependence of thermal NO on residence time. The *degree* of dependence, however, is a function of r_τ. Cases with $r_\tau \leq 1$ maintain relatively low levels of NO (below 10 ppm) even at high $\tau_{ent,main}$, while cases with r_τ approaching unity and beyond strongly depend on $\tau_{ent,main}$ (and thus residence time) and exhibit higher NO levels. NO increases monotonically with r_τ between 0.6 and 1.2. NO sensitivity to r_τ also increases with $\tau_{ent,main}$; at $\tau_{ent,main} = 1$ ms, doubling r_τ from 0.6 to 1.2 increases NO by 5 ppm (roughly 4×), whereas at $\tau_{ent,main} = 5$ ms, doubling r_τ increases NO by 21 ppm (roughly 6×). This increase in sensitivity is more clearly illustrated in Figure 4.5, which shows increasing NO–r_τ gradients between the different $\tau_{ent,main}$ cases.

Time traces of temperature and NO in the secondary stage are presented in Figure 4.6 to aid in understanding the foregoing observations — namely that NO increases monotonically with $\tau_{ent,main}$ and r_τ, and that NO sensitivity to entrainment ratio (dNO/dr_τ) increases with $\tau_{ent,main}$. The temperature is that of the *entrained region*, while the corrected NO mole fractions are averaged over the complete system, that is to say, the average NO taking into account fluid both inside and outside the entrained region.

In the $r_\tau = 0.6$ case (solid lines), vitiated products from the main burner finish entraining earlier than the secondary fuel. The entrained region burns at a constant ϕ ($< \phi_{global}$) while both streams are entraining and burns at increasingly higher ϕ (eventually reaching ϕ_{global}) with continued secondary fuel entrainment after the completion of main burner entrainment at 5 ms. Once all the reactants are completely entrained, the burned gas tem-

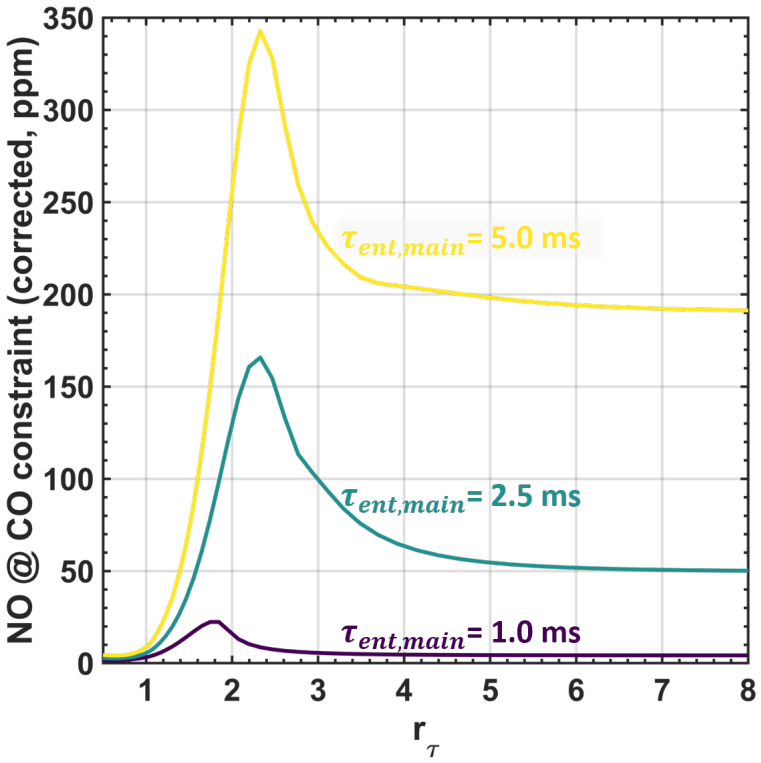

Figure 4.5: Variation of corrected NO (at 125% CO_{eq} constraint) with entrainment ratio r_τ varying from 0.6 to 8.0 across main burner entrainment time scales $\tau_{ent,main}$ = 1.0 ms, 2.0 ms and 5.0 ms.

perature reaches the target 1975 K value ($\phi_{global} \approx 0.635$).

At this point, it is helpful to recall Equation 4.8 and note that an increase in r_τ under constant M_{main}/M_{sec} results in a higher secondary-to-main entrainment rate ratio, $\dot{m}_{ent,sec}/\dot{m}_{ent,main}$. The dashed temperature trace in Figure 4.6 shows that when $r_\tau = 1.0$, $\dot{m}_{ent,sec}/\dot{m}_{ent,main}$ is equal to M_{sec}/M_{main}, which corresponds to the fuel-air ratio prescribed by ϕ_{global} and ϕ_{main} as given by Equation 4.5. The entrained region thus burns at the final temperature and the corresponding NO production rate until there is complete entrainment of both reactant streams and sufficient oxidation of CO. This results in higher overall NO production than the $r_\tau = 0.6$ case, which only attains 1975 K (and the corresponding NO production rate) toward the end of the entrained region. The $r_\tau = 1.0$ case and the infinite mixing and entrainment time traces shown in Figure 3.3a exhibit an interesting similarity—both models burn at the target equivalence ratio throughout the secondary

stage, with the main difference being the increased residence time for the finite entrainment rate case.

As seen in Figure 4.4, the $r_\tau = 1.2$ case exhibits the highest NO level. This is most clearly understood through the evolution of the local temperature in the entrained region. Here, secondary fuel entrains faster than vitiated main burner products and consequently finishes entraining *earlier* than the main burner fluid stream. As such, the entrained region burns at a higher ϕ compared to when $r_\tau = 0.6$ and 1.0, reaching local temperatures beyond the final temperature. This temperature overshoot results in significantly higher NO production rates as evidenced by the NO traces shown in Figure 4.6, where the $r_\tau = 1.2$ case has the steepest NO slope among all three cases. The higher temperature also leads to the increased sensitivity of NO to $\tau_{ent,main}$ observed in Figure 4.4.

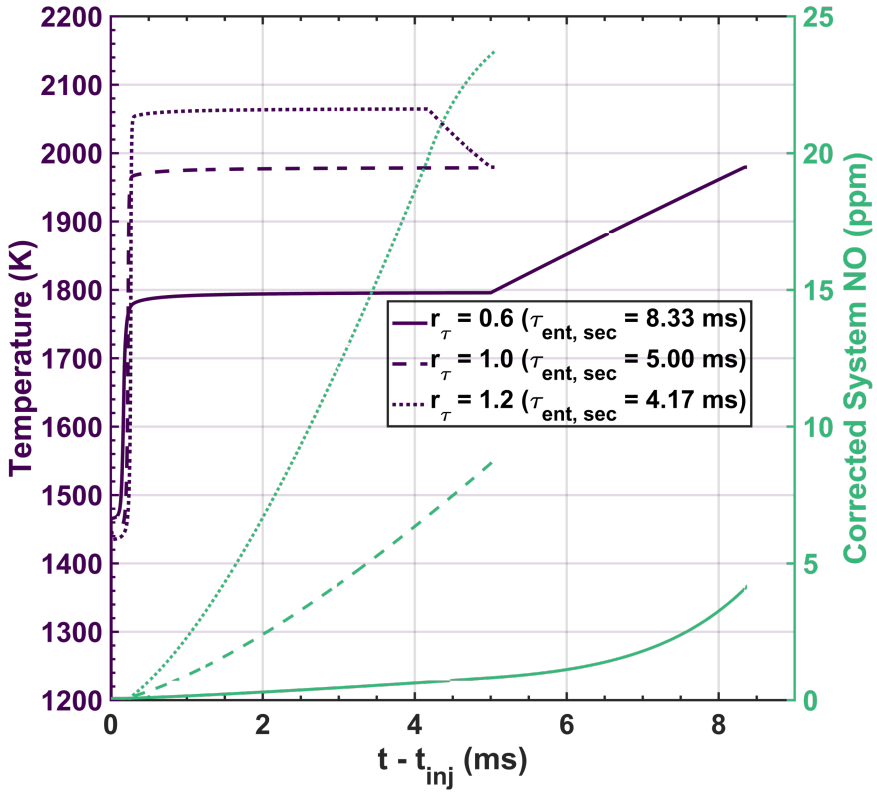

Figure 4.6: Time evolution of entrained region temperature and system averaged NO for $\tau_{ent,main} = 5$ ms and $r_\tau = 0.6$, 1.0 and 1.2. System averaged NO accounts for unentrained reactants when calculating the corrected value. For r_τ = 0.6 and 1.0, the time evolution of the system is shown until system average CO reaches the 125% CO_{eq} constraint.

To reiterate, these results show that even for finite-rate entrainment in the secondary stage, NO emission levels can be reasonably low, e.g., below 10 ppm, as long as the main burner product entrainment is not too slow (e.g., $\tau_{ent,main}$ below 5 ms) and the entrainment ratio is less than 1-1.2. While this is above the NO value ($\sim$1 ppm) predicted for infinite entrainment rates, it is well below the minimum NO of an ideal LPM combustor with a 20 ms residence time under similar operating conditions, i.e., 25 ppm. However, completely entraining the main product stream more quickly than the much lower mass flow rate fuel stream would be difficult. In practice, this would require initial placement of the fuel in close contact with nearly all the main stream, or intense stirring of the two streams. Given the high temperature of the product stream, distributing fuel injectors throughout the hot flow would be problematic. Furthermore, typical staged combustor configurations, for example those employing conventional transverse jets in crossflow do not provide sufficient penetration of the injected fuel into the main burner exhaust, leaving a significant portion of the latter unentrained for long times. Due to the excess main burner products that remain pure, ignition and NO formation reactions occur in a mixture much richer than the global stoichiometry. In other words, r_τ in such conventional configurations is typically greater than unity and represents situations where the secondary mixture ignites before all the crossflow fluid has entrained with the jet fluid.

Figure 4.5 includes results for cases where $r_\tau > 1$. For $\tau_{ent,main}$ slower than a few ms, NO levels are near 100 ppm or more — significantly beyond that of current emissions regulations. Compared to the cases where $r_\tau \leq 1$, NO levels in these cases exhibit a higher dependence on $\tau_{ent,main}$, which limits the secondary stage residence time. For the range of $\tau_{ent,main}$ tested, a region of high NO exists around $1.8 \leq r_\tau \leq 2.3$ as shown by the peaks in Figure 4.5. In this region, slight variations in r_τ can significantly change the amount of NO produced, as do slight perturbations in $\tau_{ent,main}$. In other words, the entrainment rates of *both* main and secondary streams are very crucial to NO production when the secondary stream entrains roughly twice as fast as the main burner. Beyond the peaks around $r_\tau \approx 2.3$,

NO decreases monotonically with r_τ and achieves lower levels (albeit still above regulatory limits), and are less sensitive to increases in r_τ.

Of particular interest is the ability of the $\tau_{ent,main} = 1.0$ ms case to maintain NO levels below 30 ppm across the entire range of r_τ, indicating that so long as the main burner is fully entrained in approximately 1.0 ms, a designer can allow the secondary fuel stream to entrain faster or slower than the main burner stream. This is another result of the linear dependence of NO on residence time — if the overall residence time is capped at 1 ms, NO levels will be relatively low regardless of the rate at which the secondary fuel entrains.

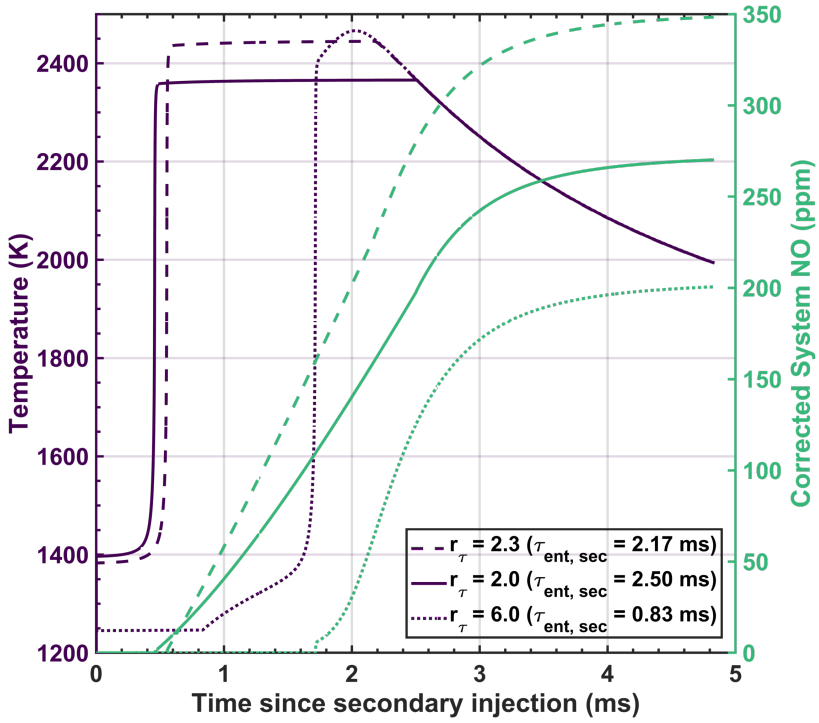

Figure 4.7: Time evolution of entrained region temperature and system averaged NO for $\tau_{ent,main} = 5$ ms and $r_\tau = 2.0$, 2.3, and 6.0. System averaged NO accounts for unentrained reactants when calculating the corrected value. The time evolution of the system is shown until system average CO reaches the 125% CO_{eq} constraint.

As previously noted, the $r_\tau = 1.2$ case produces a temperature overshoot because the entrained region begins burning when its equivalence ratio is *above* ϕ_{global}. As r_τ increases further, the entrained region burns at increasingly higher equivalence ratios, leading to a significantly larger overshoot temperature that drives the sharp rise in NO when r_τ in-

creases from 1.2 to around 2.3. This trend is shown in Figure 4.7, where the overshoot temperature increases monotonically with r_τ and peaks near the stoichiometric adiabatic flame temperature ($\sim$2460 K for a methane-air system with the initial conditions used in this study). In fact, due to the fast secondary entrainment rate when $r_\tau = 6.0$, the entrained region actually ignites rich and passes through $\phi = 1$ before eventually reaching ϕ_{global}.

However, it should be observed that NO production is not governed by overshoot temperature alone. Indeed, the case with the highest overshoot temperature ($r_\tau = 6.0$) does not result in the highest NO emissions as one might expect; rather, this occurs at the $r_\tau = 2.3$ case, which has a longer dwell time at a slightly lower peak temperature. The significant difference in time spent at the overshoot temperature can be attributed to the shorter ignition delay after entrainment begins for the $r_\tau = 2.3$ case (0.5 ms) compared to the $r_\tau = 6.0$ case (1.6 ms). This difference in ignition delay is in turn driven by the difference in initial temperature of the entrained region, which depends on the temperatures and entrainment rates of both streams. For example, increasing the entrainment rate of secondary fuel (which is colder than the main burner products) leads to a lower initial temperature and thus increases ignition delay. Likewise, lowering the temperature of the secondary fuel stream while maintaining constant entrainment rates also increases ignition delay.

Recall that thermal NO production in high-temperature combustion environments depends on temperature and residence time. In an axial fuel-staged combustor with finite entrainment rates, these two parameters manifest themselves as the maximum temperature in the combustor and the time spent at those temperatures. We have seen that cases with $T_{max} \leq T_{final}$ produce the lowest NO levels — these cases burn at equivalence ratios below ϕ_{global} and eventually "work" their way up to the final equivalence ratio, thereby reducing time spent at the maximum temperature. For cases where $T_{max} > T_{final}$, time spent at the maximum temperature can be reduced primarily by entraining the main burner stream faster and to a lesser extent by delaying autoignition.

4.3 Finite Entrainment Effects: Fuel-Air Secondary Stage

The results of the preceding section demonstrate that NO_x emissions from an axial fuel-staged system with finite-entrainment rates will have difficulty achieving NO emissions well below those of a single-stage LPM combustor unless the fuel can be entrained with enough main burner products before ignition occurs such that near stoichiometric conditions are avoided. Achieving this in a practical implementation is likely prohibitive. Furthermore, the NO exhaust levels can be quite sensitive to the relative entrainment rates of the fuel and main burner streams, so a system designed to achieve low NO emissions would produce much higher emissions for even moderately small changes in the entrainment conditions.

This section explores how staging both fuel and air can relax the entrainment requirements. The effect of a variable secondary injection equivalence ratio ϕ_{sec} on NO is elucidated by examining the governing physical parameters affected by ϕ_{sec} — namely entrained region temperature and residence time. In addition, the sensitivities of NO to entrainment rates and secondary equivalence ratios are also characterized to provide readers with a sense of the design landscape.

4.3.1 Varying ϕ_{sec} Under Constant r_τ

We first consider variations in ϕ_{sec} while ϕ_{global} and ϕ_{main} are held constant. We specify these three equivalence ratios and the total mass flow rate (M_{total}) to determine the flow rates of fuel and air at the main and secondary inlets — $M_{fuel,main}$, $M_{air,main}$, $M_{fuel,sec}$, $M_{air,sec}$, given by Equation 4.5. In this parametric study, we present results using both the standard and normalized (symmetric) versions of the equivalence ratio. The latter, $\phi_{sec,norm}$ (Equation 4.9), ranges from 0.48 to 0.96, which corresponds to a ϕ_{sec} range of 0.92 to 21.2.

$$\phi_{sec,\ norm} = \frac{\phi_{sec}}{1 + \phi_{sec}} \tag{4.9}$$

The highest ϕ_{sec} examined can be considered to reasonably represent the limiting pure fuel case, whereas the lowest value represents the minimum ϕ_{sec} for which the secondary mixture is able to reach T_{final} within 15 ms. The values of ϕ_{sec} and $\phi_{sec,norm}$ studied are illustrated in Figure 4.8; they are uniformly distributed in the normalized space, but more concentrated toward less rich mixtures in standard ϕ. ϕ_{main} and ϕ_{global} are held constant at the same values that were used in the pure fuel-staging study in order to isolate the effect of secondary equivalence ratio on NO production.

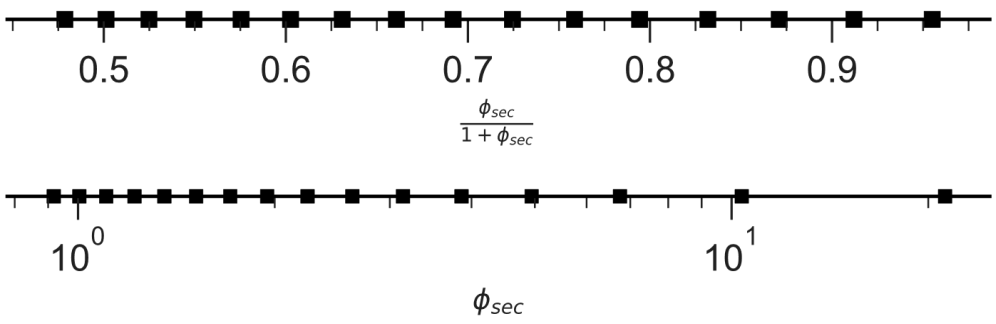

Figure 4.8: Distribution of secondary equivalence ratio used in the present study.

The effect of incorporating air-staging on the NO-r_τ relationship is presented in Figure 4.9 for the same three $\tau_{ent,main}$ values used in the pure fuel study. As expected, the results for the richest secondary case, ϕ_{sec} of 21.2, are essentially the same as the pure fuel results presented in Figure 4.5. In addition, the non-monotonic dependence of NO on r_τ, i.e., the NO peak, is retained across the complete range of ϕ_{sec} examined, with the peaks for corresponding $\tau_{ent,main}$ cases migrating to lower r_τ values as ϕ_{sec} is decreased. Perhaps the most striking observation is that NO emissions below 10 ppm can be achieved across the full range of r_τ values if the secondary stage injection is close to stoichiometric, though it can remain somewhat rich, e.g., 1.5. It should be noted, however, that producing ϕ_{sec}

between 1 and 1.5 requires injection of $\sim$ 25-45% of the overall flow in the secondary stage for the chosen ϕ_{global} and ϕ_{main} (see Figure 4.3).

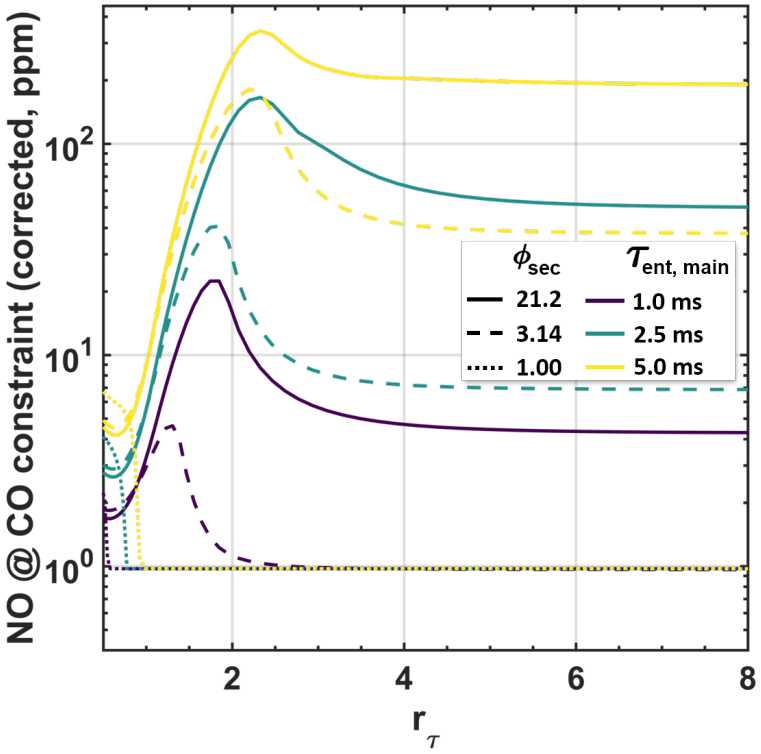

Figure 4.9: Corrected NO at 125% CO_{eq} constraint across entrainment ratio r_τ for various ϕ_{sec} and $\tau_{ent,main}$ combinations.

When secondary entrainment completes before the main stream entrainment, (r_τ > 1), we observe a decrease in NO for fixed r_τ as air is shifted to the secondary stage; for $r_\tau <$ 1, the opposite trend occurs. The remainder of this section explores these behaviors, beginning with slower main entrainment.

Figure 4.10 presents the same NO results as Figure 4.9, but now as a function of secondary stream equivalence ratio at $r_\tau = 2.2$ and 7.8. Clearly, NO increases monotonically with ϕ_{sec}, with a pure fuel secondary stream producing the highest NO. The reduction in NO with decreasing ϕ_{sec} can be attributed to the previously identified parameters, specifically lower peak temperatures and shorter high-temperature dwell times resulting from longer ignition delay, τ_{ign}. Indeed, the maximum local (entrained region) temperature for each case, shown in Figure 4.11, is generally a good indicator of the relative amount of

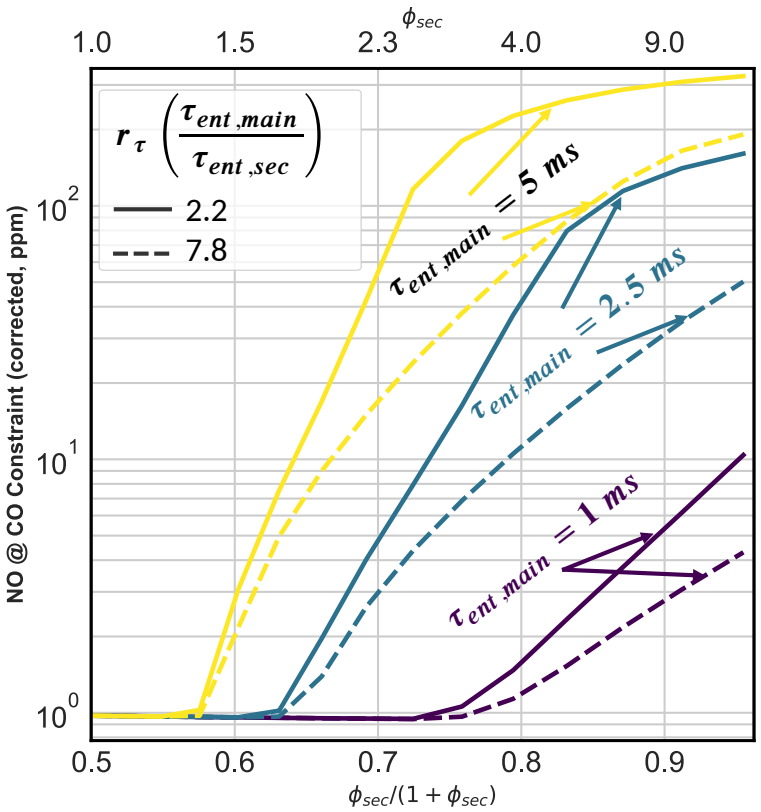

Figure 4.10: Corrected NO at 125% CO_{eq} constraint across different secondary equivalence ratios ϕ_{sec} for different main burner entrainment time scales $\tau_{ent,main}$ and entrainment ratios r_τ.

NO produced. For a fixed main entrainment time, the higher r_τ case (i.e., where secondary entrainment finishes earlier) produces less NO and generally has a lower maximum temperature. The exception is for long entrainment times and relatively rich mixtures, e.g., $\tau_{ent,main} = 5$ ms and $\phi_{sec,norm} > 0.85$, where the faster secondary entrainment ($r_\tau = 7.8$) case still produces less NO but now has a higher maximum temperature than the $r_\tau = 2.2$ case.

As in the pure fuel results, entraining the secondary fluid more quickly for a fixed main entrainment time results in lower initial temperatures within the entrained region. Consequently, increasing r_τ generally tends to significantly lengthen the ignition delay, resulting in a lower equivalence ratio in the entrained region when it ignites compared to the lower r_τ case. This effect is magnified with the addition of air to the secondary

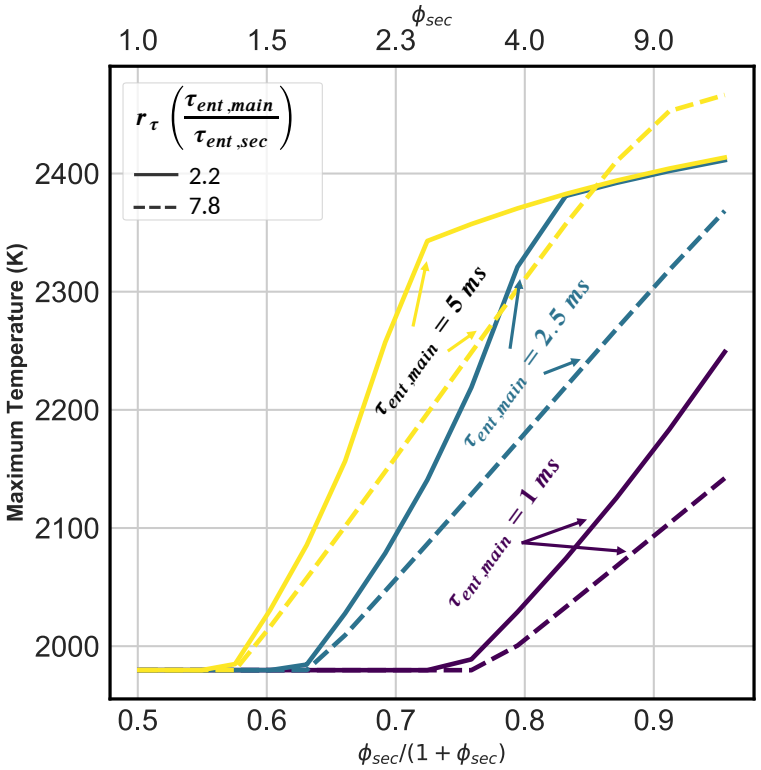

Figure 4.11: Maximum local temperature achieved in the entrained region across different secondary equivalence ratios ϕ_{sec} for different main burner entrainment time scales $\tau_{ent,main}$ and entrainment ratios r_τ.

stream — while decreasing ϕ_{sec} increases the temperature of the secondary stream, which is formed from cold (300 K) fuel but preheated (650 K) air, it also adds mass to the secondary stream under our constraint of fixed ϕ_{main}. Moreover, almost all of the cases presented in Figure 4.11 produce maximum temperatures well below the stoichiometric adiabatic flame temperature of 2460 K. Thus, increasing the fraction of air in the secondary stream (i.e., reducing ϕ_{sec}) further delays ignition such that the entrained region ignites only when its local equivalence ratio is lean.

For $\tau_{ent,main} = 5$ ms, $\phi_{sec,norm} > 0.85$ and r_τ = 7.8, the amount of air added to the secondary stream is small, so the entrained region ignites closer to stoichiometric in the r_τ = 7.8 case compared to the r_τ = 2.2 case, which leads to higher local temperatures in the former. However, as illustrated by the time traces in Figure 4.12, τ_{ign} is considerably shorter for the $r_\tau = 2.2$ case — the high-$\phi_{sec,norm}$ cases ignite in less than 1 ms, well be-

fore secondary entrainment is complete (2.3 ms). Therefore, although the entrained region ignites closer to stoichiometric in the r_τ = 7.8 case, the reduced high-temperature dwell time due to longer τ_{ign} results in lower NO production.

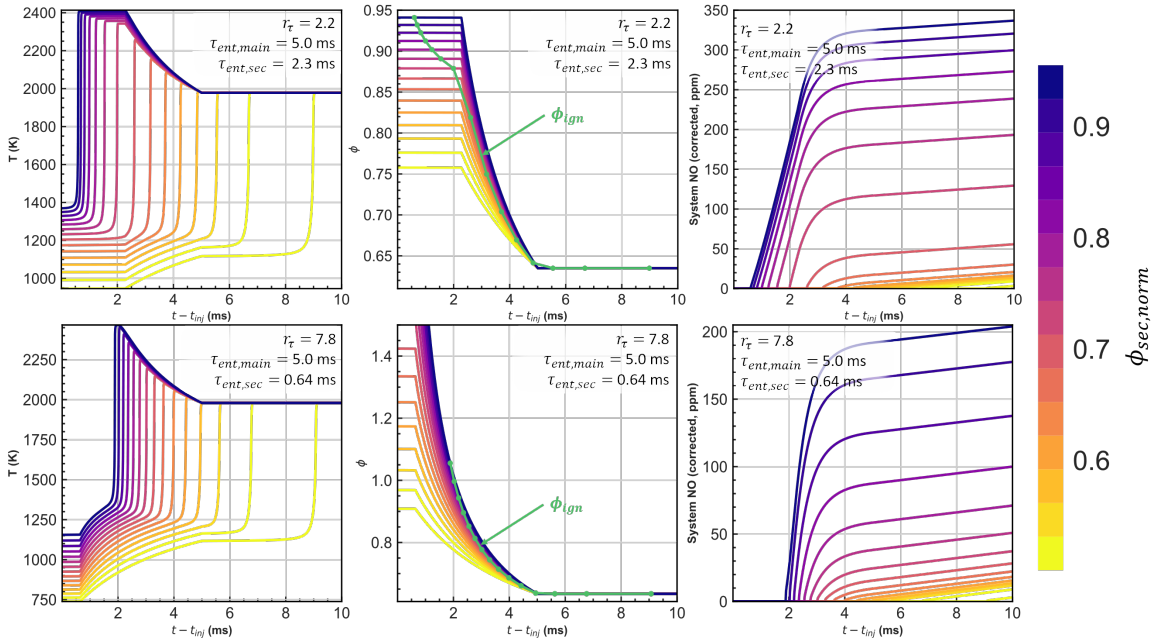

Figure 4.12: Time traces of entrained region temperature, entrained region equivalence ratio and corrected system NO for various ϕ_{sec} at $\tau_{ent,main}$ = 5 ms and r_τ = 2.2 and 7.8.

Returning to the NO results shown in Figure 4.10, we can identify three distinct regions as ϕ_{sec} changes. In the first region, where the secondary stream is only moderately rich, NO emissions stay roughly constant, near the theoretical minimum value for fast entrainment (< 1 ppm), and are essentially independent of $\tau_{ent,sec}$ for $r_\tau > 1$. These are cases with ignition delay times (τ_{ign}) longer than the entrainment time scales, such that the entrained region burns only after nearly all the main and secondary fluids have been entrained. In other words, low-ϕ_{sec} cases that only burn when $\phi_{entrain} = \phi_{global}$ do not experience temperature overshoots and exhibit NO levels equivalent to that of the infinite entrainment case. Moreover, the range of ϕ_{sec} for which this holds decreases as the main entrainment time drops. In this region, we can say that NO emissions are low because entrainment is sufficiently fast to *increase* the relevant chemical time scale (τ_{ign}) beyond the slowest entrainment time.

The second region exhibits a high slope, $d\text{log(NO)}/d\phi_{sec,norm}$, occupying ϕ_{sec} ranges where τ_{ign} is longer than the smaller of the two entrainment time scales, i.e., where the entrained region ignites after the secondary stream has fully entrained but while the main stream is still entraining. In this region, increases in τ_{ign} afforded by lower ϕ_{sec} allows more main burner fluid to be entrained before ignition, which leads to lower ϕ_{ign} and T_{max} because more (lean) main burner products are being mixed with (all) the secondary fluid, thus creating a leaner mixture at ignition.

Finally the third region exhibits a reduced $d\text{log(NO)}/d\phi_{sec,norm}$ and occupies the upper ϕ_{sec} range. For the conditions of Figure 4.10, this region only exists for the slower entrainment cases, e.g., $\tau_{ent,main} =$ 2.5 and 5 ms, and r_τ = 2.2 (the 5 ms case is the one discussed previously). Here, large temperature overshoots (above T_{final}) persist for long periods of time, as seen in Figure 4.12 as well as the previous pure fuel results. Ignition occurs while the secondary fluid is still entraining. In other words, the chemical time in this region is faster than the entrainment time scales.

Next, we consider the sensitivity of the NO produced to changes in entrainment times (since entrainment rates will have significant fluctuations and variations in a practical system). The results shown in Figure 4.10 reveal that $d\text{NO}/d\tau_{ent}$ is reasonably small for ϕ_{sec} below roughly 1.5-2. For example, varying $\tau_{ent,main}$ from 2.5 to 5 ms and r_τ from 2.2 to 7.8 at $\phi_{sec} = 1.7$ results in NO ranging from approximately 1-8 ppm.

At this point, we return to the unusual behavior observed for $r_\tau < 1$ in Figure 4.9, i.e., an increase in NO as more air is diverted to the secondary stage. Under these conditions, the entrained region is lean initially since the main burner stream entrains more quickly than the secondary stream. According to Eq. 4.8, increasing $\phi_{sec,norm}$ leads to a larger entrainment rate of secondary fluid $\dot{m}_{ent,sec}$ relative to main burner fluid (to maintain the same r_τ). Because the system is limited by the slower secondary stream entrainment rate when $r_\tau < 1$, an increase in $\dot{m}_{ent,sec}$ results in a higher initial equivalence ratio and consequently a higher ϕ_{ign} (closer to ϕ_{global}). This is illustrated in the equivalence ratio time traces shown

in Figure 4.13, where lower ϕ_{sec} in fact results in *higher* ϕ_{ign} [2]. Thus the low ϕ_{sec} cases that ignite at higher equivalence ratios burn hotter than the high ϕ_{sec} cases, leading to higher NO production rate. The temperature traces in Figure 4.13 show that for $r_\tau < 1$, the reduction in "high-temperature" dwell time from the longer τ_{ign} exerts a smaller influence on NO compared to the increase in temperature because the thermal NO pathway is temperature-limited at these low-temperature (< 1800 K) initial conditions. Regardless, the NO levels for $r_\tau < 1$ are relatively low (< 10 ppm) for all the cases examined, and while conceptually interesting, this region is less likely to be observed for the same reasons outlined in Section 4.2.

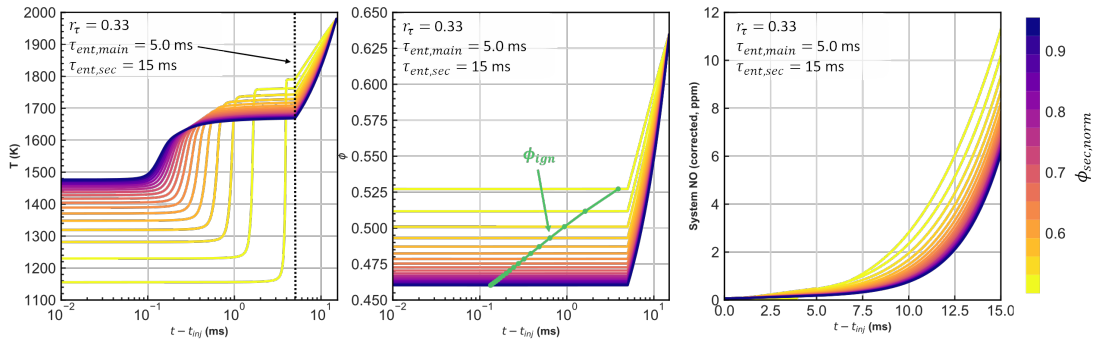

Figure 4.13: Time traces of entrained region temperature, entrained region equivalence ratio and corrected system NO for various ϕ_{sec} at $\tau_{ent,main}$ = 5 ms and r_τ = 0.33. The horizontal time axis is plotted on a logarithmic scale to magnify pre-ignition features in the temperature and equivalence ratio plots. The ignition equivalence ratio of the entrained region, ϕ_{ign}, is indicated with round markers on top of the equivalence ratio subplot.

4.3.2 Varying ϕ_{sec} Under Constant Entrainment Rates

In the previous analysis, results were presented for fixed r_τ. For this to occur, however, Eq. 4.8 indicates that the mass entrainment ratio $\dot{m}_{ent,sec}/\dot{m}_{ent,main}$ must also increase as a result of adding air to the secondary stage, i.e., lowering M_{main}/M_{sec}. While increasing the mass injected in the secondary stream would likely increase the mass entrainment rates in many practical injection configurations, there is no reason to believe that the changes would

[2] Note that for the $r_\tau \geq 1$ cases shown in Figure 4.12, ϕ_{ign} increases with ϕ_{sec}.

necessarily scale as required above. For example in a typical single JICF configuration, increasing the jet mass flow rate would tend to increase somewhat the time required to entrain all the jet fluid. Thus the previous analysis may be considered to be optimistic regarding the dependence of the entrainment times on ϕ_{sec}.

A more conservative assumption would be that the ratio of the mass entrainment rates is constant as we lower ϕ_{sec}, thus requiring r_τ to decrease. The constant r_τ results can be resampled to create a data set where the mass entrainment ratio is held constant for a fixed main stream entrainment time of 5 ms. These results are presented in Figure 4.14 for three mass entrainment ratios: 0.2, 0.5, and 2.0.

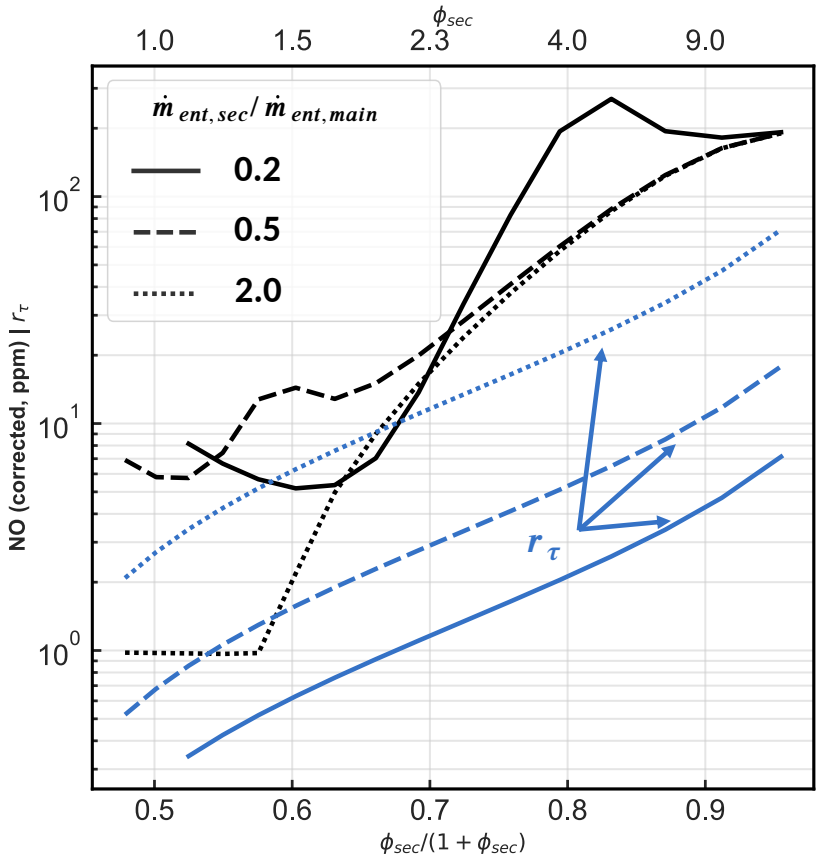

Figure 4.14: Variation of NO with $\phi_{sec,norm}$ for three constant values of entrainment rate ratios. The variation of r_τ with $\phi_{sec,norm}$ for the three entrainment rate ratios (as governed by Equation 4.8) are shown in blue.

The overall trend is a reduction in NO as the secondary fuel is diluted with air for all three mass entrainment ratios. Once again, reducing ϕ_{sec} tends to lower the peak temper-

ature of the entrained region and reduce the high-temperature residence time by delaying ignition of the secondary mixture. A lower ϕ_{sec} can also reduce NO by enabling the secondary stream to stay pure for longer periods (recall that low r_τ allows the mixture to burn at leaner equivalence ratios before increasing to the final temperature as more secondary fuel is entrained). On the other hand, these results also show that insufficiently decreasing ϕ_{sec} for the lowest mass entrainment ratio leads to NO levels that are actually higher than when injecting pure fuel. This occurs because the lowest mass entrainment ratio (0.2) data set has a lower r_τ than the other cases at a fixed ϕ_{sec}. Thus when a small amount of air is added to the secondary stream r_τ drops to 2-3, which is the maximum NO condition in Figure 4.9. As ϕ_{sec} is reduced further, NO drops as r_τ decreases to 1 and then increases slightly below r_τ = 1. This behavior, though less pronounced, is also seen in the 0.5 mass entrainment ratio case, but not the 2.0 case because it approaches r_τ = 2 only as the secondary stream becomes stoichiometric, where there is little sensitivity to r_τ.

Comparing these fixed mass entrainment ratio results to those for fixed entrainment time ratio (Figures 4.9 and 4.10), we see the minimum obtainable NO levels for near stoichiometric secondary injection are indeed higher, though not by much, with this more conservative entrainment assumption. The minimum NO varies from 1-6 ppm for the cases studied, and the optimum ϕ_{sec} ranges from 1.1 to 1.6.

4.3.3 Connection with Experimental Findings

The results presented thus far demonstrate that for practical finite-rate entrainment cases where $r_\tau > 1$, a leaner secondary injection leads to lower NO. These findings are in agreement with experimental and computational findings by Sirignano [80] and Ahrens et al. [38] on NO_x emissions in typical JICF-based staged combustion systems. They found that decreasing secondary equivalence ratios led to lower NO_x levels, which was attributed to enhanced pre-flame mixing enabled by flame liftoff. Recognizing the non-linear impact of lifting on NO_x, Sirignano characterizes these ϕ_{sec} effects based on liftoff, classifying the

secondary flame behavior into three regimes — lee-stabilized (i.e., attached flame), lean lifted and rich lifted. These regimes are illustrated in Figure 4.15 (compiled from [80]).

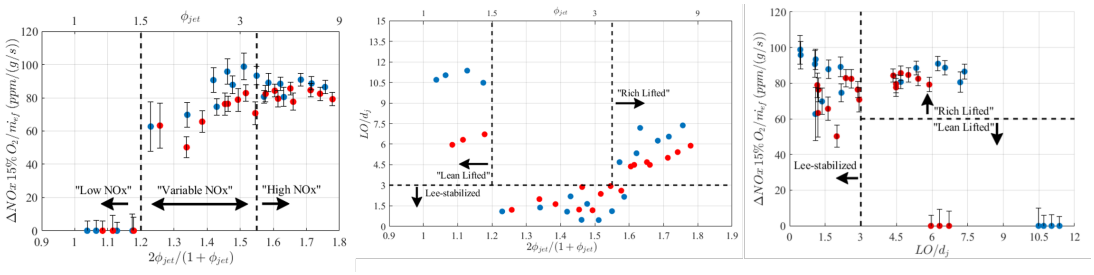

Figure 4.15: Experimental results of normalized NO_x levels and liftoff height as a function of normalized jet equivalence ratio, as well as normalized NO_x levels as a function of liftoff height. Red markers indicate results obtained at $\phi_{main} = 0.50$ and blue markers indicate results obtained at $\phi_{main} = 0.45$. Crossflow conditions were held constant and $J \leq 20$ for all cases [80].

Comparing the first plot in Figure 4.15 to the NO results presented in Figure 4.10, we see that the regions labeled as "Low NO_x", "Variable NO_x" and "High NO_x" are indeed aligned between the modeling results and experimental results, with roughly the same ϕ_{sec} range covered. Moreover, the agreement is quite remarkable for the $\tau_{ent,main} = 5$ ms, $r_\tau = 2.2$ case, which clearly exhibits three distinct regions.

From the three regions of distinct ϕ_{sec} sensitivity identified in Figure 4.10, it can be observed that the low ϕ_{sec} region is similar to the lean lifted cases identified by Sirignano. Both the previous experimental and current numerical results show that this region enables very low NO_x emissions that are essentially constant with ϕ_{sec}. The low experimental NO_x measurements in [80] suggest that ϕ_{ign} is lean due to larger observed liftoff heights, which increase the amount of available time (or equivalently, space) for the jet and crossflow to mix. This hypothesis is supported by the temperature and equivalence ratio time traces shown in Figure 4.12, which indicate that the lean lifted cases at low ϕ_{sec} only ignite when $\phi_{ign} = \phi_{global}$ due to the additional time for entrainment. In other words, the lean lifted case is a scenario where $\max(\tau_{ent,main}, \tau_{ent,sec}) \leq \tau_{ign}$.

The intermediate region of high $d\text{NO}/d\phi_{sec}$ is similar to Sirignano's lee-stabilized regime at intermediate ϕ_{sec} values, which produces moderate levels of NO_x that increase

monotonically with ϕ_{sec}. In the experiments, this region is characterized by a secondary flame that is lifted on the windward side and attached on the lee side, and NO_x levels that vary across a wide range depending on ϕ_{sec}. Experimental results indicate that the change in $d\text{NO}/d\phi_{sec}$ from the lean lifted to the lee-stabilized regime lies in the distinct flame stabilization behaviors, as shown in the middle chart in Figure 4.15. The time traces in Figure 4.12 further illustrate that $d\text{NO}/d\phi_{sec}$ is high because changes in ϕ_{sec} directly impact ϕ_{ign}, which in turn impacts the overshoot temperature. In terms of time scales, this region can be characterized as $\min(\tau_{ent,main}, \tau_{ent,sec}) < \tau_{ign} < \max(\tau_{ent,main}, \tau_{ent,sec})$ where the secondary mixture ignites before the slower of the two streams has completely entrained, which in the case of $r_\tau > 1$ allows for some main burner fluid entrainment before igniting at $\phi_{ign} > \phi_{global}$. Ignition delay is also less sensitive to ϕ_{sec} in this region compared to the lean lifted case due to the higher initial temperatures.

Finally, the region of high NO_x and low ϕ_{sec} sensitivity at high ϕ_{sec} approaching pure fuel staging can be compared to the the "rich lifted" regime in [80]. Both these high-ϕ_{sec} regions produce high levels of NO_x and are relatively insensitive to further increases in ϕ_{sec}. In the experiments, the secondary flame was observed to be fully lifted. However, in the present autoignition-based, flameless model, increasing ϕ_{sec} leads to a very short τ_{ign} as explained in Section 4.3. That is, $\tau_{ign} \ll \min(\tau_{ent,main}, \tau_{ent,sec})$. The short ignition times under fast secondary entrainment (i.e., $r_\tau > 1$) lead to high NO_x levels due to the high temperature overshoots that persist for long periods.

At this point, it should be noted that while the comparisons made between the three regions identified in this work with Sirignano's three regimes corroborate in terms of liftoff height/ignition delay as well as NO_x levels, the classifications based on $\phi_{sec,norm}$ are different. Sirignano observed that secondary flames within the intermediate range of $\phi_{sec,norm}$ between 0.6 and 0.75 are lifted on the windward side and attached on the lee-side of the jet. However, the reactor model predicts that the intermediate $\phi_{sec,norm}$ in between 0.6 and 0.8 actually exhibit significant levels of ignition delay (see Figure 4.12 in Section 4.3 and

Figure A.2 in Appendix A.1). On the other hand, the high ϕ_{sec} cases in the experimental results were classified as rich lifted whereas the modeling results showed very short ignition delay for cases approaching the limit of pure fuel secondary injection.

The key discrepancy lies in the prediction of ignition delay — the reactor model predicts that a higher ϕ_{sec} approaching pure fuel results in lower τ_{ign} because of the higher initial temperature in the entrained region, while the experimental results show that liftoff height increase with ϕ_{sec}. The discrepancy in ignition delay may in turn be caused by differences in the specified parameters between the experimental and computational work. For example, in changing the secondary equivalence ratio ϕ_{sec}, the present simulations hold T_{exit} fixed while allowing M_{main} and M_{sec} to vary as described in Section 4.1, whereas the experimental work holds the relative contributions roughly constant ($\dot{m}_{jet}/\dot{m}_{total} \leq 5\%$ across all experiments) while allowing the exit temperature to vary[3]. Namely, the finite-rate entrainment model reduces M_{sec} as $\phi_{sec,norm}$ is increased towards pure fuel. For a given jet diameter, this reduction in M_{sec} [4] can be linked to a reduction in the jet density and/or jet velocity. The lower jet velocity results in a lower J, thus reducing liftoff height as seen in the experimental study by Kolb *et al.* in [1]. Indeed, the τ_{ign}-ϕ_{sec} trends predicted by the present model are in agreement with experimental observations of liftoff height with jet equivalence ratio by Kolb *et al.* The variation of τ_{ign} with ϕ_{sec} is included in Figure A.2 in Appendix A.1. Under the context of autoignition, the temperature time traces shown in Figure 4.12 illustrate that the main reason for the decrease in liftoff height is the higher initial temperatures due to the lower secondary contribution to total mass.

In summary, this comparison shows that although it is not designed to simulate a jet-in-crossflow, the current finite-rate entrainment model is capable of predicting trends based on entrainment characteristics and physical parameters that are in agreement with experimental findings, so long as the prevailing jet ignition mechanism can be reasonably determined

[3]The normalization of the NO_x results shown in Figure 4.15 are to account for the difference in exit temperatures or "ΔT" imparted by the secondary stage.

[4]Recall that because the finite-rate entrainment model is a closed system, the inlet mass flow rates are represented as *amounts*.

to be driven by autoignition. It is also important to remember that the preceding discussions were focused mainly on JICF experiments with limited sample sizes, while the model is more abstract and can be used to represent non-JICF architectures such as the multiple, high mass-ratio jets employed in [81].

4.4 Minimum NO Configuration

In all the results presented up to this point, the main stage equivalence ratio was fixed at ϕ_{main} = 0.372. In order to examine the minimum obtainable NO level at the same overall fuel-air ratio (with T_{final} = 1975 K), an optimization study was conducted for fixed entrainment characteristics, specifically $\tau_{ent,sec}$ and $\tau_{ent,main}$, using the methods described in the Section 4.1.5. We choose a relatively short secondary entrainment time of 1 ms and long main entrainment time of 5 ms, that is, a scenario where main burner finish entraining later than the jet fluid.

In the optimization, the free design variables were ϕ_{main}, M_{sec}/M_{total}, and the secondary stage residence time, $\tau_{res,sec}$. The M_{sec}/M_{total} was used in place of ϕ_{sec} to more easily permit the specification of constrains on the allowable fraction of mass injected at the secondary stage. ϕ_{sec} can be found from this value through Equations 4.5. The three design variables along with their associated bounds are summarized in Table 4.3 below.

Table 4.3: Design parameters and the associated bounds used by the optimization algorithm to find minimum NO levels.

Parameter	**Lower Bound**	**Upper Bound**
ϕ_{main}	0.35	0.63
M_{sec}/M_{total}	0.01	0.20
$\tau_{res,sec}$	5 ms	15 ms

In addition to the bounds on the design parameters in Table 4.3, which are specified as linear inequality constraints in Dakota, the same 125% CO_{eq} constraint used in Sections 4.2 and 4.3 is applied here. This constraint means that solutions can only have CO levels

of at most 25% higher than the equilibrium levels.

Thus the constrained minimization problem is posed as[5]:

$$\min_{\phi_{main},\phi_{sec},\tau_{sec}} \quad \text{NO}(x) \tag{4.10}$$

$$\text{s.t.} \quad \tau_{ent,main} = 5ms \tag{4.11}$$

$$\tau_{ent,sec} = 1ms \tag{4.12}$$

$$M_{sec}/M_{total} \leq 20\% \tag{4.13}$$

$$\text{CO}(x) \leq 1.25 \times \text{CO}_{eq}(\phi_{global}) \tag{4.14}$$

$$\frac{|T - T_{ad}(\phi_{global})|}{T_{ad}(\phi_{global})} \leq 0.01 \tag{4.15}$$

For the above operating conditions, entrainment limits, design parameters and constraints, the optimum solution identified a minimum NO of 3.2 ppm (corrected). The optimal design parameters for this solution are $\phi_{main} = 0.351$, M_{sec}/M_{total} = 20% (the corresponding $\phi_{sec} = 1.86$), and $\tau_{res,sec} = 5$ ms. The result for the secondary mass ratio is at the upper bound of the allowed range, while the optimal $\tau_{res,sec}$ and ϕ_{main} are essentially at the lower bounds for those parameters. Given that the optimal solution has a ϕ_{main} close to the value examined in the previous sections, the result for ϕ_{sec} is also consistent with the previous findings. The optimal value for $\tau_{res,sec}$ matches $\tau_{ent,main}$ for this case; no additional residence time is required once the main stream is fully entrained as the CO constraint is already met.

Table 4.4: Optimum solution determined from the finite-rate entrainment model.

Optimal Result/Parameter	**Value**
NO (ppm, corrected)	3.2
ϕ_{main}	0.351
M_{sec}/M_{total}	0.20
$\tau_{res,sec}$	5 ms

[5]Based on the notation introduced in 2.11

While these results indicate the optimal design requires a very lean main burner, it is useful to examine the NO levels over the parameter space covered in the optimization study (Figure 4.16). While NO is a stronger function of ϕ_{sec} than ϕ_{main}, there *is* a region where ϕ_{main}approaches ϕ_{global} where NO levels begin to drop again, although not to the levels achieved at the lower end of the ϕ_{main} range. By making ϕ_{main} approach ϕ_{global}, we are in fact recovering the LPM NO_x limit.

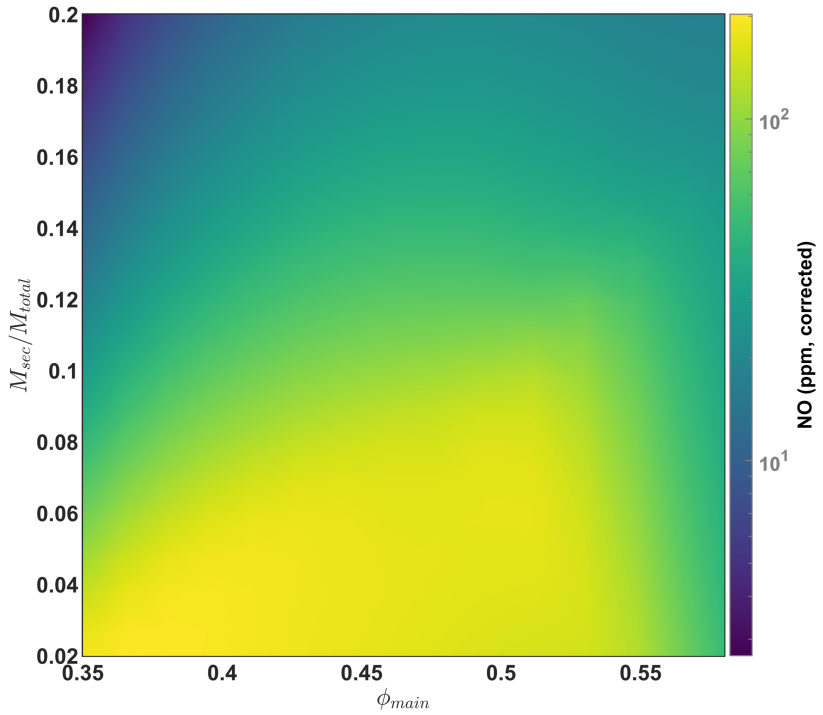

Figure 4.16: Variation in NO over ϕ_{main} and M_{sec}/M_{total} for $\phi_{global} = 0.635$, $\tau_{ent,main} = 5$ ms and $\tau_{ent,sec} = 1$ ms.

4.5 Chapter Summary

In this chapter, simulation results based on a reduced-order model of a staged combustor that captures finite-rate entrainment between the main burner stream and the secondary reactants stream were presented. The generic staged combustor flow field was partitioned into three regions, two with pure fluid (main or secondary) and one being the entrained region containing both fluids. The entrained region is assumed to have infinitely-fast small-

scale mixing, meaning that it is homogeneous at all times.

The effect of finite-rate entrainment on NO_x emissions in a fuel-staged (i.e., pure fuel secondary injection) combustor was characterized using the finite-entrainment model. The simulation results indicate that entrainment is indeed a key parameter that can result in significant variations in NO_x emissions — by two orders of magnitude compared to the fundamental minimum limits in some cases. NO_x levels increase monotonically with $\tau_{ent,main}$, but the rate of increase is more heavily influenced by the ratio between the main and secondary entrainment time scales, r_τ. More specifically, a value of r_τ exists for each $\tau_{ent,main}$ where NO reaches its peak, and exhibits very high sensitivity to $\tau_{ent,main}$. The fundamental mechanisms behind this trend were elucidated in this chapter. Time traces obtained using the finite-entrainment model indicate that the NO peaks correspond to combinations of $\tau_{ent,main}$ and $\tau_{ent,sec}$ that result in a combination of high overshoot temperatures and long dwell times at those temperatures. The ignition delay τ_{ign} was found to directly influence the residence times; later ignition delays lead to shorter times spent at the final temperature. τ_{ign} also affects the magnitude of the temperature overshoot by influencing the equivalence ratio at which the mixture ignites, ϕ_{ign}, though ϕ_{ign} is also influenced by the relative entrainment rates of both streams as well as the main burner equivalence ratio. A region of low NO_x (below 10 ppm) was found in the region where $\tau_{ent,main} < 5$ ms and $r_\tau \leq 1.2$.

Investigations into the effect of fuel and air staging showed that in general, a decrease in ϕ_{sec} leads to reduced NO_x. However, depending on the entrainment time scales, NO_x reduction benefits may be small before ϕ_{sec} is sufficiently decreased. For a $\tau_{ent,main}$ of 5 ms, a ϕ_{sec} of below 2 is sufficient to main NO_x levels below 10 ppm. This ϕ_{sec} value corresponds to roughly a 20% contribution from the jet to the overall system mass, which is on the upper end of what can reasonably be achieved in JICF-based systems. The fundamental parameter enabling fuel-air staging to reduce NO_x is again the ignition delay τ_{ign}. As ϕ_{sec} is decreased, the contribution of the jet to the total system mass increases, thus the entrained region starts colder. The lower initial temperature leads to increased ignition

delay which, as mentioned in the previous paragraph, decreases dwell time at high temperatures and potentially decreases the equivalence ratio at which the entrained region burns, thus reducing the magnitude of the temperature overshoot. Results obtained under fixed entrainment *rates* (as opposed to entrainment time scales) also indicate that a lower ϕ_{sec} leads to lower NO_x levels. The trends identified in this section match those of Sirignano *et al.* [2], where NO_x emissions are found to decrease with increasing lift-off height of the reacting jet in crossflow.

Finally, a constrained optimization study is conducted for the $\tau_{ent,main}$ = 5 ms, $\tau_{ent,sec}$ = 1 ms case to determine the minimum NO_x achievable under these finite entrainment constraints. The minimum NO level was found to be $\sim$3 ppm, and the enabling configuration was one of a very lean main burner with as lean a jet as the constraints would allow. The optimal secondary residence time was one that allowed for sufficient CO oxidation under the limitations of finite-rate entrainment. As such, 5 ms was required to achieve the 3 ppm NO levels, as opposed to the optimal 0.2 ms secondary residence times determined in Section 3.4. These results are promising for the staged combustion architecture because it shows that even under finite-rate entrainment limitations, the design space still allows for NO_x levels that are lower than the theoretical minimum NO_x limits for the LPM architecture.

CHAPTER 5
FINITE-RATE MIXING EFFECTS

The previous chapter explored the effects of finite-rate entrainment on NO production in an axially staged combustor. This chapter describes the development of an original reactor network model to investigate finite-rate mixing, and application of the model to examine finite-rate mixing on NO_x in axially staged combustors with infinite-rate and finite-rate entrainment.

5.1 Limitations in Current Finite-Rate Mixing Models

5.1.1 PaSR Background

Previous work on the effects of finite-rate mixing on chemistry have employed *Partially-Stirred Reactors* (PaSRs) [82–84] that provide some control over the rate of turbulent mixing. The PaSR is a probability density function (PDF) method that is frequently used to solve the closure problems that arise in CFD-based modeling of turbulent reacting flows, as well as to compare the performance of different molecular mixing models and numerical algorithms [85]. It is a Lagrangian approach in that multiple particles are represented in an ensemble that approximates the joint composition PDF.

The typical PaSR configuration is similar to a PSR. Multiple inlet streams enter a constant-pressure reactor at prescribed mass flow rates and remain in the reactor for a given residence time $\tau_{res} = \overline{\rho}V/\dot{m}$. Fluid at the mean thermochemical state exits the reactor at a rate equal to the sum of the inlet mass flow rates. [85]. The main difference between PaSRs and PSRs lies in the former's inclusion of finite-rate molecular mixing, which is characterized by a mixing time scale τ_{mix}. This characteristic mixing time is often considered to be proportional to the turbulent eddy turnover time, i.e., roughly the time taken

for turbulent kinetic energy to dissipate at the smallest scales [86]. The ratios between τ_{res} or τ_{mix} and τ_{chem} give a measure of control over whether or not a given scenario is chemical rate-limited. Furthermore, if $\tau_{res}/\tau_{mix} >> 1$, mixing occurs on a shorter time scale than the residence time so fluid exits the reactor in a homogeneous state. This is the limit corresponding to a PSR. On the other hand, if $\tau_{res}/\tau_{mix} << 1$, the fluid stream entering the reactor does not mix with fluid already in the reactor, so the reactor is inhomogeneous. This is the limiting case corresponding to a plug-flow reactor.

The ANSYS CHEMKIN software package implements the PaSR model developed by Correa [86]. As mentioned above, the joint composition PDF is approximated by Lagrangian particles, which are in turn described by a system of $(N_s + 1) \times N_p$ first-order time-dependent ODEs where $N_s \equiv$ the number of species and $N_p \equiv$ the number of particles in the ensemble. In CHEMKIN, the PaSR simulation is broken into three steps [84]:

1. Through-flow/entrainment: the states of a certain number of particles in the ensemble (i.e., set of equations) are replaced with those of incoming mixtures

2. Molecular mixing: Particles in the ensemble are allowed to interact based on a prescribed mixing rule. Examples of scalar mixing models include the Curl mixing model [87], the IEM (Interaction-by-Exchange-with-the-Mean) model [88–90] and the EMST (Euclidean Minimum Spanning Tree) model [91]. The PaSR is modeling transport of the joint-composition PDF due to turbulent mixing, meaning that the enthalpy and composition vector participates in this mixing step.

3. Chemical reactions: The (stiff) system of ODEs and the underlying chemical kinetics are integrated numerically by a time step Δt.

5.1.2 CHEMKIN PaSR Validation and Limitations

A study using the PaSR model implemented in ANSYS CHEMKIN was performed to validate the CHEMKIN implementation against published results in [82]. In his study,

Correa used a 50% CO and 50% H_2 (by volume) syngas fuel mixture, which was then premixed with air at a stoichiometry such that the equilibrium temperature rose by 1000 K (from an initial mixture temperature of 1000 K). This temperature rise corresponds to $\phi = 0.37$. The residence time of the reactor was 5 ms, simulations used between 100 and 300 particles, and mixing times analyzed were 0.1 ms, 0.316 ms, 1.0 ms and 10 ms. This mixing time scales span "the inertial sub-range of turbulence expected in practical devices."[82]

In order to replicate the above conditions in Chemkin as closely as possible, the 18 species and 43 reaction mechanism for CO/H_2 combustion used by Correa is imported into Chemkin, with thermodynamic and transport properties sourced from GRI-Mech 3.0. Figures 5.1 and 5.2 compare the time-evolution of ensemble averaged temperature and NO mass fraction for Correa's implementation and CHEMKIN's implementation of the PaSR. Because the deterministic IEM model is used by Correa and in the current validation study, the stochastic fluctuations in these time traces are caused only by the random nature of the through-flow. If a stochastic mixing model such as the Curl model were used, then the mixing step would be an additional source of stochasticity.

The results presented in Figures 5.1 and 5.2 show reasonable agreement between the CHEMKIN PaSR and Correa's results. The stochastic steady-state temperature agrees well when $\tau_{mix} = 0.1$ ms, but is roughly 5% lower for the cases with slower mixing ($\tau_{mix} = 1.0$ ms and 10 ms). NO results for the two implementations are within 5 ppm of each other at the steady-state converged solution.

However, preliminary staged combustor simulations, presented below, indicate that the PaSR is not a suitable model for the purposes of NO_x prediction in staged combustors. This is because the PSR-like implementation of a PaSR (i.e., its implementation as a flowing system), along with its quasi-steady state nature, do not accurately represent the evolution of a fluid packet as it moves downstream in a combustor. Rather, the results must be seen as a steady-state snapshot of the statistical distribution in a non-homogeneous region

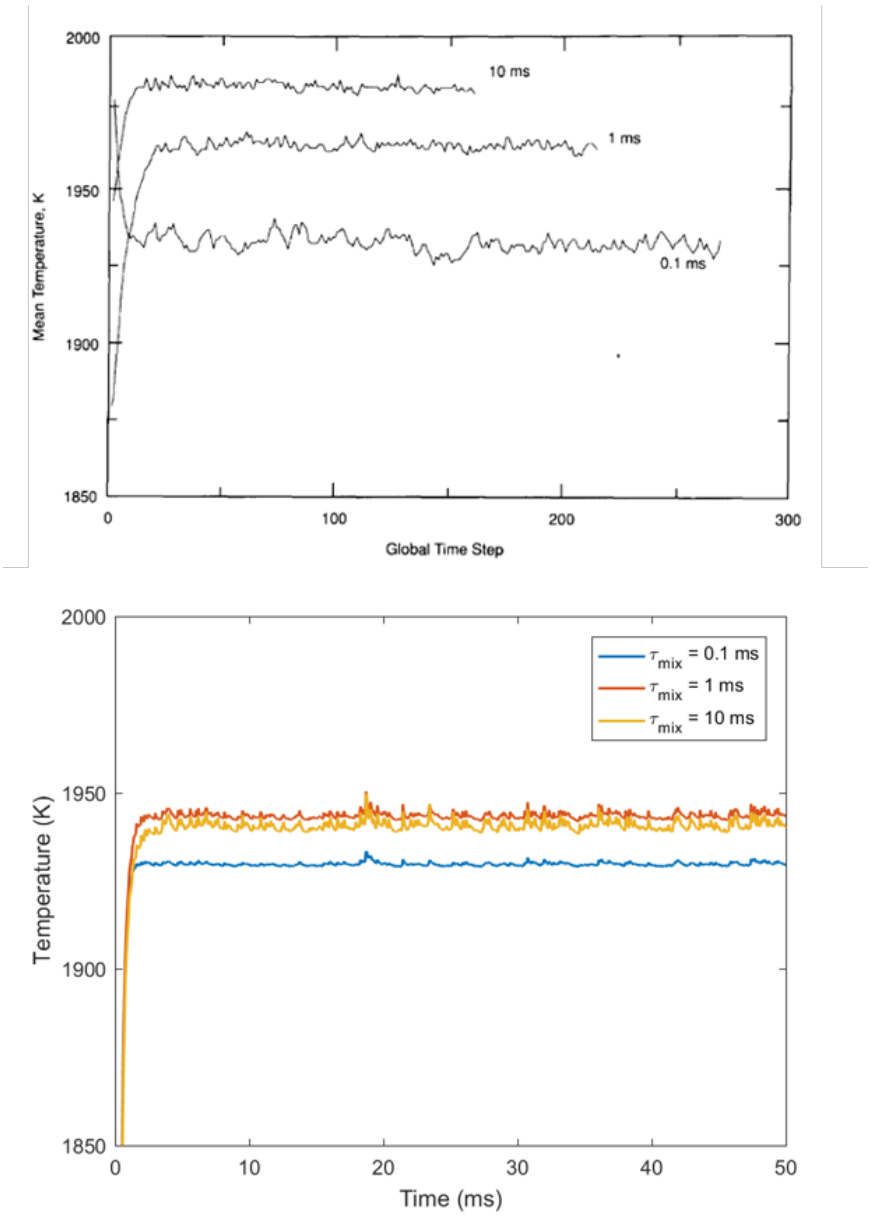

Figure 5.1: Comparison between ensemble average temperatures (i.e., average temperatures across all particles in the reactor) for Correa's PaSR (top) and CHEMKIN's implementation.

that represents the secondary stage, wherein the contents have on average been in the region for τ_{res}. In retrospect, this is the perspective under which the PaSR was designed, especially considering that its primary application today is to determine the evolution of a joint velocity-composition PDF in a given CFD grid cell as a closure to the subgrid/-subfilter scale terms. This paradigm is fundamentally different from the approach that has

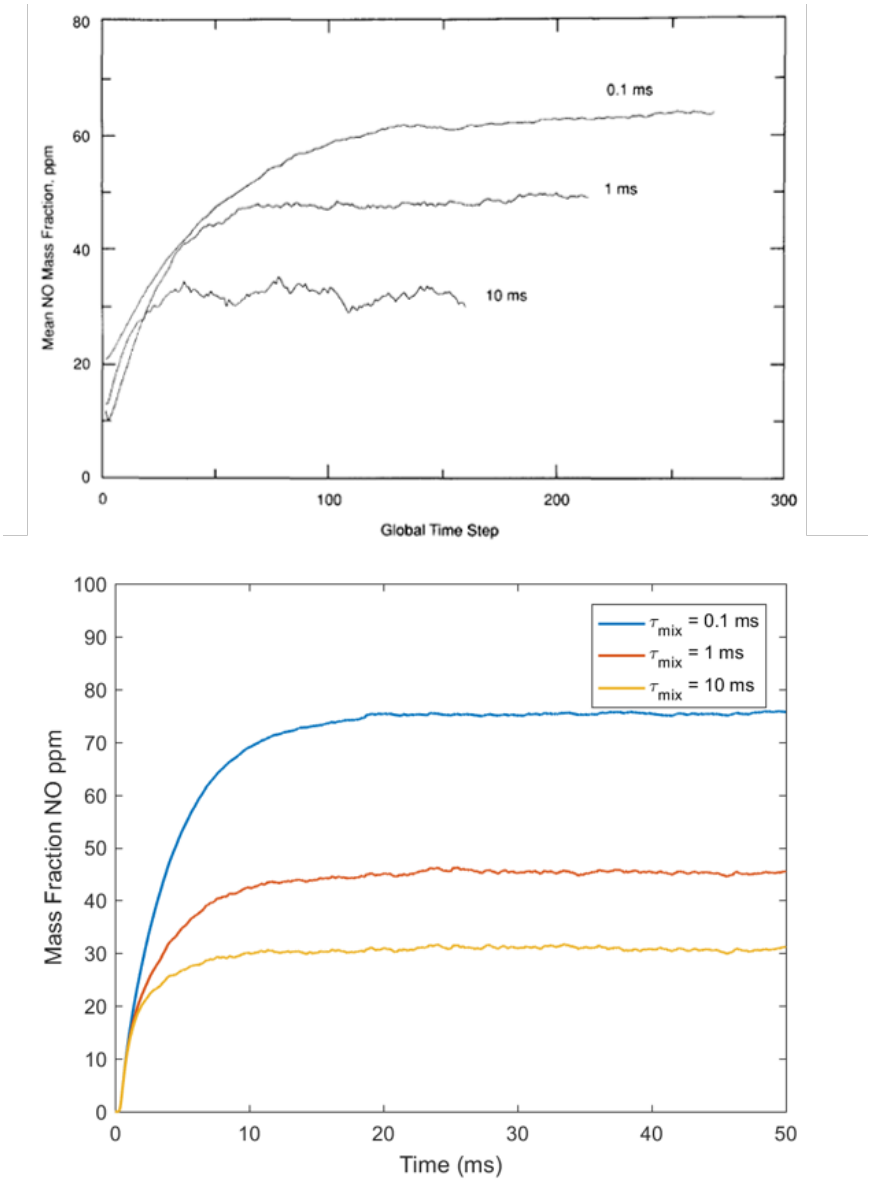

Figure 5.2: Comparison between ensemble average mass fraction of NO for Correa's PaSR (top) and CHEMKIN's implementation (bottom).

been taken thus far in this thesis, namely that each of the secondary stage models hitherto described simulate a set of reactants as it travels along the combustor.

Aside from the conceptual dissimilarity, these studies demonstrated that the CHEMKIN PaSR does not allow for exact specification of entrainment rates due to its stochastic particle-replacement approach. Instead, a proxy for the entrainment rates is specified — the number of particles replaced at each through-flow step. This number, NREP, is then

allocated to each stream based on the ratio of the flow rates, thus resulting in additional sensitivity to the number of particles used in the PaSR, NPAR.

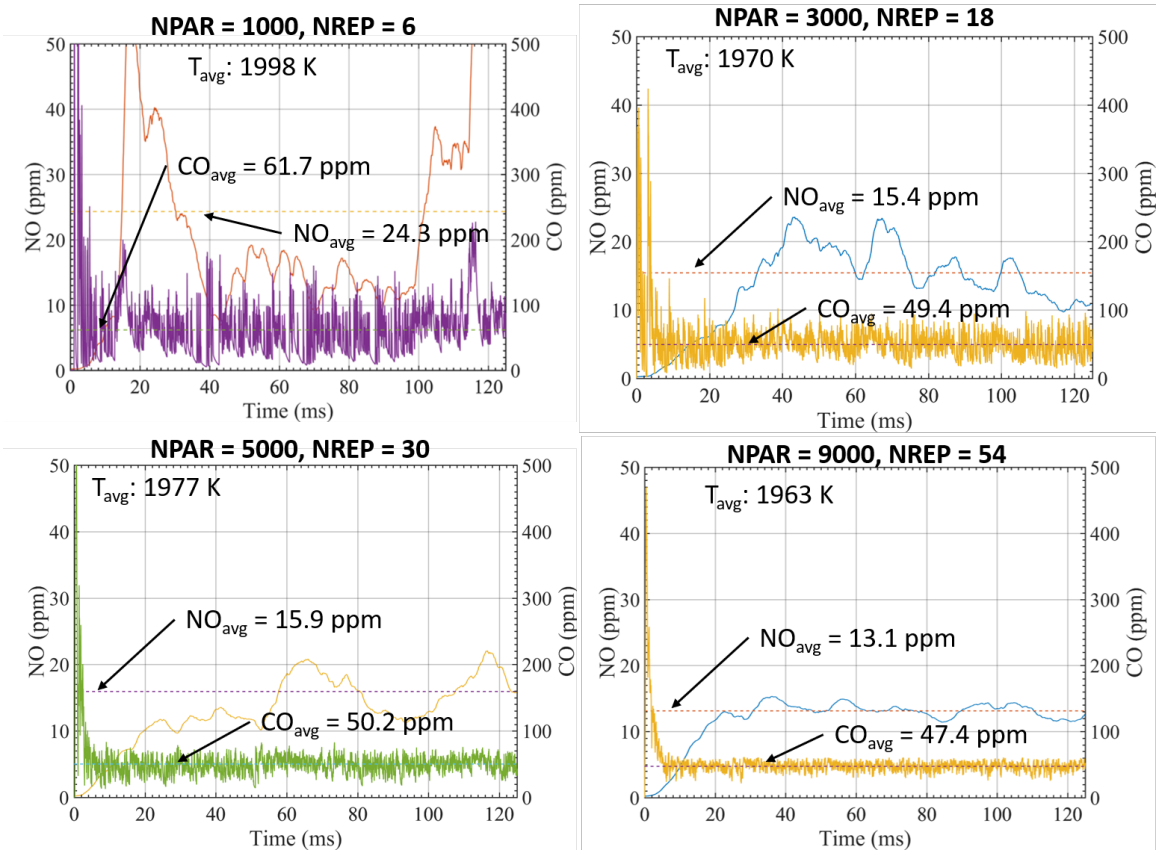

Figure 5.3: NO and CO prediction time histories from the CHEMKIN PaSR model of an axial fuel-staged combustor for $\phi_{global} = 0.64$, $\phi_{main} = 0.37$ and $\tau_{mix} = 0.05ms$ for different NPAR-NREP combinations. Note that both variables are equally scaled by multiples of 3, 5 and 9 from the base case of NPAR = 1000 and NREP = 6.

Figure 5.3 shows an example of the sensitivity to NREP and NPAR through results obtained from four fuel-staged combustor PaSR simulations. In these four cases, the reactor residence time τ_{res} as well as all inlet flow rates were held constant. The mixing time τ_{mix} was fixed across all four cases at 0.05 ms[1]. These results show that, despite holding constant what one would consider to be the key parameters in a staged combustor, NO still varies by around 50%.

[1]Recall that τ_{mix} represents the time taken for turbulent eddies to dissipate.

5.2 Limited Mixing and Entrainment (LiME) Reactor

5.2.1 Conceptual Description

The above limitations of the PaSR model, paired with the slowness of the CHEMKIN implementation, make it unsuitable as a reactor for staged combustor emissions prediction that incorporates both finite-rate large-scale entrainment and small-scale mixing models. Thus a new, compatible reactor model is required to implement small-scale mixing

This new approach, the Limited Mixing and Entrainment (LiME) reactor, is similar to the CHEMKIN PaSR in that it is also a Lagrangian method that can be used to derive PDFs of a given region, but it is conceptually closer to batch reactors than PSRs. In fact, batch reactors are used as the underlying Lagrangian particles. Figure 5.4 illustrates the time evolution of a batch of reactants in this reactor model.

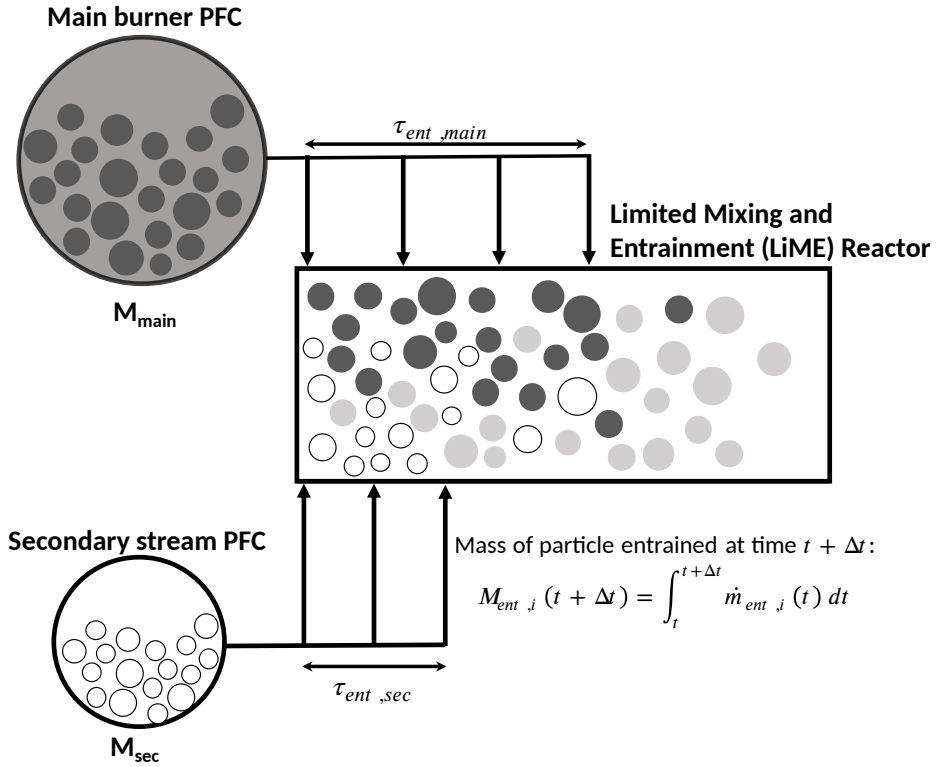

Figure 5.4: Illustration of the time evolution of a batch of reactants within LiME (Limited Mixing and Entrainment) Reactor

As described in Section 1.2.4, mixing is composed of two different regimes — fine-

scale mixing and large-scale entrainment. In this paradigm, small-scale mixing in the LiME reactor can be seen as the limiting step before diffusion drives a local region to a homogeneous, molecularly mixed state. By including both these aspects of entrainment and mixing, it can be used to examine their relative importance on NO_x chemistry in staged combustors.

The effect of macromixing is captured by limiting/tailoring the entrainment rate of reactants into the reactor because particles cannot be mixed until they are first brought together by large-scale structures. One of the main advantages of the LiME reactor compared to the CHEMKIN PaSR implementation is that it allows direct control over the entrainment rate. By prescribing different entrainment rates, one essentially looks at a different section or *magnification* of a flow field. For instance, a constant entrainment rate of secondary reactants into main burner products could represent an axial multi-staged combustor whereby each secondary injector has the same mass flow rate, while an entrainment of main burner products into secondary reactants whose rate increases in time could represent the windward side of a JICF. In Chapter 4, the entrainment rates of *both* the main burner and the secondary streams into the reactor were varied to examine their effects on NO_x emissions.

The LiME reactor takes inspiration from the PaSR in its treatment of micromixing, whereby prescribed models govern the interaction between particles. Taken from [92, p. 265], Table 5.1 lists the constraints (I-III') and desirable properties (i - vi) of micromixing models.

Despite the effort that has gone into improving existing mixing schemes, it is unlikely that a model will be developed which completely satisfies all of the desirable properties listed in Table 5.1 [92]. In light of the ongoing developments and the various mixing models in literature which have their own pros and cons, the LiME reactor is developed in such a way as to accommodate various molecular mixing models, as we will discuss below.

[2] i.e., scalar variances should decay at the correct rate
[3] Reynolds Number = Ratio of inertial forces to viscous forces
[4] Schmidt Number = Momentum diffusivity/Mass diffusivity
[5] Dahmkohler Number = Chemical timescale/Mixing timescale

Table 5.1: Constraints and desirable properties of micromixing models taken from [92]. Note that not all constraints and properties are essential for the present use case where the system does not have an exit.

(I)	Model must leave the scalar mean unchanged
(II)	Model must yield the correct joint scalar dissipation rate[2]
(III)	Model must be uncorrelated with the velocity at high Reynolds numbers
(III')	Model must yield the correct local scalar isotropy
(i)	The inert scalar PDF should relax to Gaussian form for any initial condition
(ii)	All scalars must remain in the allowable region as determined by mixing and chemistry
(iii)	Any conserved linear combination of scalars must be maintained
(iv)	Scalar mixing should be local in composition space
(v)	The evolution of the scalar PDF should depend on the length-scale distribution of the scalar field
(vi)	Any known Re,[3] Sc,[4] or Da[5] dependence should be included in the model parameters

For the implementation in this thesis, the LiME reactor uses the IEM mixing model. The IEM model is a linear, deterministic mixing process that has been widely implemented due to its simplicity. The equation governing the IEM mixing process is

$$\frac{d\phi_i(t)}{dt} = -\frac{C_\phi}{2\tau_{mix}}\big(\phi_i(t) - \langle\phi(t)\rangle\big) \tag{5.1}$$

where ϕ_i is the state vector of the i-th particle, which typically comprises the enthalpy and composition, τ_{mix} is the mixing time[6], C_ϕ is the mixing-model coefficient [85] and $\langle\phi\rangle$ is the mean thermodynamic state of the reactor, also known as the ensemble average when an ensemble of particles are concerned. It is important to note that τ_{mix} is also typically taken to be the inverse of the mean turbulence frequency, ω [93]. Setting C_ϕ to its typical value of 2.0[7], a simple discretization of Equation 5.1 allows for its use in a time-marching numerical simulation.

[6] $\tau_{mix} = \kappa/\epsilon$, where ϵ is the turbulent kinetic energy and κ is the viscous dissipation rate

[7] Haworth states that $C_\phi = 1.5$ gives satisfactory results

$$\Delta\phi_i(t) = -\frac{1}{\tau_{mix}}\Big(\phi_i(t) - \langle\phi_i(t)\rangle\Big)\Delta t \tag{5.2}$$

$$\begin{aligned}\phi_i(t+\Delta t) &= \phi_i(t) + \Delta\phi_i(t) \\ &= \phi_i(t) - \frac{1}{\tau_{mix}}\Big(\phi_i(t) - \langle\phi(t)\rangle\Big)\Delta t\end{aligned} \tag{5.3}$$

One can show that the IEM model readily satisfies constraint (I) and partially satisfies constraint (II) in Table 5.1, and because the LiME reactor is a closed system with no concept of velocity, constraint (III) is not considered. In terms of the desirable properties, the IEM model is a deterministic model and therefore does not exhibit property (i). It does, however, satisfy (ii) and (iii) because of its linear form. In the IEM model, the scalar variables (elements in the state vector ϕ_i) of all particles interact with every other particle (i.e. with the mean of all particles $\langle\phi\rangle$), thereby posing the possibility of "jump conditions" where the scalar variables see a drastic change in value should the time step be too large. Since the actual process of turbulent mixing is *continuous* in space and time, these jump conditions are inherently non-physical.

5.2.2 Model Implementation

This section details the software implementation of the LiME Reactor. It includes descriptions about the core classes required by the reactor model and the various dependencies between the classes.

`Particle` Class

Because the finite-rate mixing and entrainment model takes its roots in the Lagrangian particle PDF method (namely the PaSR), it is not surprising that Particles are the centerpiece of this model. Rather than implement the particles as individual ODEs in a larger system of equations, this model represents particles in a more literal sense by extending Cantera's

`Solution` objects.

The Cantera `Solution` class is used to represent a particle's thermodynamic and chemical state as well as its transport properties. Rather than include a copy of a Solution object in each particle instance, the particle itself is made a *subclass* of Cantera's `Solution` class. A particle therefore inherits all properties as well as methods of a Cantera `Solution` object because it is itself a Cantera `Solution` object. In addition to these methods, each particle has its own `ConstPressureReactor` and `ReactorNet` objects to which it is linked. This allows for a method `react` to be implemented that enables integration of a single particle's system of ODEs given in Equation 2.10. Particles can also keep track of their own time histories either in Numpy arrays or Pandas DataFrames.

To facilitate mixing, each particle possesses a property `Particle.HY` that represents the thermochemical state of that particle. This is an array of length $N_s + 1$ where N_s represents the number of species in a given chemical mechanism. The first entry of this array is the mass-specific enthalpy of the particle while the remaining entries are mass fractions. During a mixing step, this vector is used in the mixing model. In the IEM model, for instance, $\phi_i(t)$ in Equation 5.1 would be replaced with the vector HY from the i-th particle. While the mass of individual particles may differ, the mass of any given particle typically stays constant throughout a simulation run unless particle coalescing occurs, which will be described in a following section.

`ParticleFlowController` Class

As discussed in Chapter 2, entrainment in this case implies the convective transport of reactants through large-scale coherent structures. Finite-rate entrainment is modeled in Chapter 4 through the use of Cantera `MassFlowController` objects. Mathematically, these objects are linked to a reactor's mass flux terms in the transport equations. Thus whenever the `react` method is called, the flux terms in the transport equation are set to the amount given by the `MassFlowController`'s flow rates.

When dealing with discrete particles as opposed to a single continuous region, it is difficult to achieve as elegant a solution as was done in Chapter 4. Correa's implementation of the PaSR uses a stochastic approach to entrainment/through-flow by replacing particles that are in the ensemble. The number of particles replaced is based on the entrainment rate. Based on evaluations of this method of entrainment in CHEMKIN, it results in a lack of smoothness and an unnecessarily large dependence on the number of particles in order to ensure proper resolution of the entrainment rate.

Entrainment in the LiME reactor is therefore handled through Particle Flow Controller (PFC) objects. PFC objects are charged with a prescribed amount of upstream reactant and linked downstream to the secondary stage LiME reactor. These are particle "factories" that create and inject `Particle` objects of a certain *mass* into the LiME reactor. In addition to the mass of the injected particles, the entrainment rate can also be controlled by how frequently the PFCs introduce particles into the downstream reactor. Furthermore, PFCs are linked to their own copy of Cantera `ConstPressureReactor` and `ReactorNet` objects, and thus can be charged with intermediate/vitiated products of combustion that continue reacting as they are entrained into a downstream reactor.

`LiME` Reactor Class

Finally, the core component that binds the particles and PFCs together is the `LiME` class. The `LiME` class serves the following purposes:

1. Store and manage cleanup of `Particle` objects
2. Handle chemical reaction steps of each particle
3. Manage mixing of particles based on prescribed micromixing rules
4. Maintain a time history of the system's average state, that is, the so-called ensemble average used in Correa and Chen's implementation of the PaSR.

The `LiME` class serves the first purpose by maintaining pointers to `Particle` objects in a Python list data structure. In other words, this reactor is essentially a growing collection of `Particle` objects. Chemical reaction for each particle in the LiME reactor's particle list is handled by manually invoking each particle's `react` function, followed by a mass-averaging of the post-reaction particle states (enthalpies and mass fractions) to arrive at an updated LiME reactor state.

To model small-scale mixing, the `LiME` class has a method `mix` that accepts a mixing time scale τ_{mix}. This method can accommodate in a plug-and-play fashion any micromixing model that prescribes rules for particles to interact and exchange mass. Due to its simplicity and satisfactory performance for the situations considered in this thesis, only the IEM model is implemented so far. However, the code is designed such that implementation of other micromixing models is convenient.

The discretized IEM model given in Equation 5.3 can be implemented as follows for a LiME reactor with N particles and k species. For the mass fraction of species α in particle i,

$$\begin{aligned} Y_i^\alpha(t+\Delta t) &= Y_i^\alpha(t) + \Delta Y_i^\alpha(t) \\ &= Y_i^\alpha(t) - \frac{C_\phi}{2\tau_{mix}} \left(Y_i^\alpha - \langle Y^\alpha \rangle\right) \Delta t \end{aligned} \tag{5.4}$$

where the average mass fraction of α is defined as

$$\langle Y^\alpha \rangle \equiv \frac{\sum_{i=1}^N (m_i Y_i^\alpha)}{\sum_{i=1}^N m_i} = \frac{\text{total mass of } \alpha}{\text{total system mass}} \tag{5.5}$$

Similarly, the enthalpy at the next time step can be evaluated as,

$$\begin{aligned} h_i(t+\Delta t) &= h_i(t) + \Delta h_i(t) \\ &= h_i(t) - \frac{C_\phi}{2\tau_{mix}} \left(h_i - \langle h \rangle\right) \Delta t \end{aligned} \tag{5.6}$$

where the average enthalpy h is defined as

$$\langle h \rangle \equiv \frac{\sum_{i=1}^{N}(m_i h_i)}{\sum_{i=1}^{N} m_i} = \frac{\text{total enthalpy of particle } i}{\text{total system enthalpy}} \tag{5.7}$$

In lieu of its fourth function, the `LiME` class is made a subclass of the `Particle` class. Conceptually, this means that the LiME Reactor is a particle that contains other particles, whose state represents the mass-averaged states of those particles. The `LiME` class provides an interface function called `insert` for PFC objects to introduce new particles.

A key performance-oriented feature of the `LiME` class is the `gobble` function, which enables particles with similar states to be combined into one larger particle. At the end of every reaction step, a looping pairwise comparison is performed across all particles to identify particles that can be coalesced. If the L2 norm of the vector of differences in mass fractions and the normalized specific enthalpy squared is below a specified tolerance, the particles are combined and the individual particle is removed from the LiME reactor's particle list. The number of particles is no doubt an essential parameter to ensure statistical significance when stochastic mixing models are employed. However, a deterministic, mass-based mixing model such as the IEM model used in this study has been observed to be relatively insensitive to the number of particles. Nonetheless, the `gobble` function is an optional one, and can be deactivated by setting the argument `coalesce = False` when calling the reactor's `react` method. Performance has been shown to improve by around 40% with coalescing enabled.

5.2.3 Model Validation

IEM Validation

This section describes preliminary studies performed to validate the mixing functionality of the LiME reactor. The main goals are to ensure the LiME reactor's implementation of the IEM model conserves mass and energy, as well as meets constraints I and II in Table 5.1.

A LiME reactor with three particles are used for this validation study. The initial state of each particle is shown in Figure 5.5. Because this is a study to validate the mixing model, the particles are non-reacting. The `mix` function of the LiME reactor is called with a τ_{mix} of 0.1 ms to simulate finite-rate small-scale mixing.

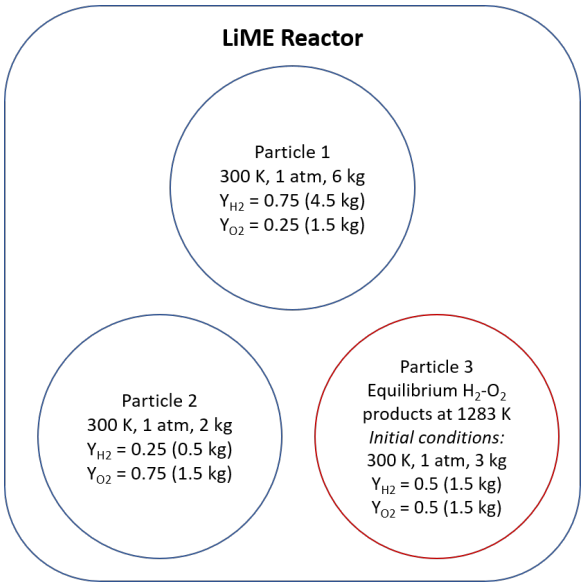

Figure 5.5: Illustration of a LiME reactor with three non-reacting particles used to validate the IEM mixing model.

System time traces of mass and temperature are shown in Figure 5.6. These time traces demonstrate that the IEM mixing model does in fact conserve mass and energy among all three particles despite transporting species and energy between them. There is a small, 1 J rise in system enthalpy, which is a small number potentially due to numerical inaccuracies when the Δt used in Equation 5.3 is finite. Figure 5.7 shows time traces of species mass fraction and temperature in the *particles* themselves, demonstrating that the IEM model does indeed bring all the particles to a mean thermodynamic state.

5.3 Finite-Rate Mixing Effects with Infinitely Fast Entrainment

The next study is intended to isolate the effects of finite-rate mixing on NO_x emissions in a fuel-staged combustor; it is performed with the LiME reactor under the assumption of

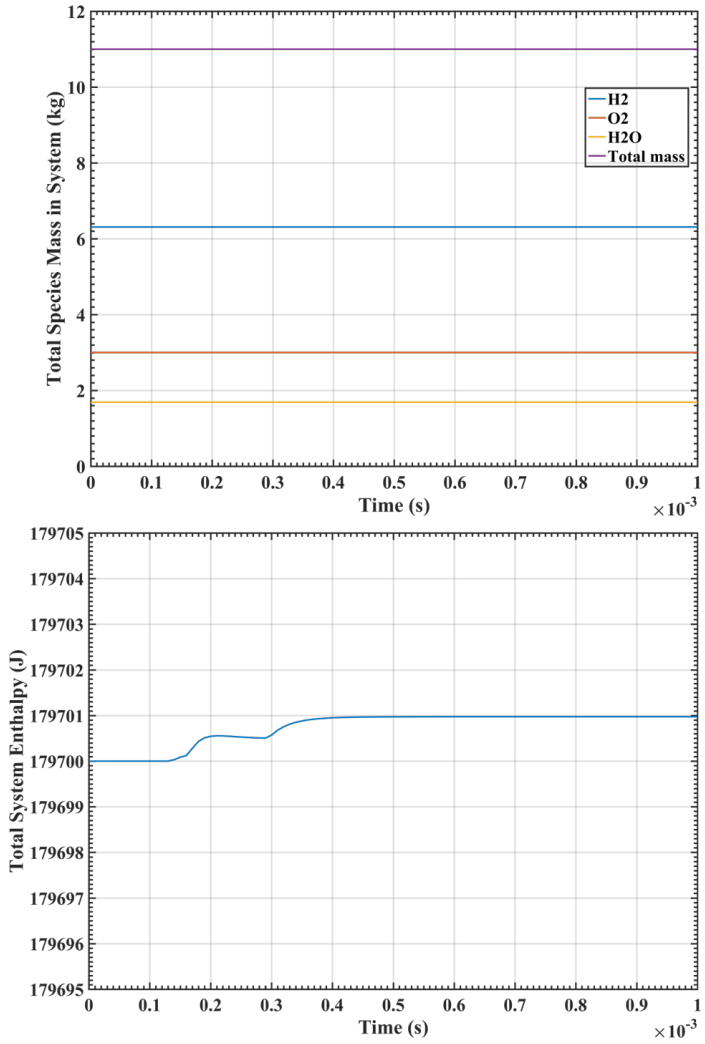

Figure 5.6: Enthalpy and mass time traces for the non-reacting three-particle LiME reactor illustrating that the mixing step conserves mass of each species although they are being transported across different particles. Total system enthalpy is also conserved to within 1 J, which is thought to be a numerical artifact.

infinitely-fast entrainment. The reactor is initialized with two `Particle` objects — a main burner products particle, and a secondary fuel particle.[8]

The overall mixture uses the same baseline global equivalence ratio (0.635) and corresponding final temperature (1975 K) studied in the previous chapters. With a ϕ_{main} of 0.37, this results in the main burner contributing 98% of the total system mass while secondary fuel accounts for the remaining 2%, as shown in Figure 4.3. A 2 ms residence time

[8]The fact that the particles are only prevented from forming a homogeneous mixture by fine-scale mixing (and not large-scale entrainment) means that it is *well-macromixed*.

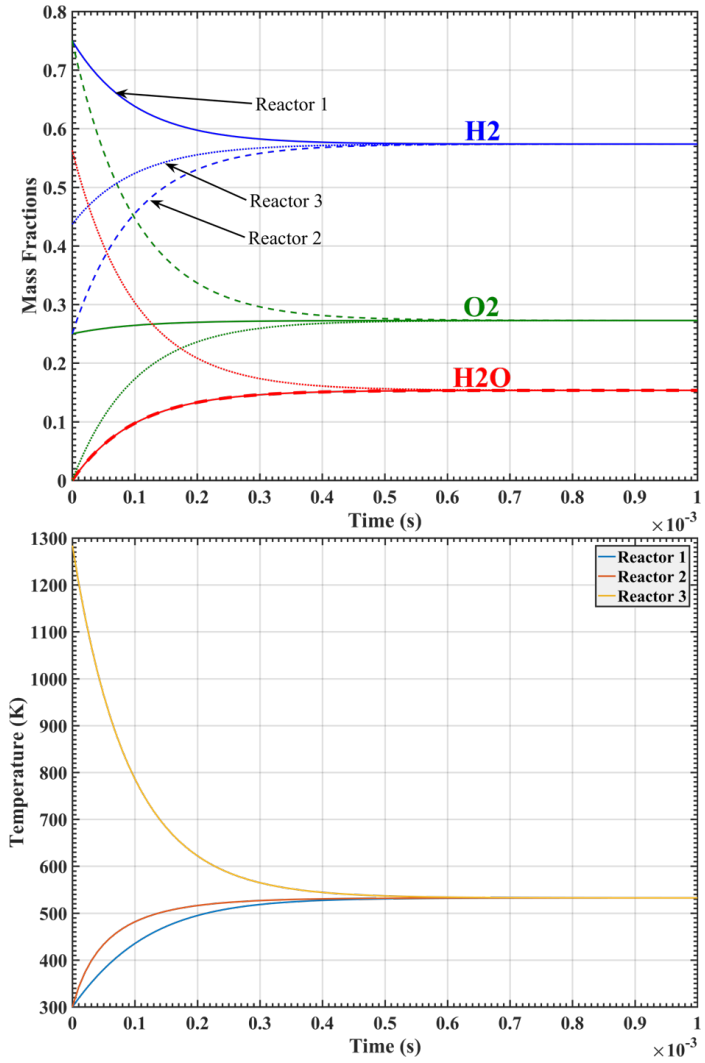

Figure 5.7: Time traces of particle temperatures and mass fractions demonstrate relaxation to the mean achieved by the IEM model.

secondary stage is simulated under four different mixing times τ_{mix} = 0.01, 0.10, 0.20, and 0.30 ms.

From the time traces shown in Figure 5.8, the $\tau_{mix} = 0.01$ ms case closely matches that of Figure 3.3, i.e., infinitely fast mixing and entrainment between the main burner products and secondary fuel before reactions occur. As τ_{mix} is increased, the model accurately captures the formation of temporary high-temperature hot spots in the secondary fuel particle (solid yellow line). Unsurprisingly, NO_x production rates are high in such high-temperature conditions. Compared to the finite-rate entrainment case where the tempera-

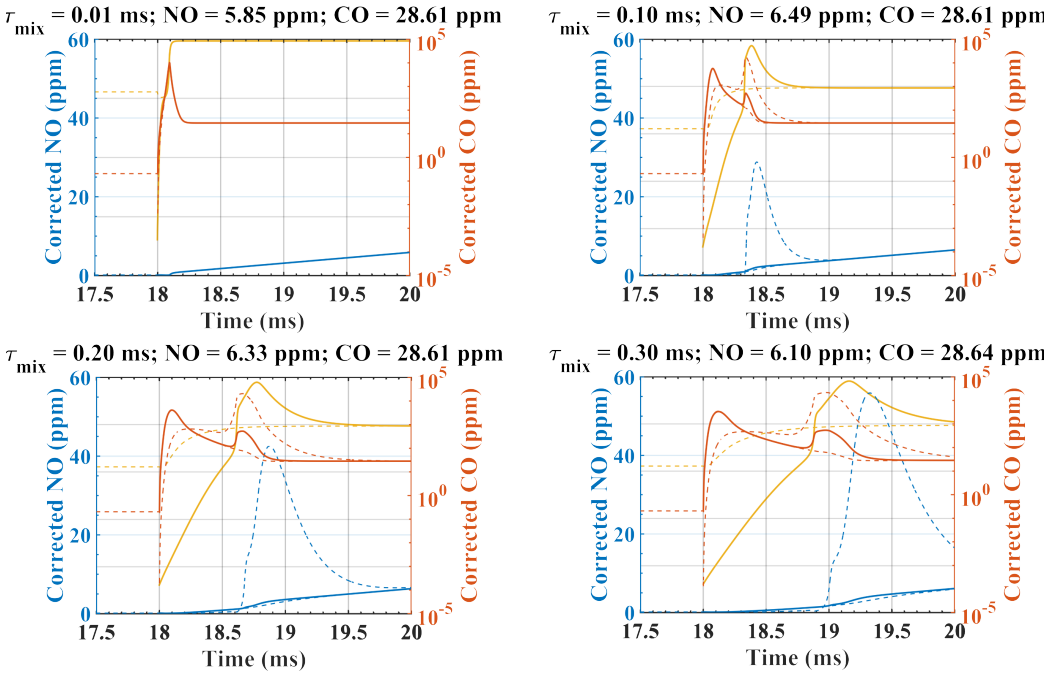

Figure 5.8: Comparison between four different micromixing times of the NO (blue) and CO (orange) histories obtained from the partially-stirred batch reactor model with infinitely fast macromixing. Dashed lines for NO and CO represent the two different particles being used in the reactor, while solid lines for NO and CO represent the mass-averaged values. The temperature histories of each case are overlaid in yellow. Although no scales are shown, the final temperature value at 20 ms for all cases is 1975 K; the emphasis is on the temperature overshoot under finite-rate mixing conditions. The yellow solid line represents the temperature of the secondary fuel particle while the yellow dashed line represents the main burner products particle.

ture overshoot occurs throughout the entire secondary stage, the temperature overshoots in the finite-mixing scenario are limited to specific particles.

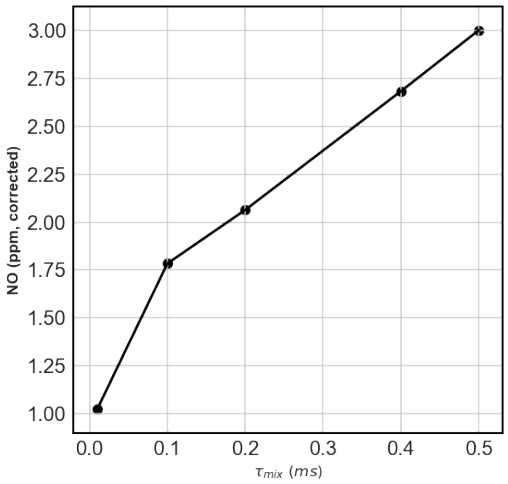

(a) Variation of corrected NO at the 125% CO_{eq} constraint.

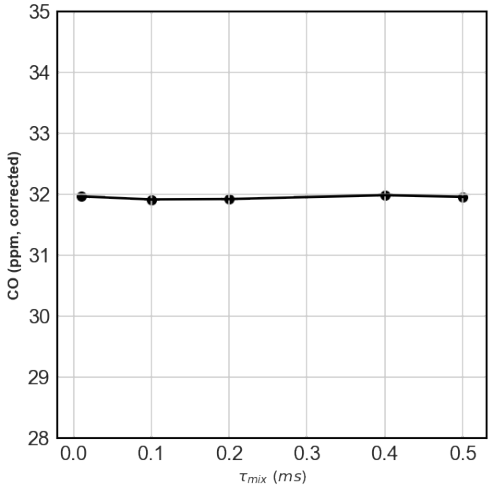

(b) Variation of corrected CO at the 125% CO_{eq} constraint.

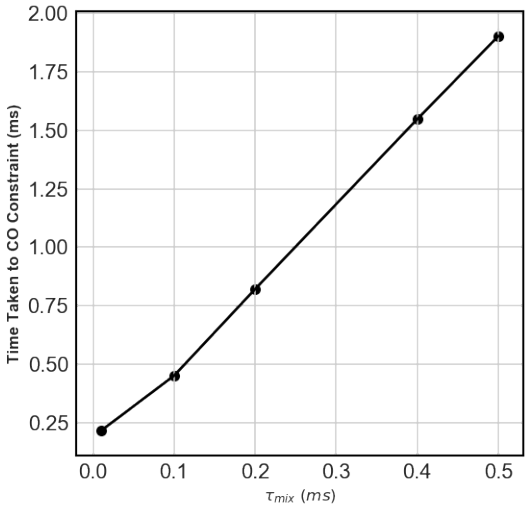

(c) Time taken to reach 125% CO_{eq} constraint

Figure 5.9: Variation in NO and CO at the 125% CO_{eq} constraint with τ_{mix}. Notice that all CO levels are around 32 ppm corrected, which corresponds to the 125% equilibrium CO level for a 1975 K methane-air flame. Time taken to reach the CO constraint is also shown.

Figure 5.9 summarizes the NO results of this finite-rate mixing study with an additional $\tau_{mix} = 0.001$ ms case to simulate the fast-mixing limit. Figure 5.9a shows that compared to finite-rate entrainment effects shown in Chapter 4, NO levels remain relatively low and only increase from 1 to 3 ppm as τ_{mix} slows to 0.5 ms. When $\tau_{mix} = 0.001$ ms, we recover

the fundamental minimum NO limit presented in Section 3.4 under the assumptions of infinitely fast mixing and entrainment. It is important to note that, similar to $\tau_{ent,main}$ and $\tau_{ent,sec}$ in the finite-rate entrainment case, the time required for CO to oxidize does still increase with τ_{mix}, albeit to a smaller extent due to the smaller magnitude of the mixing time scale.

5.4 Finite Mixing and Entrainment Effects on NO_x

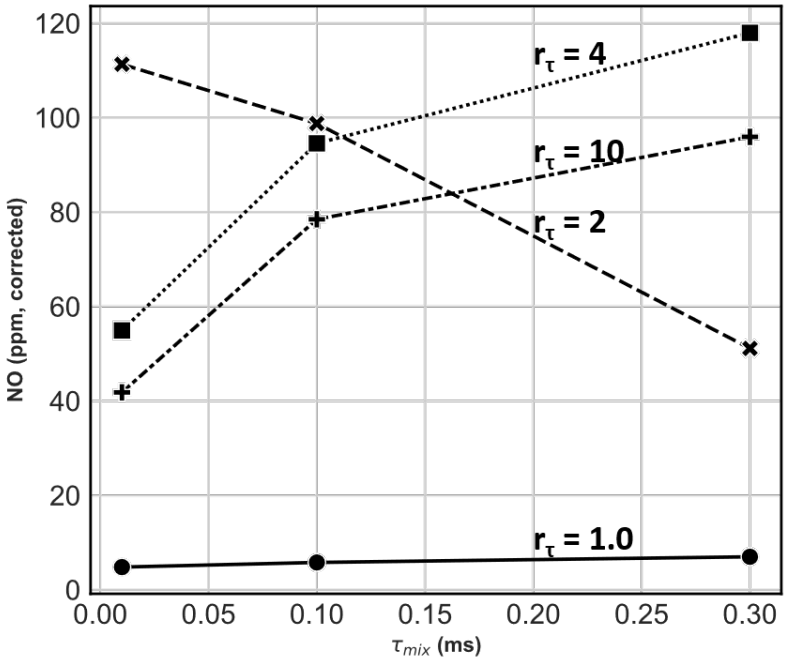

Figure 5.10: Variation of NO with the mixing time scale τ_{mix} for four sets of entrainment time scale ratios, r_τ and $\tau_{ent,main}$ = 2.0 ms.

Using the LiME reactor model, a series of parametric studies were performed to examine the effects of finite-rate mixing under finite-rate entrainment on an axially fuel-staged combustor. Results are presented for a $\tau_{ent,main}$ = 2.0 ms case under four entrainment time scale ratios r_τ = 1, 2, 4, 10, and three mixing time scales τ_{mix} = 0.01, 0.1 and 0.3 ms. Note the mixing time scales were chosen to be much shorter than the main stream entrainment time, as this would be true in virtually all practical configurations. The exit temperature is kept at 1975 K and a fixed main burner ϕ_{main} = 0.3719 is used. Being a fuel-staged

combustor study, pure fuel (CH_4) at 300 K is used at the secondary stream.

NO results, reported from the time where CO reaches the 125% of equilibrium constraint, are shown in Figure 5.10. At r_τ = 1, NO levels are low and only a weak function of τ_{mix}, increasing slightly with τ_{mix}. For the infinite mixing, but finite-rate entrainment conditions discussed in Section 4.2, the r_τ = 1 case produces relatively low NO because the entrainment ratios between the main and secondary streams correspond to ϕ_{global}, which prevents any temperature overshoot regions. In fact, a comparison with Figure 4.4 shows that the NO levels achieved by the fastest mixing case ($\sim$ 5 ppm) are very close to that of the infinite mixing, finite-rate entrainment case. The small increase in NO as the mixing rate is reduced (so τ_{mix} increased) can be partially impacted by increased non-homogeneity in the entrained region. However, as seen in the previous results for infinite-rate entrainment (Figure 5.9c), slowing the mixing also requires increasing residence times for CO oxidation, which would also tend to increase NO.

For the r_τ = 4 and 10 cases, NO increases with τ_{mix} by a factor of 2-2.5 from the fast (τ_{mix} = 0.01 ms) to slow (τ_{mix} = 0.3 ms) mixing cases. Here, the characteristic mixing times approach the secondary stream entrainment times (0.5 ms for r_τ = 4 and 0.2 ms for r_τ = 10). This is preliminary evidence that, in addition to large-scale entrainment rates, finite-rate mixing can play an important and detrimental role in staged combustor NO emissions.

Conversely in the r_τ = 2 case ($\tau_{ent,sec}$ = 1 ms), NO exhibits an inverse relationship with τ_{mix}. Faster mixing in this case encourages higher NO, which may seem a rather surprising result. To further examine this trend, Figure 5.11 shows results plotted against r_τ for fixed values of τ_{mix}. In addition, it includes results from the previous chapter with infinite mixing. We see that r_τ = 2 roughly corresponds to the NO peak caused by a combination of high peak temperatures and residence time at those high temperatures as discussed in Section 4.2. Thus it would appear that in this high-temperature, high residence time regime, a slower mixing rate would help to reduce the peak temperature and/or reduce the residence time spent at those temperatures.

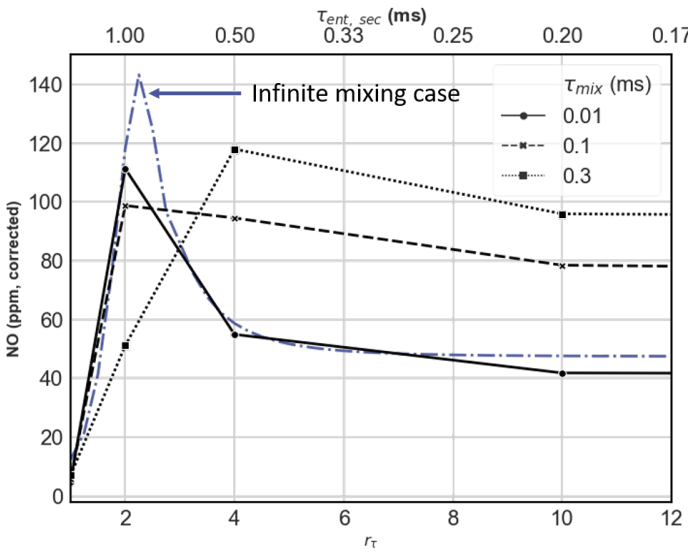

Figure 5.11: Variation of corrected NO (at 125% CO_{eq} constraint) with entrainment ratio r_τ for $\tau_{ent,main}$ = 2.0 ms under different mixing rates. The variation of NO with r_τ for the infinite mixing, finite-entrainment case from Chapter 4 is included as a reference.

The temperature histories of the entrained region (where most, if not all of the NO_x in the secondary stage is produced) shown in Figure 5.12 demonstrate that *both* of these effects are at play when moving from τ_{mix} = 0.1 ms to τ_{mix} = 0.3 ms. In this case, the slower mixing allows the secondary particles (i.e., fluids packets entrained from the fuel stream) to ignite later; at the same time, slower mixing also allows the main burner particles to burn at leaner conditions, thus reducing peak temperatures and time spent at those temperatures. Notice, however, that the secondary fuel particles pass through the same peak temperature in both cases. This indicates that the fuel particles ignite while they are still rich, regardless whether the mixing is fast or slow. Furthermore, this demonstrates the advantage of fuel-air staging previously seen in Section 4.3. By diluting the secondary stream with air the secondary particles remain cooler when they mix partially with hot fluid exchanged from the main burner particles; thus ignition may be delayed until the secondary particles are lean.

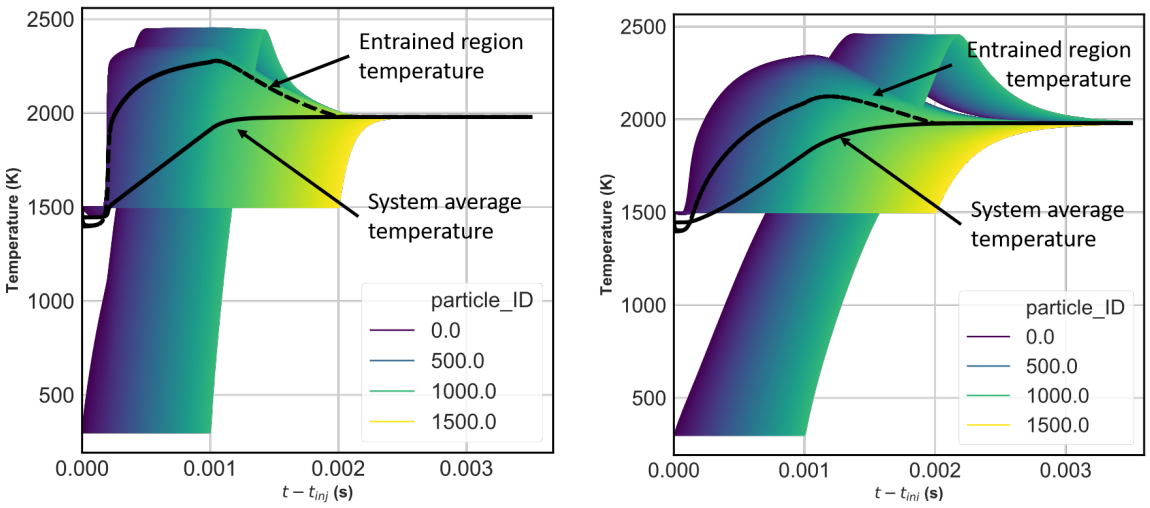

(a) τ_{mix} = 0.1 ms

(b) τ_{mix} = 0.3 ms

Figure 5.12: Temperature histories of each particle in the LiME reactor (entrained region). The average temperature of the entrained region and the entire system (taking into account unentrained reactants) is plotted in black dashed and solid lines, respectively.

5.5 Chapter Summary

This chapter detailed the motivation behind the development of a Limited Mixing and Entrainment (LiME) reactor to simulate NO_x formation in a staged combustor under finite-rate entrainment and mixing. The LiME reactor is a non-uniform collection of small, homogeneous reacting particles that can interact with each other to simulate small-scale mixing. It was developed with parallel computing in mind, and is capable of integrating the network of particles simultaneously.

The Interaction by Exchange with the Mean (IEM) mixing model was implemented in the LiME reactor and validated using non-reacting particles to ensure conservation of mass and energy, as well as uniform decay to the system average mass fractions, enthalpy and temperature. The reactor was developed to accommodate different mixing models in a "plug and play" fashion. In particular, the use of stochastic mixing models would enable the LiME reactor to approximate the joint composition PDF within a given non-homogeneous region.

Further validation studies were performed under the assumptions of infinite-rate en-

trainment but finite-rate mixing. In these studies, the LiME reactor was charged with a main burner products particle and a secondary fuel particle. As the mixing time scale τ_{mix} was reduced, the fundamental minimum NO_x levels identified in Chapter 3 were recovered. These studies also enabled the effect of small-scale mixing to be investigated in isolation, demonstrating that small-scale mixing plays a relatively small role in NO_x emissions under the assumption of infinitely fast entrainment.

Simulations were performed using the LiME model to study the combined effects of finite-rate mixing and entrainment. It was found that τ_{mix} exerts greater influence over NO_x levels when entrainment rates are finite, especially when the secondary stream entrains much faster than the main burner stream (i.e., $r_\tau > 1$). While NO_x increases with τ_{mix} for most values of r_τ, it was found that slower small-scale mixing can actually be beneficial when r_τ is at such a level that overshoot temperatures are high and dwell times at those temperatures are long. For these situations, slower small scale mixing helps to delay τ_{ign}, which provides more time for reactants to entrain so that the particles can reach leaner conditions upon ignition. These results demonstrate that finite-rate entrainment and mixing should be treated simultaneously when designing staged combustors, so as to capture the full array of parameters governing τ_{ign}.

CHAPTER 6
CONCLUSION

The work presented herein was primarily motivated by the demand for novel high-temperature, low-NO_x combustor architectures necessitated by the industry-wide push towards combined cycle plant efficiencies of 65% and beyond. The prohibitive cost of building prototypes relegates full-scale *in-situ* testing to the final stages of the combustor design cycle, while accurate models with turbulence and detailed chemistry cannot be used to efficiently cover the vast design space. This motivated the utilization of reduced-order models, specifically chemical reactor networks (CRN), to efficiently study a broad range of staged combustor architectures. This chapter reiterates major accomplishments and contributions of this thesis. It also summarizes the results that were obtained using different reduced-order models and provides recommendations for future work based on those results.

6.1 Thesis Contributions

6.1.1 Fundamental Minimum NO_x Limits

Using an ideal CRN model of a staged combustor that assumed infinitely fast mixing and entrainment between the main burner and secondary streams, the NO_x reduction potential of the staged combustion architecture was assessed. This ideal CRN model, in conjunction with a constrained optimization package, enabled the determination of minimum NO_x levels achievable by the staged combustor architecture at different firing temperatures. The importance of these theoretical minimum NO_x values should be emphasized. Similar to how the efficiency limits on ideal thermodynamic cycles can be used to gauge the efficiency of a given design, emissions limits based on ideal staged combustors also provide a benchmark so as to better determine the appropriate resource allocation towards staged

combustor R&D efforts.

Compared to the theoretical minimum emissions of standard lean premixed (LPM) approaches, the staged combustor architecture was found to be capable of achieving dramatically lower NO_x levels, e.g., $\sim$1 ppm corrected to 15% excess oxygen at all temperatures below 2000 K, with greater relative NO_x reductions at high temperatures. The single-point minimum NO_x levels were found to be relatively insensitive to the global residence time of the combustor as well as the chemical mechanism used. Moreover, design studies to optimize the axial fuel-staged combustor for multiple operating conditions demonstrated that similar NO levels could be achieved without sacrificing part-load emissions. The need for a constraint on CO in order to define the minimum NO was also introduced.

A major accomplishment in this study is the elucidation of the fundamental parameters governing these emissions limits as they pertain to axial fuel-staged combustor. Specifically, under the assumptions of infinite mixing and entrainment between the main burner and secondary streams, the optimal staged combustor architecture is one with the minimum main burner equivalence ratio that enables rapid secondary stage autoignition and the minimum secondary zone residence time required to meet the CO burnout constraint. Thus the connection between the staged combustor parameters ϕ_{main} and τ_{sec} and the fundamental parameters governing thermal NO production, T and τ_{res}, was established.

6.1.2 Characterization of Finite-Rate Entrainment Effects

Recognizing the practical limitations of the infinitely-fast mixing assumptions used to determine the theoretical minimum NO_x levels, the influence of finite-rate large-scale entrainment on staged combustor NO_x emissions was characterized using a different CRN model. Entrainment time scales were introduced to represent the time taken for a pure fluid stream to disappear in an entrained region.

The time taken for the main burner stream to completely entrain, $\tau_{ent,main}$ is found to be a strong scaling parameter in NO_x production; regardless of the secondary entrainment

rate, NO increases monotonically with $\tau_{ent,main}$. The *ratio* between the main and the secondary entrainment time scales, r_τ, exerts an even greater influence on NO_x. The lowest emissions are generally obtained when $r_\tau < 1$, i.e., when the main stream finishes entraining before the secondary fuel stream. The combination of the longest $\tau_{ent,main}$ and an r_τ of 2.3 produces NO_x levels more than 300x above the theoretical, infinite-entrainment/mixing limit. These trends in NO were found to be governed by temperature overshoots in the entrained region due to combustion at equivalence ratios closer to stoichiometric (compared to the overall equivalence ratio of the staged combustor) as well as the dwell time at high temperatures, both of which are heavily influenced by the autoignition delay time τ_{ign}. If ignition occurs under rich conditions, the entrained region must eventually pass the near-stoichiometric, peak flame temperature condition as the region dilutes toward the lean global equivalence ratio of the system. If it ignites only after reaching a lean condition, the maximum temperature experienced is reduced.

The effect of fuel-air staging (i.e., addition of air to the secondary fuel stream) under finite-entrainment rate scenarios was also characterized. For $r_\tau > 1$, which is the likely scenario in practical devices due to the greater mass/extent of the main stage stream, NO decreases monotonically with the secondary equivalence ratio, ϕ_{sec}, across all entrainment rates. The fundamental parameter enabling this NO_x benefit is the autoignition delay time, which increases with decreasing ϕ_{sec} due to the lower initial temperature in the entrained region[1], thus delaying ignition. The higher τ_{ign} in turn provides more time for fluid to entrain and thus bring the mixture closer to the target equivalence ratio ϕ_{global} before combustion. This elucidation of the mechanism by which ϕ_{sec} affects τ_{ign} verifies that addition of air to the secondary jet in [80] primarily improves NO_x by delaying ignition (liftoff in their case)

In this study, NO_x levels below 10 ppm were obtained with $\phi_{sec} < 2$ for all entrainment rates explored, indicating that including air injection in the secondary stage, or some other

[1]The decrease in the entrained region's initial temperature is in turn caused by the higher contribution of relatively lower-temperature secondary mass.

method of delaying ignition of the secondary stage, is of crucial importance in staged combustor design. While this finding is not completely unexpected, as a similar behavior occurs in RQL (rich-burn, quick-quench, lean burn) combustors, the present work provides insight into the sensitivity of NO emissions to variations in the staged combustor conditions.

This characterization of finite-rate entrainment effects culminated in a constrained optimization study to determine the staged combustor configuration that minimizes emissions under finite entrainment rates ($\tau_{ent,main}$ = 5.0 ms and $\tau_{ent,sec}$ = 1.0 ms). Perhaps unsurprisingly, the combustor design that minimized NO_x was one that contributed as much secondary mass as the constraints would allow (i.e., the lowest ϕ_{sec} allowed), as lean a main burner as possible, and just enough residence time in the secondary stage to ensure sufficient CO burnout. The minimum NO value was found to be $\sim$3 ppm corrected, which is roughly 3x the fundamental limits but well within modern emissions standards.

6.1.3 Limited Mixing and Entrainment (LiME) Reactor Model

Further generalization of the reduced-order model necessitated inclusion of finite-rate (small-scale) mixing effects. Preliminary studies involving the standard approach employed in Partially-Stirred Reactors (PaSR), such as those implemented in ANSYS CHEMKIN, demonstrated the need to develop a custom reactor model in order to accurately represent the evolution of reactants in a combustor under finite-rate mixing and entrainment. Thus a different type of Lagrangian model was developed in this thesis — the Limited Mixing and Entrainment (LiME) reactor.

The LiME reactor is essentially a non-uniform collection of small, homogeneous reacting particles that are allowed to interact with each other to simulate small-scale mixing. It was developed with parallel computing in mind and is capable of integrating the network of particles in parallel. Perhaps more importantly, it uses a novel, semi-continuous approach to fluid entrainment in which particles of given mass are introduced into the LiME reactor as an approximation of the mass flux terms in the governing equations. Precise control over

the entrainment rate is not available with the existing PaSR implementation. The LiME reactor is capable of combining particles of similar thermodynamic states in order to reduce computational cost.

In this thesis, the Interaction by Exchange with the Mean (IEM) method was implemented in the LiME reactor to model the effects of finite-rate small-scale mixing, but the reactor was developed such that other mixing models can be implemented with ease. In particular, the use of stochastic mixing models would enable the LiME reactor to approximate the joint composition PDF within a given region. Non-reacting validation studies were conducted that demonstrated the current implementation enforces the conservation equations and converges each particle's thermodynamic state to the mean system state according to the desired mixing time scale τ_{mix}.

Reacting validation studies using infinite-rate entrainment, but finite-rate mixing further validated the LiME reactor; the fundamental minimum NO values obtained in the earlier infinite-mixing and entrainment study were recovered as the mixing time scale was reduced. For the conditions examined, a τ_{mix} of 0.01 ms is sufficient to achieve this fast mixing. Furthermore, these studies showed that under the assumption of infinite-rate entrainment, small-scale mixing plays a relatively small role in NO_x reduction. That is, fast entrainment is sufficient to achieve low NO_x even with slow-mixing in a fuel-staged combustor.

Finally, a study was performed to study the combined effects of finite-rate mixing and entrainment on NO_x emissions. The mixing time scale τ_{mix} was found to influence NO_x significantly when entrainment rates are finite. This is especially true when the secondary stream entrains much faster than the main burner stream (i.e., $r_\tau > 1$), where the slowest τ_{mix} case of 0.3 ms increased NO_x by more than 2x compared to the infinite mixing case. In entrainment-limited situations, however, where overshoot temperatures are high and high-temperature dwell times are long, slower small-scale mixing is a mechanism by which τ_{ign} can be increased, thereby allowing more time for reactants to entrain before

combustion occurs. Therefore, properties governing small-scale mixing such as the mass and thermal diffusivities of the secondary stream should be considered when designing staged combustors.

6.2 Recommendations for Future Work

6.2.1 Further Design Space Exploration

As a testament to this generalized reduced-order approach, more than 30,000 design points were explored across the various mixing and entrainment cases with many more edge cases explored automatically by the optimization algorithms, and no CAD models were required in the process. A study at this scale is difficult even with relatively "cheap" RANS simulations employing analytically-reduced chemical mechanisms, let alone the detailed mechanisms used in this work. In stark contrast, the extensive experimental characterization performed by Sirignano *et al.* spans 144 interrogation points.

Even so, we have but covered a small portion of the design space; the studies presented in this thesis were mainly for the same exit temperature of 1975 K at an elevated pressure of 25 atm. Further explorations should be performed at various other firing temperatures and pressures to determine if the trends with entrainment and mixing time scales presented in this thesis scale with temperature and pressure.

The finite-rate entrainment study showed cases of up to $\tau_{ent,main}$ = 5 ms, which is presumably shorter than that of an actual staged combustor — one does not expect pure main burner fluid in a typical staged combustor to disappear before the fluid stream leaves the combustor and enters the turbine. Thus the model can be used with more realistic time scales that are either calculated using CFD or measured experimentally in order to determine the best parameters to minimize NO_x in those regimes.

While the current work demonstrated the importance of ignition delay in secondary-stage NO_x reduction, Sirignano suggests isolating the impact of ignition delay through the use of additives that affect the chemical time scales [80]. Such a study would be possi-

ble with any of the models used in this work, with the added advantage of the improved accuracy in autoignition delay prediction due to the detailed chemical mechanisms used herein.

6.2.2 LiME Reactor Performance Characterization and Optimization

It is said that premature optimization is the root of all evil [94]. In lieu of this advice, considerable effort has been taken to validate the LiME reactor model as well as the IEM mixing model to ensure physically valid results, as opposed to refactoring and profiling the code to try and optimize performance. Figure 6.1 shows the performance of a serial version of the LiME reactor. The time required to run a 3 ms secondary stage scales roughly linearly with the average number of particles. That said, it is believed that due to the independent nature of the particles everywhere except the mixing step, the reactor should exhibit favorable scaling characteristics when parallelized. As such, this can potentially be an avenue of future development for the LiME reactor should it see additional users in the future.

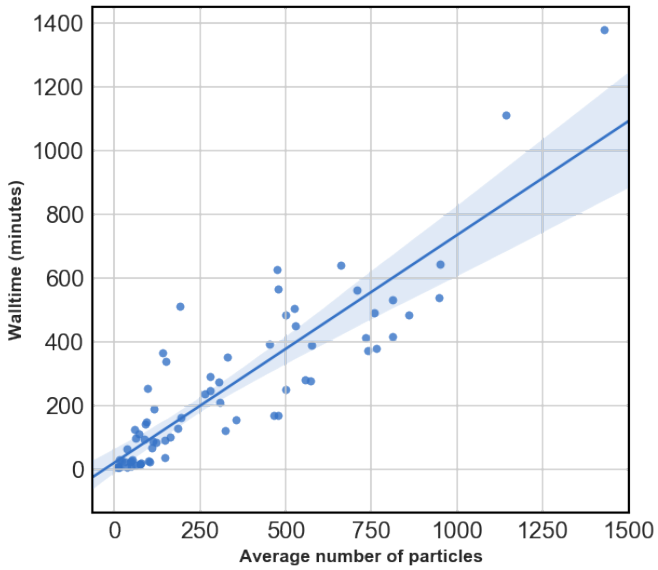

Figure 6.1: Variation in computational walltime with average number of particles in the LiME reactor.

As discussed above, the LiME reactor can accommodate multiple different mixing models, including stochastic ones. The implementation and validation of these models is therefore a task to be undertaken should the need arise for modeling the joint composition PDF. One particular validation study in the case of stochastic models is the number of particles required for statistical convergence. Since the `gobble` function exists to reduce the number of particles, rules need to be in place that prevent the number of particles from dropping below a certain level.

Furthermore, additional development work is required to integrate the LiME reactor into full engine simulations used to predict emissions, such as the hybrid approach described in [60]. Analysis of the LiME model's algorithmic performance and scalability is essential to help engineers in deciding the appropriate models to use in a given task. In addition, assumptions used in the development of the LiME reactor may have to be reassessed when the model is used in unison with other models, e.g., the constant pressure assumption may adversely impact accuracy when simulating an aircraft engine with bleed air and line losses.

6.2.3 Reinforcement Learning Design Optimization Framework

The application of neural networks and reinforcement learning to control chemical processes has been considered long before the modern concept of *deep* reinforcement learning enabled by recent breakthroughs in deep neural networks [95]. Leveraging reinforcement learning to provide an alternative loss function, Hoskins and Himmelblau train neural networks to control nonlinear chemical processes in continuously-stirred tank reactors (CSTR) where no model of the objective function existed. Their neural network compared favorably to the then state-of-the-art (tuned) PID controllers, but were ultimately hindered by the lack of massively-parallel computing architectures required to efficiently train the network. More recently, Zhou *et al.* [96] developed a deep reinforcement learning model that identifies experimental conditions to optimize synthesis reaction outcomes. Their model proved

to be more efficient than state-of-the-art blackbox optimization algorithms, and was successfully pre-trained on microdroplet (simulation) reactions before being applied to batch reactions.

The above examples leverage the predictive capability of neural networks to control chemical processes so as to maximize yield. In the case of combustor design, however, the goal is to manipulate the time-evolution of chemical reactions so as to *minimize* the yield of NO_x while meeting constraints on CO and exit temperature. Using the finite-entrainment model from Chapter 4, an OpenAI `gym` [97] environment has been developed, in which a reinforcement learning agent can be trained to learn the parameters that govern NO_x chemistry. However, an agent that was trained using the Proximal Policy Optimization (PPO2) [98] algorithm learned that the best way to minimize NO_x was to not burn any fuel at all. It is thought that this issue may be caused by an ill-posed reward function, and thus investigations can be performed into the development of this novel combustor design methodology. For the interested reader, the source code for the Gym simulation environment is available at: https://github.com/edwinytgoh/ReinforcementKinetics.

Appendices

APPENDIX A

SUPPLEMENTARY FIGURES

A.1 Chapter 4

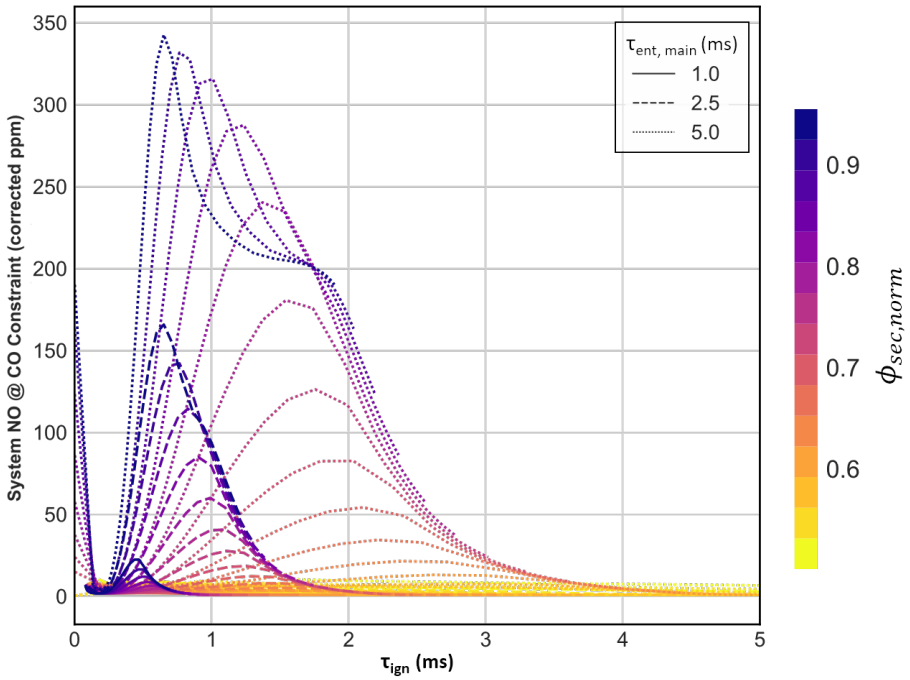

Figure A.1: Variation in system NO at the 125% CO_{eq} constraint with τ_{ign} based on the maximum change in temperature gradient.

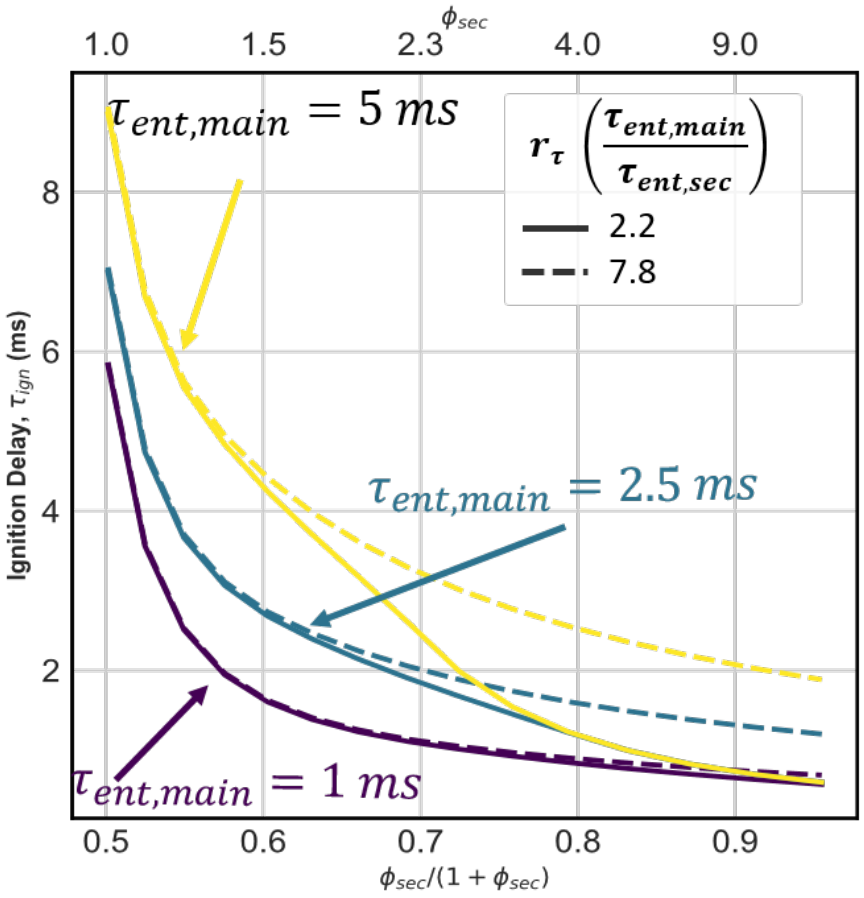

Figure A.2: Variation of ignition delay τ_{ign} with secondary equivalence ratio.

APPENDIX B

SOURCE CODE

The software toolkit and LiME reactor model developed as part of this thesis is available at https://github.com/edwinytgoh/LiME.

REFERENCES

[1] M. Kolb, D. Ahrens, C. Hirsch, and T. Sattelmayer, "A model for predicting the lift-off height of premixed jets in vitiated cross flow," *Journal of Engineering for Gas Turbines and Power*, vol. 138, no. 8, 2016.

[2] M. D. Sirignano, V. Nair, B. Emerson, J. Seitzman, and T. C. Lieuwen, "Nitrogen oxide emissions from rich premixed reacting jets in a vitiated crossflow," *Proceedings of the Combustion Institute*, vol. 37, no. 4, pp. 5393–5400, 2019.

[3] International Energy Agency, *World Energy Outlook 2017*. International Energy Agency, 2017, p. 782, ISBN: 978-92-64-28230-8.

[4] BP Energy Economics, "2018 BP Energy Outlook," BP PLC, Tech. Rep., 2018, p. 124.

[5] V. McDonell and M. Klein, "Ground-Based Gas Turbine Combustion," in *Gas Turbine Emissions*, T. C. Lieuwen and V. Yang, Eds., Cambridge: Cambridge University Press, pp. 24–80.

[6] H. S. Leff, "Thermodynamics of combined-cycle electric power plants," *American Journal of Physics*, vol. 80, no. 6, pp. 515–518, 2012.

[7] R. Kehlhofer, B. Rukes, F. Hannemann, and F. X. Stirnimann, *Combined-cycle gas & steam turbine power plants*. PennWell, 2009, p. 434, ISBN: 9781593701680.

[8] T. C. Lieuwen, M. Chang, and A. Amato, "Stationary gas turbine combustion: Technology needs and policy considerations," *Combustion and Flame*, vol. 160, no. 8, pp. 1311–1314, 2013.

[9] *Modeling of Minimum NOx in Staged-Combustion Architectures at Elevated Temperatures*, vol. Volume 4A: Combustion, Fuels and Emissions, Turbo Expo: Power for Land, Sea, and Air, V04AT04A048, Jun. 2017. eprint: sans mono.fd Sans Mono.fd https://asmedigitalcollection.asme.org/GT/proceedings-pdf/GT2017/50848/V04AT04A048/2433303/v04at04a048-gt2017-63787.pdf.

[10] S. Can Gülen, "Étude on Gas Turbine Combined Cycle Power PlantNext 20 Years," *Journal of Engineering for Gas Turbines and Power*, vol. 138, no. 5, p. 051 701, Oct. 2015.

[11] "Development of Low NOx Combustion System with EGR for 1700řC-class Gas Turbine," Tech. Rep. 1, 2013.

[12] I. Glassman, R. A. Yetter, I. Glassman, and R. A. Yetter, "Chapter 8 Environmental Combustion Considerations," in *Combustion*, 2008, pp. 409–494, ISBN: 9780120885732.

[13] A. Haagen-Smit, "Chemistry and Physiology of Los Angeles Smog," *Industrial & Engineering Chemistry*, vol. 44, no. 6, pp. 13421346, 1952.

[14] American Meteorological Society. (). A look at u.s. air pollution laws and their amendments.

[15] International Energy Agency, "Energy and Air Pollution - World Energy Outlook 2016 Special Report," International Energy Agency, Paris Cedex 15, France, Tech. Rep., 2016.

[16] C. T. Bowman, "Control of combustion-generated nitrogen oxide emissions: Technology driven by regulation," *Symposium (International) on Combustion*, vol. 24, no. 1, pp. 859–878, 1992.

[17] World Health Organization, *Ambient air pollution: a global assessment of exposure and burden of disease*, World Health Organization, Ed. World Health Organization, 2016, ISBN: 9789241511353.

[18] S. R. Turns, *An introduction to combustion : concepts and applications*. McGraw-Hill, 1996, p. 565, ISBN: 0079118127.

[19] A. C. A. Lipardi, J. M. Bergthorson, and G. Bourque, "NOx Emissions Modeling and Uncertainty From Exhaust-Gas-Diluted Flames," *Journal of Engineering for Gas Turbines and Power*, vol. 138, no. 5, p. 051 506, Nov. 2015.

[20] A. A. Konnov, I. V. Dyakov, and J. de Ruyck, "Nitric oxide formation in premixed flames of H2+CO+CO2 and air," *Proceedings of the Combustion Institute*, vol. 29, no. 2, pp. 2171–2177, Jan. 2002.

[21] R. K. Hanson and S. Salimian, "Survey of Rate Constants in the N/H/O System," in *Combustion Chemistry*, W. C. Gardiner, Ed., New York, NY: Springer US, 1984, pp. 361–421, ISBN: 978-1-4684-0186-8.

[22] S. M. Correa, "A Review of NOx Formation Under Gas-Turbine Combustion Conditions," *Combustion Science and Technology*, vol. 87, no. 1-6, pp. 329–362, 1993.

[23] J. A. Miller and C. T. Bowman, "Mechanism and modeling of nitrogen chemistry in combustion," *Progress in Energy and Combustion Science*, vol. 15, no. 4, pp. 287–338, Jan. 1989.

[24] L. Moskaleva and M. Lin, "The spin-conserved reaction CH+N2H+NCN: A major pathway to prompt no studied by quantum/statistical theory calculations and kinetic

modeling of rate constant," *Proceedings of the Combustion Institute*, vol. 28, no. 2, pp. 2393–2401, Jan. 2000.

[25] A. A. Konnov, "Implementation of the NCN pathway of prompt-NO formation in the detailed reaction mechanism," *Combustion and Flame*, vol. 156, no. 11, pp. 2093–2105, 2009.

[26] T. Sattelmayer, A. Eroglu, M. Koenig, W. Krebs, and G. Myers, "Industrial Combustors," in *Gas Turbine Emissions:* T. C. Lieuwen and V. Yang, Eds., Cambridge: Cambridge University Press, 2012, pp. 290–362.

[27] A. Lefebvre and D. Ballal, *Gas Turbine Combustion*. CRC Press, Apr. 2010, ISBN: 978-1-4200-8604-1.

[28] P. Gokulakrishnan and M. S. Klassen, "NOx and CO Formation and Control," in *Gas Turbine Emissions*, T. C. Lieuwen and V. Yang, Eds., Cambridge: Cambridge University Press, pp. 175–208.

[29] P. Gokulakrishnan, M. J. Ramotowski, G. Gaines, C. Fuller, R. Joklik, L. D. Eskin, M. S. Klassen, and R. J. Roby, "A Novel Low NOx Lean, Premixed, and Prevaporized Combustion System for Liquid Fuels," *Journal of Engineering for Gas Turbines and Power*, vol. 130, no. 5, p. 051 501, Sep. 2008.

[30] G. Leonard and J. Stegmaier, "Development of an Aeroderivative Gas Turbine Dry Low Emissions Combustion System," *Journal of Engineering for Gas Turbines and Power*, vol. 116, no. 3, p. 542, 1994.

[31] A. Amato, J. M. Seitzman, and T. C. Lieuwen, "Emissions from Oxyfueled or High-Exhaust Gas Recirculation Turbines," in *Gas Turbine Emissions*, T. C. Lieuwen and V. Yang, Eds., Cambridge: Cambridge University Press, pp. 209–234.

[32] H. Karim, J. Natarajan, V. Narra, J. Cai, S. Rao, J. Kegley, and J. Citeno, "Staged Combustion System for Improved Emissions Operability and Flexibility for 7HA Class Heavy Duty Gas Turbine Engine," in *Volume 4A: Combustion, Fuels and Emissions*, ASME, Jun. 2017, V04AT04A062, ISBN: 978-0-7918-5084-8.

[33] R. E. Jones, "Advanced Technology for Reducing Aircraft Engine Pollution," in *Winter Annual Meeting of the American Society of Mechanical Engineers*, Detroit, Michigan: NASA, 1973.

[34] C. Hassa, "Partially Premixed and Premixed Aero Engine Combustors," in *Gas Turbine Emissions*, T. C. Lieuwen and V. Yang, Eds., Cambridge: Cambridge University Press, pp. 237–289.

[35] S. M. Martin, W. R. Laster, and J. E. P. Bilbao, "Axial stage combustion system with exhaust gas recirculation," pat. 20170114717A1, Apr. 2017.

[36] P. J. Stuttaford, P. Economo, S. Jorgensen, D. Gauthier, and T. Hui, "Axially staged gas turbine combustor with interstage premixer," pat. 9851107B2, Jul. 2014.

[37] V. Hoferichter, D. Ahrens, M. Kolb, and T. Sattelmayer, "A Reactor Model for the NOx Formation in a Reacting Jet in Hot Cross Flow Under Atmospheric and High Pressure Conditions," in *ASME Turbo Expo 2014: Turbine Technical Conference and Exposition*, American Society of Mechanical Engineers, 2014, V04BT04A037–V04BT04A037.

[38] D. Ahrens, M. Kolb, C. Hirsch, and T. Sattelmayer, "NOx formation in a reacting premixed jet in hot cross flow," in *Proceedings of the ASME Turbo Expo*, vol. 4B, American Society of Mechanical Engineers (ASME), 2014, ISBN: 9780791845691.

[39] W. R. Laster, S. M. Martin, J. E. Portillo Bilbao, J. Hardes, and T. A. Fox, "Dual outlet nozzle for a secondary fuel stage of a combustor of a gas turbine engine (us patent 10,139,111)," Nov. 2018.

[40] J. E. Broadwell and R. E. Breidenthal, "A simple model of mixing and chemical reaction in a turbulent shear layer," *Journal of Fluid Mechanics*, vol. 125, pp. 397–410, 1982.

[41] S. Muppidi and K. Mahesh, "Study of trajectories of jets in crossflow using direct numerical simulations," *Journal of Fluid Mechanics*, vol. 530, pp. 81–100, May 2005.

[42] R. Sullivan, B. Wilde, D. R. Noble, J. M. Seitzman, and T. C. Lieuwen, "Time-averaged characteristics of a reacting fuel jet in vitiated cross-flow," *Combustion and Flame*, vol. 161, no. 7, pp. 1792–1803, Jul. 2014.

[43] A. R. Karagozian, "The jet in crossflow," *Physics of Fluids*, vol. 26, no. 10, p. 101 303, Oct. 2014.

[44] S. D. Heister, T. T. Nguyen, and A. R. Karagozian, "Modeling of liquid jets injected transversely into a supersonic crossflow," *AIAA Journal*, vol. 27, no. 12, pp. 1727–1734, 1989.

[45] S. H. Smith and M. G. Mungal, "Mixing, structure and scaling of the jet in crossflow," *Journal of Fluid Mechanics*, vol. 357, S0022112097007891, Feb. 1998.

[46] V. Nair, M. Sirignano, B. Emerson, B. Halls, N. Jiang, J. Felver, S. Roy, J. Gord, and T. Lieuwen, "Counter rotating vortex pair structure in a reacting jet in crossflow," *Proceedings of the Combustion Institute*, vol. 37, no. 2, pp. 1489 –1496, 2019.

[47] V. Nair, B. R. Wilde, B. Emerson, and T. C. Lieuwen, "Spatial development of shear layer vortices in a reacting jet in crossflow," in *AIAA Aerospace Sciences Meeting, 2018*, 2018, ISBN: 9781624105241.

[48] D. R. Getsinger, L. Gevorkyan, O. I. Smith, and A. R. Karagozian, "Structural and stability characteristics of jets in crossflow," *Journal of Fluid Mechanics*, vol. 760, no. 4, pp. 342–367, Dec. 2014.

[49] S. Bagheri, P. Schlatter, P. J. Schmid, and D. S. Henningson, "Global stability of a jet in crossflow," *Journal of Fluid Mechanics*, vol. 624, p. 33, Apr. 2009.

[50] K. C. Gottiparthi, R. Sankaran, A. M. Ruiz, G. Lacaze, and J. C. Oefelein, "Large Eddy Simulation of a Supercritical Fuel Jet in Cross Flow using GPU-Acceleration," in *54th AIAA Aerospace Sciences Meeting*, Reston, Virginia: American Institute of Aeronautics and Astronautics, Jan. 2016, ISBN: 978-1-62410-393-3.

[51] H. Johari, M. Pacheco-Tougas, and J. Hermanson, "Penetration and Mixing of Fully Modulated Turbulent Jets in Crossflow," *AIAA Journal*, vol. 37, no. 7, pp. 842–850, Jul. 1999.

[52] K. Mahesh, "The Interaction of Jets with Crossflow," *Annual Review of Fluid Mechanics*, vol. 45, no. 1, pp. 379–407, 2013.

[53] D. Ahrens, M. Kolb, C. Hirsch, and T. Sattelmayer, "Influence of Preflame and Postflame Mixing on NOx Formation in a Reacting Premixed Jet in Hot Cross Flow," *Journal of Engineering for Gas Turbines and Power*, vol. 138, no. 8, p. 10, 2016.

[54] D. Schmitt, M. Kolb, J. Weinzierl, C. Hirsch, and T. Sattelmayer, "Ignition and Flame Stabilization of a Premixed Jet in Hot Cross Flow," in *Volume 1A: Combustion, Fuels and Emissions*, ASME, Jun. 2013, V01AT04A053, ISBN: 978-0-7918-5510-2.

[55] R. Kulkarni, J. P. Wood, M. Zuber, and H. U. Karim, "Numerical Simulation of a Reacting Jet in a Vitiated Cross Flow Using a Novel Progress Variable Approach," in *Volume 4B: Combustion, Fuels and Emissions*, ASME, Jun. 2017, V04BT04A010, ISBN: 978-0-7918-5085-5.

[56] J. Weinzierl, M. Kolb, D. Ahrens, C. Hirsch, and T. Sattelmayer, "Large-Eddy Simulation of a Reacting Jet in Cross Flow With NOx Prediction," *Journal of Engineering for Gas Turbines and Power*, vol. 139, no. 3, p. 31 502, Sep. 2016.

[57] D. Mavris, "Enhanced Emission Prediction Modeling and Analysis for Conceptual Design," Atlanta, GA, Tech. Rep., 2007. eprint: https://smartech.gatech.edu/bitstream/handle/1853/40892/106154_GT_Combustor_Final_Report_vFINAL.pdf.

[58] S. Yang, R. Ranjan, V. Yang, W. Sun, and S. Menon, "Sensitivity of predictions to chemical kinetics models in a temporally evolving turbulent non-premixed flame," *Combustion and Flame*, vol. 183, pp. 224–241, 2017.

[59] T. L. Cong, E. Bedjanian, and P. Dagaut, "Oxidation of Ethylene and Propene in the Presence of CO ₂ and H ₂ O: Experimental and Detailed Kinetic Modeling Study," *Combustion Science and Technology*, vol. 182, no. 4-6, pp. 333–349, Jun. 2010.

[60] A. D. Siegel, "A computational approach for preliminary combustor design and gaseous emissions evaluations using a method for sparse kinetics," PhD thesis, Nov. 2016.

[61] R. F. Monaghan, R. Tahir, A. Cuoci, G. Bourque, M. Füri, R. L. Gordon, T. Faravelli, A. Frassoldati, and H. J. Curran, "Detailed multi-dimensional study of pollutant formation in a methane diffusion flame," *Energy and Fuels*, vol. 26, no. 3, pp. 1598–1611, Mar. 2012.

[62] A. Andreini and B. Facchini, "Gas Turbines Design and Off-Design Performance Analysis With Emissions Evaluation," *Journal of Engineering for Gas Turbines and Power*, vol. 126, no. 1, p. 83, Jan. 2004.

[63] R. K. Denney, J. C. Tai, and D. N. Mavris, "Emissions prediction for aircraft conceptual design," in *48th AIAA/ASME/SAE/ASEE Joint Propulsion Conference and Exhibit 2012*, 2012, pp. 1–12, ISBN: 9781600869358.

[64] R. Rezvani, "A conceptual methodology for the prediction of engine emissions," PhD thesis, 2010.

[65] O. Schulz and N. Noiray, "Combustion regimes in sequential combustors: Flame propagation and autoignition at elevated temperature and pressure," *Combustion and Flame*, vol. 205, pp. 253–268, 2019. arXiv: 1811.10063.

[66] R. J. Kee, M. E. Coltrin, and P. Glarborg, "Zero- and One-Dimensional Systems," in *Chemically Reacting Flow*, Hoboken, NJ, USA: John Wiley & Sons, Inc., Jan. 2005, pp. 649–692, ISBN: 9780471461296.

[67] H. S. Fogler, *Elements of chemical reaction engineering*. Prentice Hall PTR, 1999, p. 967, ISBN: 0135317088.

[68] S. Yousefian, G. Bourque, and R. F. D. Monaghan, "Review of Hybrid Emissions Prediction Tools and Uncertainty Quantification Methods for Gas Turbine Combustion Systems," in *Volume 4B: Combustion, Fuels and Emissions*, ASME, Jun. 2017, V04BT04A005, ISBN: 978-0-7918-5085-5.

[69] D. G. Goodwin, H. K. Moffat, and R. L. Speth, *Cantera: An Object-oriented Software Toolkit for Chemical Kinetics, Thermodynamics, and Transport Processes*, \url{http://www.cantera.org}, 2017.

[70] A. C. Hindmarsh, P. N. Brown, K. E. Grant, S. L. Lee, R. Serban, D. E. Shumaker, and C. S. Woodward, "{SUNDIALS}: Suite of nonlinear and differential/algebraic equation solvers," *ACM Transactions on Mathematical Software (TOMS)*, vol. 31, no. 3, pp. 363–396, 2005.

[71] H. S. Fogler, *Elements of Chemical Reaction Engineering (5th Edition) (Prentice Hall International Series in the Physical and Chemical Engineering Sciences)*. Prentice Hall, 2016, ISBN: 0133887510.

[72] A. S. AlAdawy, J. G. Lee, and B. Abdelnabi, "Effect of turbulence on NOx emission in a lean perfectly-premixed combustor," *Fuel*, vol. 208, pp. 160–167, 2017.

[73] G. P. Smith, D. M. Golden, M. Frenklach, N. W. Moriarty, B. Eiteneer, C. T. Bowman, R. K. Hanson, S. Song, W. C. Gardiner Jr., V. V. Lissianski, and Z. Qin, *GRI-Mech 3.0*.

[74] Mechanical and Aerospace Engineering (Combustion Research), University of California at San Diego, *Chemical-Kinetic Mechanisms for Combustion Applications*, San Diego Mechanism web page.

[75] T. Sattelmayer, W Polifke, D Winkler, and K Dobbeling, "NOx-Abatement Potential of Lean-Premixed GT Combustors," *Journal of Engineering for Gas Turbines and Power*, vol. 120, no. 1, pp. 48–59, Jan. 1998.

[76] J. Santner, S. F. Ahmed, T. Farouk, and F. L. Dryer, "Computational Study of NOx Formation at Conditions Relevant to Gas Turbine Operation: Part 1," *Energy and Fuels*, vol. 30, no. 8, pp. 6745–6755, 2016.

[77] B. M. Adams, W. Bohnhoff, K. Dalbey, J. Eddy, M. Eldred, D. Gay, K Haskell, P. D. Hough, and L. P. Swiler, "Dakota, a multilevel parallel object-oriented framework for design optimization, parameter estimation, uncertainty quantification, and sensitivity analysis: Version 5.0 user's manual," *Sandia National Laboratories, Tech. Rep. SAND2010-2183*, 2009.

[78] G. A. Gray, J. D. Griffin, M. Taddy, M. Martinez-Canales, and T. G. Kolda, "Hopspack: Hybrid optimization parallel search package," Technical Report SAND2008-8057. Sandia National Laboratories (SNL-CA, Tech. Rep., 2008.

[79] PACE, *Partnership for an Advanced Computing Environment (PACE)*, 2017.

[80] M. D. Sirignano, "Experimental investigation of nitrogen oxide production in premixed reacting jets in a vitiated crossflow," PhD thesis, Georgia Institute of Technology, 2019.

[81] N. Jain and J. M. Seitzman, "Mixing and combustion characterization of a staged combustor with multiple, high mass-ratio jets in crossflow," in *Proceedings of the ASME Turbo Expo*, vol. Part F130041-4B, American Society of Mechanical Engineers (ASME), 2017, ISBN: 9780791850855.

[82] S. M. Correa and I. Z. Hu, "Turbulence-chemistry models in highly strained nonpremixed flames," General Electric Corporate Research and Development, Schenectady, NY, Tech. Rep., 1998.

[83] S. M. Correa, "Models for high-intensity turbulent combustion," *Computing Systems in Engineering*, vol. 5, no. 2, pp. 135–145, Apr. 1994.

[84] J.-Y. Chen, "Stochastic Modeling of Partially Stirred Reactors," *Combustion Science and Technology*, vol. 122, no. 1-6, pp. 63–94, 1997.

[85] D. Haworth, "Progress in probability density function methods for turbulent reacting flows," *Progress in Energy and Combustion Science*, vol. 36, no. 2, pp. 168–259, 2010.

[86] S. M. Correa, "Turbulence-Chemistry Interactions in the Intermediate Regime of Premixed Combustion," *Combustion and Flame*, vol. 93, pp. 41–60, 1993.

[87] R. L. Curl, "Dispersed phase mixing: I. Theory and effects in simple reactors," *AIChE Journal*, vol. 9, no. 2, pp. 175–181, Mar. 1963.

[88] J Villermaux and J. C. Devillon, "Représentation de la coalescence et de la redispersion des domaines de ségrégation dans un fluide par un modele dinteraction phénoménologique," in *Proceedings of the 2nd International symposium on chemical reaction engineering*, Elsevier New York, vol. 26, 1972, pp. 1–13.

[89] C. Dopazo, "Probability density function approach for a turbulent axisymmetric heated jet. Centerline evolution," *Physics of Fluids*, vol. 18, no. 4, pp. 397–404, 1975.

[90] S. B. Pope, "Pdf methods for turbulent reactive flows," *Progress in energy and combustion science*, vol. 11, no. 2, pp. 119–192, 1985.

[91] S Subramaniam and S. B. Pope, "A mixing model for turbulent reactive flows based on Euclidean minimum spanning trees," *Combustion and Flame*, vol. 115, no. 4, pp. 487–514, Dec. 1998.

[92] R. O. Fox, *Computational Models for Turbulent Reacting Flows*. Cambridge: Cambridge University Press, 2003, ISBN: 9780511610103.

[93] C. Celis and L. F. Figueira da Silva, "Lagrangian mixing models for turbulent combustion: Review and prospects," *Flow, Turbulence and Combustion*, vol. 94, no. 3, pp. 643–689, Apr. 2015.

[94] D. E. Knuth, "Structured programming with go to statements," *ACM Computing Surveys (CSUR)*, vol. 6, no. 4, pp. 261–301, 1974.

[95] J. Hoskins and D. Himmelblau, "Process control via artificial neural networks and reinforcement learning," *Computers & chemical engineering*, vol. 16, no. 4, pp. 241–251, 1992.

[96] Z. Zhou, X. Li, and R. N. Zare, "Optimizing chemical reactions with deep reinforcement learning," *ACS central science*, vol. 3, no. 12, pp. 1337–1344, 2017.

[97] G. Brockman, V. Cheung, L. Pettersson, J. Schneider, J. Schulman, J. Tang, and W. Zaremba, *Openai gym*, 2016. eprint: arXiv:1606.01540.

[98] J. Schulman, F. Wolski, P. Dhariwal, A. Radford, and O. Klimov, *Proximal policy optimization algorithms*, 2017. arXiv: 1707.06347 [cs.LG].